LASER INDUCED LOCAL STRUCTURAL AND PROPERTY MODIFICATIONS IN SEMICONDUCTORS FOR ELECTRONIC AND PHOTONIC SUPERSTRUCTURES −SIC TO GRAPHENE CONVERSION

by

Naili Yue

A dissertation submitted to the faculty of
The University of North Carolina at Charlotte
in partial fulfillment of the requirements
for the degree of Doctor of Philosophy in
Electrical Engineering

Charlotte

2013

Approved by:

____
Dr. Yong Zhang

____
Dr. Raphael Tsu

____
Dr. Edward Stokes

____
Dr. Patrick Moyer

ABSTRACT

NAILI YUE. Laser induced local structural and property modifications in semiconductors for electronic and photonic superstructures − SiC to graphene conversion (Under the direction of DR. YONG ZHANG)

Graphene is a single atomic layer two-dimensional (2D) hexagonal crystal of carbon atoms with sp^2-bonding. Because of its various special or unique properties, graphene has attracted huge attention and considerable interest in recent years. This PhD research work focuses on the development of a novel approach to fabricating graphene micro- and nano-structures using a 532 nm Nd:YAG laser, a technique based on local conversion of 3C-SiC thin film into graphene. Different from other reported laser-induced graphene on single crystalline 4H- or 6H- SiC, this study focus on 3C-SiC polycrystal film grown using MBE. Because the SiC thin film is grown on silicon wafer, this approach may potentially lead to various new technologies that are compatible with those of Si microelectronics for fabricating graphene-based electronic, optoelectronic, and photonic devices.

The growth conditions for depositing 3C-SiC using MBE on Si wafers with three orientations, (100), (110), and (111), were evaluated and explored. The surface morphology and crystalline structure of 3C-SiC epilayer were investigated with SEM, AFM, XRD, μ-Raman, and TEM. The laser modification process to convert 3C-SiC into graphene layers has been developed and optimized by studying the quality dependence of the graphene layers on incident power, irradiation time, and surface morphology of the SiC film. The laser and power density used in this study which focused on thin film SiC was compared with those used in other related research works which focused on bulk SiC.

The laser-induced graphene was characterized with μ-Raman, SEM/EDS, TEM, AFM, and, I-V curve tracer. Selective deposition of 3C-SiC thin film on patterned Si substrate with SiO_2 as deposition mask has been demonstrated, which may allow the realization of graphene nanostructures (e.g., dots and ribbons) smaller than the diffraction limit spot size of the laser beam, down to the order of 100 nm. The electrical conductance of directly written graphene micro-ribbon (< 1 μm) was measured via overlaying two micro-electrodes using e-beam lithography and e-beam evaporation. The crystalline quality (stacking order, defect or disorder, strain, crystallite size, etc.) of laser-induced graphene was analyzed using Raman spectroscopy through the comparison with pristine natural graphite and CVD-grown monolayer graphene on SiO_2/Si and other substrates. The experimental results reveal the feasibility of laser modification techniques as an efficient, inexpensive, and versatile (any shape and location) means in local synthesis of graphene, especially in patterning graphene nanostructures. Different from other laser induced graphene research works, which were concentrated on bulk SiC wafers, this PhD research work focuses on thin film SiC grown on Si (111) for the first time.

DEDICATION

I dedicate this dissertation to my father who passed away during my study and my mother for their understanding and huge encouragement, and my wife and son for accompanying me through last 6 years.

ACKNOWLEDGEMENTS

I would to like to express my gratitude to my advisor, Prof. Yong Zhang, for his effort and support in helping me overcome many research barriers, invaluable knowledge, and effective research ideas. I would like to express my appreciation to Prof. Raphael Tsu, for his MBE equipment, knowledge, and support. I would like to express my appreciation to Prof. Edward Stokes, for his inspiring comments, knowledge, and encouragement. I would like to express special thanks to Prof. Patrick Moyer, for his insightful ideas, precious time, and encouragement.

Many thanks to John Hudak and Dr. Lou Deguzman, two best clean room managing faculty I have ever met, for their prompt support and countless helps in all my experimental works carried out in Cameron and Grigg Hall clean rooms. I cherish their helps and friendship. Thanks to Drs. Wattaka Sitaputra, Paolo Batoni, and Jianchao Li for their collaboration in MBE growth. Thanks to Alec Martin and Dr. Robert Hudgins for their experimental support. Thanks to Drs. Terry Xu and Tsing-hua Her for TEM support and help in experiment, respectively.

Finally, I would like to thank the following people for their helps and friendship: Pat Winter, Stephanie LaClair, Jerri Price, and Eddie Hill in ECE; Mark Clayton, Scott Williams, and Margaret Williams in Optical Center; Gail Keene and Andy Gonzales in CRI.

The research was supported by ARO (Grant No. W911NF-10-1-0281), Charlotte Research Institute, Northrop Grumman Corp., and Bissell Distinguished Professorship through Prof. Yong Zhang.

TABLE OF CONTENTS

LIST OF TABLES

LIST OF FIGURES

LIST OF ACRONYMS

AES	auger electron spectroscopy
AFM	atomic force microscopy
ARPES	angle resolved photoemission spectroscopy
BZ	Brillouin zone
BLG	bilayer graphene
CDW	charge density wave
CNT	carbon nanotube
CNW	carbon nanowall
CVD	chemical vapor deposition
CTE	coefficient of thermal expansion
CW	continuous wave
DI	de-ionized
DOS	density of states
DFT	density functional theory
DOE	design of experiment
2DEG	two dimensional electron gas
DMF	N, N-dimethylformamide
EDS	energy dispersive spectroscopy
EELS	electron energy-loss spectroscopy
EG	epitaxial graphene
FLG	few layer graphene
FET	field effect transistor

FWHM	full width half maximum
FIB	focused ion beam
GNR	graphene nanoribbon
GIC	graphite intercalated compound
GOs	graphite oxides
HIL	helium ion lithography
HOPG	highly order pyrolytic graphite
IQHE	integer quantum Hall effect
ICP-RIE	inductively coupled rective ion etching
LL	Landau level
LEED	low energy electron diffraction
LEC	light-emitting electrochemical cell
LCVD	laser induced chemical vapor deposition
LIG	laser induced graphene
MBE	molecule beam epitaxy
MLG	multi-layer graphene
MIBK	methyl isobutyl ketone
MR	magnetoresistance
MWCNT	multi-wall carbon nanotube
NSOM	near-field scanning optical microscopy
OLED	organic light-emitter diode
PDMS	polydimethylsiloxane
PECVD	plasma-enhanced vapor deposition

PLA	pulsed laser annealing
PMMA	polymethyl methacrylate
PS	Polystyrene
PCE	power conversion efficiency
QIC	quantum interference correction
RHEED	reflection high-energy electron diffraction
RGA	residue gas analysis
SEM	secondary/scanning electron microscopy
SdHOs	Shubnikov-de Haas oscillations
STS	scanning tunneling spectroscopy
SLG	single layer graphene
SCCM	standard cubic centimeter per minute
SIMS	secondary ion mass spectrometry
TTL	transistor-transistor-logic
TMD	transition metal dichalcogenides
TBA	tetrabutylammonium hydroxide
TEOS	tetraethyl orthosilicate
UHV	ultra high vacuum
WL	weak localization

CHAPTER 1: CARBON AND GRAPHENE

1.1 Carbon allotropes

Carbon, known for a variety of crystalline or amorphous allotropic forms with different atomic and electronic structures, has special properties and wide applications. The five best known crystalline allotropes are diamond, graphite, fullerenes [1], carbon nanotubes (CNTs) [2], and graphene [3]. Their atomic structures are shown in Figure 1.1. The properties and applications of carbon vary widely with allotropic forms. For example, diamond is well known to be highly transparent, highly thermally conductive, but electrically non-conductive due to its large electronic energy band gap, while graphite is opaque and highly electrically conductive due to its zero band gap of π-bond or p_z electrons derived bands, and anisotropic in thermal conductivity due to the difference between its trigonal σ-bond sp^2 electrons and π-bond p_z electrons; and diamond is among the hardest three-dimensional (3D) materials known to date due to its strong tetrahedral sp^3 σ-bonds, while graphene is soft enough to form a streak on a piece of paper due to its weak Van de Waals force (hence, graphene derives from its name from the Greek word "to write"). The variety in properties and applications is determined by the different crystalline and electronic structures. Diamond and graphite are two 3D allotropes, and rest three allotropes are low-dimensional nanostructures: zero-dimensional (0D) fullerenes, one-dimensional (1D) CNTs (including single-walled, double-walled and multi-walled tubular structures), and two-dimensional (2D) graphene. The properties and applications also vary with dimensionality and shape. For example, in these three low dimensional allotropes, all carbon-carbon bonds are sp^2 hybrid σ-bond with dangling π-bond, but their electronic properties are different because of the different dimensionalities as described in the Table 1.1. In recent years, each time when a low dimensional graphitic nanostructure was discovered and reported, e.g., fullerene in 1985 [1], CNT in 1991 [2], and graphene in 2004 [3], gold rush research was triggered. As a consequence, more special nanostructures and related properties have been studied and explored, and the scope of applications has been widened. Although graphene was explored (in 2004) later than fullerenes and CNTs, the atomic thick hexagonal 2D crystalline structure is the most basic form because fullerenes and CNTs can be derived by wrapping it up into a buckyballs with the introduction of pentagons and rolling it into a tubes, respectively, as shown in Figure 1.2 [4]. Therefore, graphene is the mother of other graphitic carbon systems.

Table 1.1: Allotropes of crystalline carbon

Dimension	**0D**	**1D**	**2D**	**3D**	**3D**
Allotrope	C60	Carbon nanotube	Graphene	Graphite	Diamond
Structure	Spherical	Cylindrical	Trigonally planar	Stacked planar	Tetrahedral
Hybridization	sp^2	sp^2	sp^2	sp^2	sp^3
Electronic properties	Semiconductor	Metal or semiconductor	Semi-metal	Metal	Insulator

Fundamentally, the understanding of the structures, properties and applications of these different carbon allotropes should start from the electron orbital configurations. Carbon, the lightest member of group IV in the periodic table, has six (6) electrons in the configuration of $1s^2 2s^2 2p^2$ in each atom. There are four valence electrons in the 2nd orbital shells: two in the *2s* subshell and two in the *2p* subshell. To form bonds with other carbon atoms, one of the two *2s* electrons of one carbon atom will be promoted into its

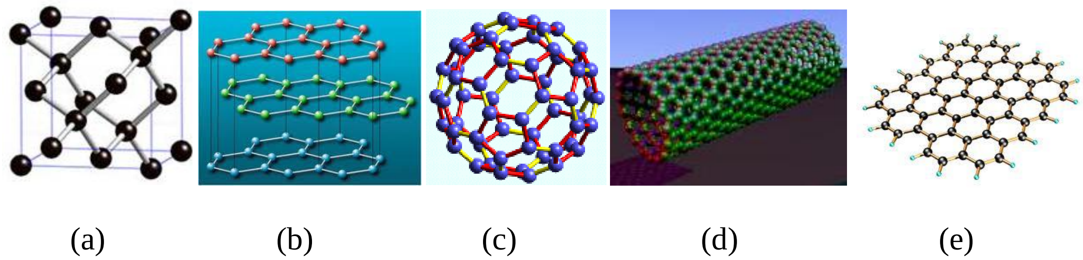

Figure 1.1: Ball-stick models of carbon allotropes. (a) Diamond. (b) Graphite. (c) Fullerene. (d) Carbon nanotube (CNT). (e) Graphene.

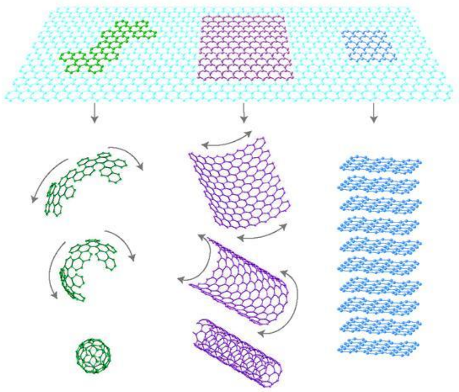

Figure 1.2: Mother of all graphitic forms. Graphene is a 2D building material for carbon materials of all other dimensionalities. It can be wrapped up into 0D buckyballs, rolled into 1D nanotubes, or stacked into 3D graphite (adapted from [4]).

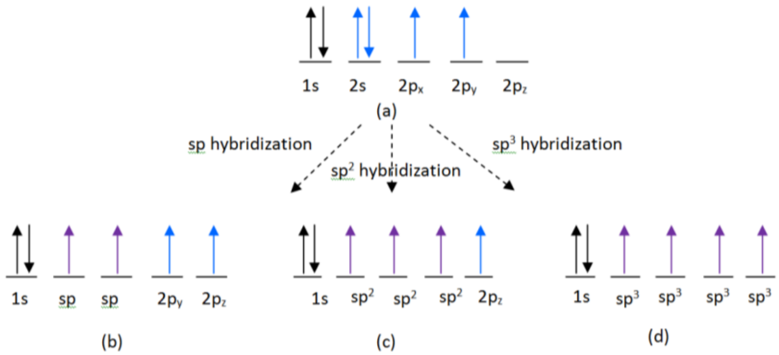

Figure 1.3: Electron configurations and their relative spins in (a) Elemental carbon. (b) *sp* hybrid orbitals. (c) *sp*^{2} hybrid orbitals. (d) *sp*^{3} hybrid orbitals.

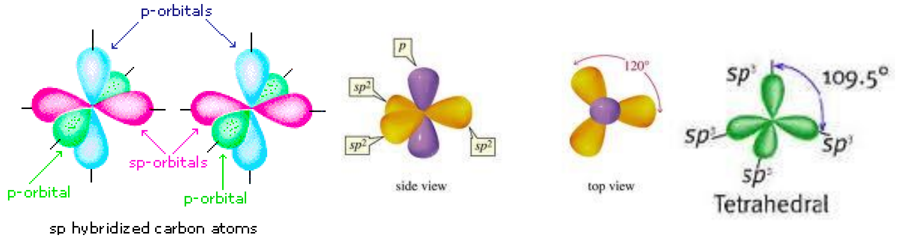

(a) (b) (c)

Figure 1.4: 3D illustration of orbital hybridizations of (a) sp^1, (b) sp^2, and (c) sp^3

empty orbital and then form bonds with other carbon atoms by means of *sp* hybrid orbitals. In general, there are three types of *sp* hybrid orbitals as shown in Figure 1.3, i.e., *sp*, sp^2, and sp^3 as shown in 3D in Figure 1.4, depending on the number of *p* orbitals (1, 2, or 3) mixing with the s orbital. Graphene and diamond are formed with three atoms bonded with sp^2 orbitals in planar triagonal shape and four atoms bonded with sp^3 orbitals in 3D tetrahedral shape, respectively.

1.2 Structure and properties of graphene

Although ideal graphene is unstable from thermodynamic perspective, it may exist through the introduction local curvatures like ripples, wrinkles, or buckling. It can also exist when supported by a foreign material. It was successfully isolated through micromechanical exfoliation and proved to exist in 2004 [4], in spite of local roughness and ripples.

For graphite, the stacking order in the stable and thus lowest energy state is Bernal stacking, in which one of two adjacent graphene layers is rotated by 60$^{\mathrm{o}}$ with respect to the other along the stacking axis, resulting in two sublattices made up of atoms A and B as shown in Figure 1.5(b), respectively. In other words, atom A in one sublattice can see vertically another atom A right below in the adjacent layer below, while atom B in the other sublattice cannot see another atom B right below in the adjacent layer below. The interspacing between layers (c direction) is 3.354 Å [5]. The adjacent layers are π-bonded via the overlap of partially filled p_z orbitals normal to the plane.

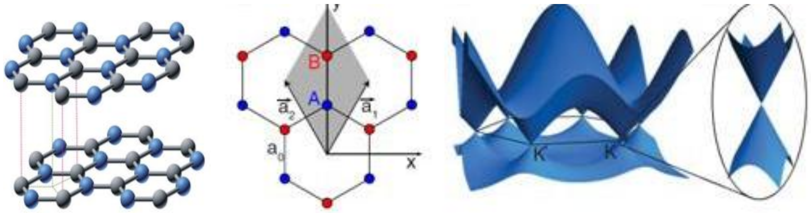

(a) (b) (c)

Figure.1.5: Atomic structure of graphite. (a) Bernal stacking (AB stacking). (b) Lattice structure. (c) Energy spectrum in Brillouin zone (graphene) (adapted from [5]).

One of the most important properties of graphene comes from its unusual electronic structure that can be described in terms of massless two-dimensional Dirac particles [5]. At low energies or long wavelengths, the electrons in graphene are not characterized by their mass but by their speed of propagation, the so-called Fermi–Dirac velocity, which is of the order of 10^6 m/s. At low energies, the electrons in graphene obey a relativistic wave equation in two dimensions [6, 7]. The quasiparticles are chiral and massless Dirac fermions of the electron and hole degenerated at the Diract point. Thus, neutral graphene is a semimetal, i.e., neither a metal nor an insulator.

Unlike common 3D materials, the membrane-like graphene has a negative thermal expansion coefficient due to the tough in-plane sigma bonds [7]. Other properties include unconventional integer quantum Hall effect [3, 8], Klein tunneling [9-11], valley polarization [12, 13], universal minimum conductivity [4, 14, 15], weak (weak-anti) localization [4, 16-20], ultrahigh mobility [4, 21-23], specular Andreev reflection at the graphene-superconductor interface [24, 25], etc. It is encouraging that multi-layer graphene (MLG), which, unlike single-layer graphene (SLG), is less susceptible to the external environment, was found to exhibit behaviors similar to those of SLG [26, 27].

1.2.1 Low energy electronic spectrum

The electronic band structure of graphene was calculated by Wallace [28] in 1947 and Slonczewski [29] in 1958, as an approximate description of graphite. Both of them adopted tight-binding approximation and took into consideration the 2p_z orbital only for each of the two atoms in the primitive cell. The energy dispersion of π and π^* bands is given as follows,

$$E(k) = \pm\gamma_o\sqrt{1 + 4\cos\left(\frac{3}{2}k_x a\right)\cos\left(\frac{\sqrt{3}}{2}k_y a\right) + 4\cos^2\left(\frac{\sqrt{3}}{2}\kappa_y a\right)} \qquad (1)$$

where $\gamma_0 = 2.75\ eV$ is the hopping energy between nearest neighbors, k_x and k_y are the two components of wave vector $\vec{k}$ in the (k_x, k_y) plane, and plus $(+)$ and minus $(-)$ signs represent the upper π and lower π^* band, respectively. The linear dispersion of energy versus momentum, i.e., $E(k) = \pm\hbar v_F|k|$, becomes nonlinear when wavevector k is away from the K or K$'$ point due to a second-order term in threefold symmetry; this phenomenon is known as trigonal warping of the electron energy spectrum [30-32]. The eigenvalues and eigenfunctions (evelope functions) was calculated and reported in referecnes [29, 33-35]. It was found that for both K and K$'$valleys, the rotation of $\vec{k}$ in (k_x, k_y) plane (K or K$'$ point as axis) by 2π will lead to a phase change in π of the wave function. This behavior is called Berry's phase [36]. The Berry phase of π enables graphene's spinelectronic property. The eigenfunctions have two components: up pseudospin ($\alpha = +1$) and low pseudospin ($\alpha = -1$) [37]. Electrons and holes can be represented by $\vec{n} \cdot \vec{k} = 1$ and $\vec{n} \cdot \vec{k} = -1$, repsectively, where $\vec{n}$ is the unit vector in the momentum direction [38].

1.2.2 Effect of a perpendicular magnetic field

The electrons behave differently in graphene than in conventional 2D system when an external magnetic field is applied perpendicularly to the plane. In two dimensional electron gas (2DEG) system, with the magnetic vector potential expressed as $\vec{A} = (-By, 0, 0)$ (Landau gauge), Schrodinger equation is modified as below [39],

$$\left(\frac{(\hat{p}_x - eB\hat{y})^2}{2m_e} + \frac{\hat{p}_y^2}{2m_e} + \frac{\hat{p}_z^2}{2m_e} + V_0(z)\right)\psi = E\psi \tag{2}$$

where m_e is the electron mass, and $V_0(z)$ is the electrostatic potential confined in z direction. If the disorder is introduced, the Hall conductivity of 2DEGs shows a plateau at $lh/2eB$ and is quantized as $\sigma_{xy} = \pm l(2e^2/h)$ [39], resulting in the integer quantum hall effect (IQHE) [40,41]. In contrast, in graphene the energy of LLs can be calculated to be $E_l = sgn(l) v_F \sqrt{2e\hbar B|l|}$, where, $|l|$ =0, 1, 2, 3, …, is the Landau index and B is the magnetic field normal to the graphene plane [42, 43]. The so-called anomalous IQHE can be expressed as $\sigma_{xy} = \pm 2(2l+1)\frac{e^2}{h}$ [3, 8]. The IQHE phenomenon was also conformed by Shubnikov-de Haas oscillations (SdHOs) at low field [3,8], infrared spectroscopy [44, 45], and scanning tunneling spectroscopy (STS) [46-48].

1.2.3 Electrostatic confinement and tunneling

The electron spectrum of GNR depends not only on the width but also on the type of its edges, i.e., whether its edge is in an armchair or zigzag shape [49]. The energy dispersion of GNR can be calculated using the tight-binding method [50-52], Dirac equation [53, 54], or first-principles calculation [55,56]. The eigenvalue equations of zigzag gribbons near the K point are given as $e^{-2\alpha L} = \frac{k_x - \alpha}{k_x + \alpha}$ and $k_x = \frac{k_n}{\tan(k_n L)}$ [57]. In

GNR, the chiral electrons can also be effectivley confined by the boundary. The Klein phenomenon of perfect transmission of carriers normal incident on an extremely narrow potential barrier in graphene was also observed by Young and Kim [58]. Moreover, Steele et al. [59] observed Klein tunneling in ultraclean CNTs with a small band gap. In contrast, Dragoman et al. [60] has shown that both the transmission and refelction coefficients at a graphene step barrier are positive and less than unity.

1.2.4 Electrical transport properties of graphene

Because of the unique band structure, graphene shows several peculiar electronic peorpties which are absent in conventioanl 2DEGs [6, 61]. The most intensively investigated properties include weak anti-localization (WAL) [3, 16-18, 36, 62], minimum conductivity [3, 8, 63, 64], carrier density dependence of conducticity [65-69].

(A) Weak (weak-anti) localization

Quantum interference between self-returned and multiply scattered paths of electrons on the scale of phase coherence length, $L_\phi = \upsilon_F \tau_\phi$, leads to quantum interference correction (QIC) to the electrical ressitance, which manifests itself in the form of weak localization (WL) [70, 71]. Yan et al. [72] used self-consistent Born approximation to study the WL effect in graphene in the presence of charged impurites. Tikhonenko et al.[73] reported that the WL in graphene exists in a large range of carrier density inclduing the Dirac region, resulting from the significant intervalley scattering. Gorbachev et al. [74] reported a similar finding in bilayer graphene. In fact, whether WL or WAL exists in the sample depends on the measurement conditions [75].

(B) Electrical conductivity and mobility

Graphene still exibits a minimum conductivity of the order of e^2/h at the lowest possbile temperature [3, 8] even though the DOS of graphene at the Dirac point is zero. A finite and gate dependent Fano factor of the universal value of 1/3 was also observed at the Dirac point, in agreement with the transport via evanescent wave theory [76]. Based on these theoretical models, the electrical conduction occurs only via evanecent waves, i.e., via tunneling between the electrical contacts, in perfect graphene and at the Dirac point [76, 77]. The theorectically calculated value of minmal conductivity ranges from $(1/\pi)(e^2/h)$ [76-83] to $(\pi/8)(e^2/h)$ [78, 81] and $(\pi/4)(e^2/h)$ [84, 85] per valley and per spin channel. The difference between theoretical and experimental values of minimal conductivity can be accounted for using different models. These puddles, with a characteristic dimension of approxiamately 20~30 nm, have been observed experimentally for graphene samples on SiO_2/Si substrtes [86, 87]. By studing the effect of doping of potassium in ultrahigh vacuum, Chen et al. [88] found that the minimal conductivity only decreased slightly with increasing the doping concentration, despite a siginificant decrease in mobility. In general, a sublinear $\sigma - n$ (conductivity- carrier concentration) curves can be applicable to the transport behavior dominanted by short-range scattering caused by point defects or dislocations in the samples with either a large carrier density or a low charge-impurity concentration. The similar experimental observation can be well explained by the theoretical models [3, 66, 79, 89]. To reduce the scattering from charged impurities, suspending graphene or using high-k dielectrics as supporting substrates are two possible approaches [21, 23, 70-93]. The physical properties and experimental mobilities are summarized in Tables 1.2 and 1.3, respectively.

Table 1.2: Physical properties of graphene

Property	Value	Reference
High spring constant	50 eV$Å^{-2}$	[94]
Young's modulus	1TPa	[95]
Thermal conductivity	(4840~5300) $Wcm^{-1}K^{-1}$	[96]
Fermi velocity	10^6 ms^{-1}	[3]

Table 1.3: Experimental mobility of graphene

Mobility ($cm^2 V^{-1} s^{-1}$)	Synthesis method and test environment	Reference
200,000	Suspended graphene by mechanical exfolitation	[23]
170, 000	Clean in UHV	[90]
100, 000	Natural graphene at 300K	[21]
28,000	Dirty suspended	[90]
3700	CVD on Ni	[97]
4050	CVD on Cu	[98]
5000	Epitaxial graphene on 6H-SiC	[99]
50 ~ 200	Nanoribbon by lithography (1 ~ 4 nm wide)	[100]
	Other semiconductor materials	
1500	Si	[101]
8500	AlGaAs/InGaAs	[101]

1.3 Synthesis of graphene layers (SLG, FLG, and MLG)

Prior to 2004 in which Geim and his coworkers [3] obtained through mechanical exfoliation and electrically characterized single layer graphene, a variety of techniques [102-104] of fabricating graphene layers had been practised and studied though the existence of monolayer graphene was doubted. Most of currently studied synthesis approaches are in fact the development of the precedents. However, the intensive research of recent years have made a significant contribution to the future realization of graphene-based nano-electronics.

The synthesis techniques for making graphene sheets include micromechanical exfoliation, epitaxial growth on SiC substrates [44-45], chemical vapor deposition (CVD) on metal [105-111], reduction from graphite oxide (GO) [112], electrical discharge [113, 114], unzipping of CNT [115-118], and laser sublimation of SiC [119-126].

1.3.1 Exfoliation

(A) Micromechanical Exfoliation

Micromechanical exfoliation is to separate top layers from graphite by applying normal and/or shear force with scotch/cellophane tape or tips of scanning probes of scanning probe microscopes such as AFM, STM or NSOM. The peeled film probably contained multilayer graphene or mixture of multilayer or single layer. The tiny tips of STM or AFM were used to peel and manipulate graphene sheets [127-132]. It was observed [127, 128] that folding or tearing of graphitic sheets which were formed spontaneously during tip scanning due to the friction between the tip and HOPG surface. Ripples were also observed in curved portion to release the strain and stabilize the electronic structure in the bent region [127, 128]. Ruoff group [131] patterned the graphite into small islands first, then tore the island into thin sheets (100 nm thick) using AFM or STM tip. Zhang et al. [132] reduced the thickness of the graphite island from 100 nm down to 10 nm by transferring the detached graphite island to a micromachined silicon cantilever, mounted graphite block onto the cantilever, and then scanned graphite block together with cantilever over a SiO_2/Si surface. Novoselov et al.[133] in 2004, instead of attaching island onto the cantiliver, pressed patterned HOPG square mesa against a 1-μm-thick layer of wet photoresist spun over a glass substrate and baked, followed by cleaving mesa off the HOPG sample and keeping them on the photoresist layer. Successive repeated peeling led to only thin flakes left on the photresist. It was found [133] that thin falkes of less than 10 nm thick attached strongly to SiO_2 due presumably to van der Waals and /or capillary forces. Through using this method, one atomic layer thick graphene sheets have been achieved [3]. Although the micromechanical exfoliation techniques have been developed drastically, the application is limited only to lab research by its drawbacks, i.e., low productivity and thus non-scalable.

(B) Chemical exfoliation

Similar to micromechanical exfoliation, chemical exfoliation is also an old technique, but unlike mechanical exfoliation, it has high productivity and scalability. In general, the chemical exfoliation is divided into two steps: first, to enlarge the interlayer spacing between adjacent graphene layers by forming graphite intercalated compounds (GICs) [134, 135] ; then, to exfoliate the thin graphite sheets via rapid evaporation of the intercalants at an elevated temperature. The processes can be enhanced by subjecting the thermally annealed GICs to treatments like ball milling or ultrasonification [136, 137]. One of the popular methods to form GICs for exfoliation purpose is to soak graphite in mixtures of sulfuric and nitric acids for an extended period of time [136, 138]. After an appropriate duration of soaking, the acid molecules penetrated into the graphite, forming alternating layers of graphite and intercalant. Following the intercalation, exfoliation is applied by rapid evaporation of the intercalants at elevated temperature. Post-treatments such as ball milling and ultrasonication can be used to improve the extent of exfoliation [136, 137, 139]. In order to obtain SLG sheets, the intercalation and exfoliation processes have to be repeated by using different intercalating and exfoliating chemistry and processes [140, 141]. Viculis et al. [135] reported a chemical route to synthesize carbon nanoscroll.

1.3.2 Reduction of graphite oxides (GOs)

Different from direct exfoliation with chemical solution, indirect exfoliation with the pre-oxidized graphites (GOs) first and then easily exfoliated GOs can be used to generate thin graphene sheets [142, 143]. The exfoliated GO sheets can be subsequently converted into thin graphene sheets with chemical, thermal, or electrochemical reduction processes [144-146].

To obtain SLG sheets, Horiuchi and coworkers have developed a two-step process [147, 148]. The first step was to oxidize the graphite using the Hummer's method, in which natural graphite particles were immersed in a mixture of H_2SO_4, $NaNO_3$, and $KMnO_4$ to obtain GICs (or GOs). In the next step, the GOs were hydrolyzed to induce the hydroxyl and ether groups into the intergraphene layer spaces, after which each GO layer became a multiply charged anion with a thickness of approximate 0.6 nm. The resulting GO layers formed a stable dispersion in water. By using this process, Horiuch et al.[147] succeeded in obtaining SLG sheets. Ruoff and co-workers developed a series of processes involving the complete exfoliation of GOs into individual GO sheets followed by their in situ reduction to obtain single graphene layer [148, 149]. The process began with the oxidation of graphite using the Hummer method [143]. Although the electrical conductivity of reduced GO sheets was found to be five orders of magnitude higher than the original GO sheets, it is still ten times lower than that of pristine graphite powders at about 10% of the bulk density. In fact, the electrical transport of reduced GO sheets was found to be dominated by hopping [150]. Raman spectroscopy reveals that the reduced GO sheet is highly disordered [149-151]. The reduced GOs may find applications in areas in which high mobility is not so critical such as transparent conductive thin film [152, 153], or composite materials [154-156].

Some methods have been developed to create colloidal suspension of graphene sheet, based on controlled charging of the graphene sheets during or after the reduction process [157-159]. Several non-oxidation and reduction based methods have been reported to reduce the disorder and defects [160]. Fabrication of graphene sheets via chemical routes poses both potential and challenges. Efforts are required for both gaining an understanding of the intercalation, oxidation, exfoliation, reduction, functionalization, and dispersion processes and developing new starting materials and reaction routes. More details can be found in a recent review [158]. The chemical synthesis of graphene has some disadvantages such as low yield and defective graphene.

1.3.3 CVD Growth on metal surfaces

SLG or MLG layers can be grown on some metal surfaces via either surface segregation of carbon atoms or themal decomposition of carbon-containing molecules [107].

According to the available literature, eight metals have been investigated: Co (0001) [161], Ru (0001) [101, 162-165], Ni (111) [166-169], Ni (100) [170], Ir (111) [171-173], Rh (111) [101, 174], Rh (100) [174], Pd (111), Pd (100) [161], Pt (111) [161, 175-178], Pt (100) [175-178, 179], Pt (110) [176, 177] and Cu [177]. The electronic structure of the metal surface determines the coupling between the carbon π orbital and substrate surface atoms, while the lattice constant of the metal influences the basal hexagonal structure of graphene layers, especially, the single- layer or few-layer graphene. The lattice constants and lattice mismatch between graphene and different metals are summarized in Table 1.4.

Table 1.4: Lattice constants of graphene and metals

Element	**Graphene**	**Ni(111)**	**Rh(111)**	**Ru(0001)**	**Ir(111)**	**Pt (111)**
Lattice constant (Å)	2.46	2.49	2.69	2.71	2.72	2.77
Lattice mismatch (%)	N/A	1.2	8.5	9.2	9.6	11.2

N'Diaye *et al*. [173] observed an incommensurate structure with a periodicity of 9.32 unit cells in graphene formed on Ir (111) by the decomposition of ethylene at 1320 K. Gamo *et al*. [169] found the spacing between the Ni surface and carbon layer is 2.1 Å and the two carbon sublattices sit on the metal atoms and the fcc hollow sites between these atoms, respectively, through ion scattering and low energy electron diffraction (LEED) analyses. Table 1.5 lists all d-spacing values between graphene and metal.

Table 1.5: Distance between graphene and metal substrates

	graphene	**Ni (111)**	**Ru (0001)**	**Pd (111)**	**Ir (111)**	**Pt (111)**	**Al (111)**	**Ag (111)**	**Cu (111)**	**Au (111)**	**SiC**
d	3.35	2.1	2.2	2.3	3.77	3.3	3.41	3.33	3.36	3.31	1.62

The strong coupling between graphene and the substrate may lead to weaker C-C bonds in the graphene plane and thus redshift phonons of the graphene layer, specially for the out-of-plane vibration modes. Graphene on Ni (111) and Ni (001) [180] and Ru (0001) [164] have showed the similar phenomenon, i.e., redshift of phonon energy of graphene. There is a trend that the interaction strength increases with the decrease in both the index and occupation of the *d* orbitals.

1.3.4 Epitaxial growth on SiC

Although CVD growth of graphene on metal substrate can be scalable for mass production, graphene has to be transferred to an insulating substrate to make devices. The epitaxial growth of graphene on SiC can avoid the transfer process. The detailed review on epitaxial growth of graphene on SiC can be found in references [181, 182].

In 1975, Bommel *et al.*[103] found the graphitization film formed on SiC in UVH (10^{-10} Torr) at a temperature higher than 1500 °C by using low energy electron diffraction (LEED) and Auger electron spectroscopy (AES) analysis techniques. In recent years, Berger et al. [183] has investigated intensively on epitaxial growth of graphene on SiC and achieved single and few layer graphene sheets on SiC. One limitation in epitaxial growth of graphene on Si-face SiC is that the domain size of graphene is limited by the roughening of the substrate during graphitization. The average step size after graphene formation is mostly in the range of 20–50 nm, independent of the initial step size of the substrate [184].

1.3.5 Unzipping of CNTs

As CNTs can be formed by rolling up graphene, graphene can reversely be formed by unzipping CNTs in longitudinal direction. Kosynkin et al. [116] synthesized GNRs by unzipping MWCNTs in concentrated H_2SO_4 acid followed by treatment with 500 wt% $KMnO_4$ for 1 hr at room temperature (22 ^{o}C) and 1 hr at 55–70 ^{o}C. After isolation, the resulting nanoribbons were highly soluble in water (12mg.ml^{-1}), ethanol and other polar organic solvents. Jiao et al [117] demonstrated an approach to making GNRs by unzipping multi-walled carbon nanotubes (MWCNTs) by plasma etching of nano-tube partly embedded in polymer film.

1.3.6 Particle beam-induced graphene

In 1982, Iijima [185] accidently discovered the graphitization of SiC when he used electron microscope to investigate 6H-SiC. It was found that some graphitized crystallites resulted from the SiC decomposed in vacuum by the electron beam irradiation with the acceleration voltage of 100 kV and beam current density of 100 C/cm^2. Perrone et al [120] studied the possibility of graphene growth on 4H-silicon carbide surface via laser processing. Raman and XPS results showed graphene signatures. Although the integrated intensity ratio of D to G band is high (> 1), the study demonstrates the possibility of graphene growth on SiC by laser illumination. Lemaitre et al [123] reported a technique to selectively graphitize regions of SiC by ion implantation first then pulsed laser annealing (PLA). Although the relative intensity and FWHM of 2D band is rather low and large, repsectively, this study also showed the feasibility of laser annealing process in graphene synthesis. CO_2 (10.6 μm) laser-induced growth of epitaxial graphene on 6H-SiC was reported by Yannopoulos [122]. The formation of few layer epitaxial graphene (EG) on SiC and its features were investigated by SEM, XPS, SIMS and Raman. In this study, high quality graphene with low ratio of D/G was obtained, which further proved laser annealing process was a viable means to synthesize graphene.

Lee et al [121] also demonstrated a low-temperature, spatially controlled and scalable epitaxial graphene (EG) synthesis based on laser-induced surface decomposition of the Si-rich face of a SiC single-crystal. It was also found that the thickness of the EG could be controlled down to single layer by adjusting laser fluence.

All the above-mentioned laser annealing processes are focused on hexagonal (4H or 6H) SiC polytype wafers. Recently, two alternative laser assisted graphene growth methods were reported [124, 125]. Wei and Xu [124] reported that under the laser illumination, carbon atoms decomposed from PMMA coated on silicon wafer could be absorbed by the molten silicon surface and then separated during the cooling process to form a few-layer graphene. Park et al [125] developed a laser-induced chemical vapor deposition (LCVD) to pattern graphene on metal.

From the above brief survey, it becomes clear that the use of focused laser beams, apart from enabling patterning, offer viable solutions to lower the graphene growth temperature down to room temperature as well as to speed-up the growth process. Laser illumination method has the following advantages over conventional thermal epitaxial growth: (1) Ambient growth of epitaxial graphene; (2) Rapid efficient process with process time of sub-second, depending on laser power; (3) The cooling rate, which is essential for the uniformity of the stress that develops on EG, can be as high as 600 Ks^{-1}. The fast cooling rate might also affect the stacking order or stacking faults of Si-face EG, which is the dominant factor affecting carrier mobility; and (4) No pre-treatment (e.g. H_2 etching, so on) of SiC surface is needed to obtain high quality graphene. In this study, unlike other laser related works in which bulk SiC wafers were used, about 190 nm thick SiC thin film is first grown on Si substrate, then graphene layers are induced by laser illumination [126].

CHAPTER 2: MBE GROWTH OF 3C-SiC ON Si WAFTER

2.1 MBE growth and substrate preparation

An ultra high vacuum (UHV) MBE system (SVT Inc., MN, USA) was employed to grow 3C-SiC on Si wafer with different orientations (100), (110) and (111). Buckyball fullerene (C60) powder (source) loaded in the Knudsen cell was used as a carbon source and Si wafers as both substrate and Si source. The MBE chamber is capable of being pumped down to 10^{-10} torr with three cascaded pumps: mechanical, turbo-molecular, and cryo-pumps. Reflection high electron energy diffraction (RHEED) and residue gas analyzer (RGA) are integrated into the chamber to in-situ monitor real time growth and residue gases. Both source and substrate can be resistively heated up to 1100 ^{o}C. Liquid nitrogen (N_2) is introduced through shroud in between inner and outer chamber wall to cool down the chamber and effusive cell to avoid any contaminants being evaporated on the sample or substrate during growth. The substrate holder is cooled by circulating chilly water to control the post-growth cooling rate. An RF match box integrated with chamber is used to generate N_2 for growing III-nitrides. The architecture of MBE system is shown in Figure 2.1.

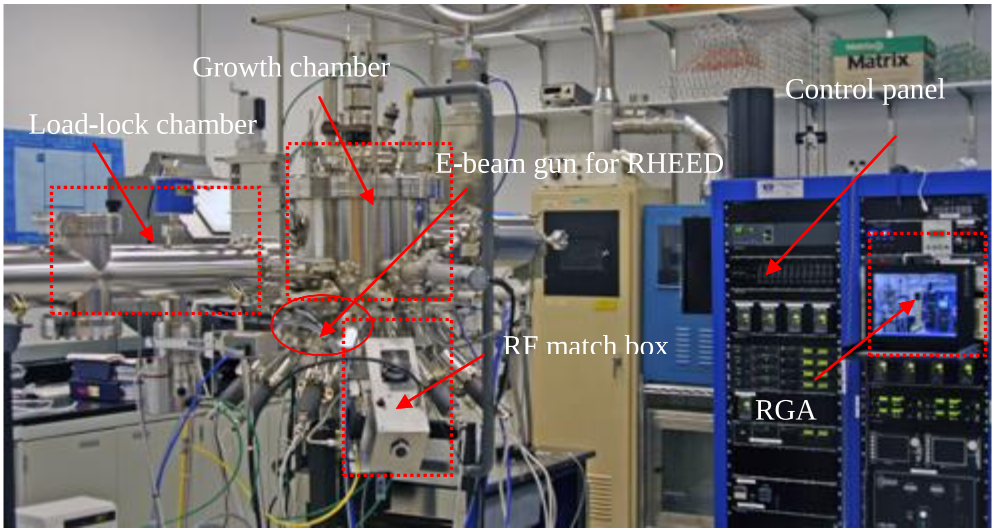

Figure 2.1: SVT MBE system capable of growing II-VI, III-nitride, Si and SiC semiconductor materials.

In order to make sure a clean surface for growing high quality film on the silicon wafer substrates, the Si wafers need to undergo two types of cleaning processes: wet cleaning and in-situ cleaning. Wet cleaning process is the same as the standard Si wafer cleaning used in semiconductor industry as described in Table 2.1. However, it is unavoidable for the cleaned Si wafer surface to be exposed to air and slightly oxidized again during transfer from clean room to MBE chamber. In-situ cleaning process can further remove this native oxide layer formed during sample transfer. In-situ cleaning process occurs in the growth chamber after the substrate is loaded into chamber. The cleaned Si wafer is loaded into load-lock chamber and then transferred into growth chamber through butterfly gate valve. Normally, it takes six (6) hours or a whole night to pump the growth chamber down to 10^{-10} torr before starting growth process. Since some residue gas may be adsorbed on the cleaned wafer, it is necessary to preheat wafer at 300 ^{o}C for half an hour after the base pressure reaches 10^{-10} torr and wait until the base pressure returns to the lowest level again. When the base pressure reaches 10^{-10} torr without any residue gas adsorbed on Si substrate surface, the Si substrate is heated up to above 850 °C and hold for at least half an hour to remove a few nanometer thick native SiO_2 layer formed during sample transfer from clean room to MBE chamber. This in-situ, or in chamber, cleaning process can further clean Si substrate surface. The cleanliness of the wafer can be monitored with reflection high energy electron diffraction (RHEED), as shown in Figure 2.2 (a).

Table 2.1 Cleaning processes for silicon wafer substrates

Steps	Processes
1	Soak Si wafer in acetone and methanol solution assisted with ultrasonic vibration for 5 minutes each, followed by rinsing with de-ionized (DI) water until resist reaches 12 ~ 15 MΩ
2	Dip Si wafer in (H_2O_2: H_2SO_4=2:3) solution mixed with 100 ml H_2O_2 and 150 ml H_2SO_4 for 20 min.
3	Rinse Si wafer with DI water until resist reaches 12~15 MΩ
4	Dip Si wafer in diluted HF (H_2O:HF=10:1) for 10 seconds
5	Rinse Si wafer until resist reaches 12~15 MΩ
6	Dry Si by blowing with nitrogen (N_2) gas

2.2 Design of experiment (DOE) for the evaluation of growth conditions

It was found that under the pressure of 10^{-10} torr, fullerene (C60) started to evaporate at 450 °C and was depleted very quickly at 700 °C. Also, at the substrate temperatures below 600 °C, no SiC or carbon film was grown on Si substrate. In this growth process evaluation, T_{C60} = 650 °C was only combined with T_{sub} = 700 °C, because 3C-SiC film peeled off from the Si substrate when the substrate temperature was increased up to 800 °C or beyond at T_{C60} = 650 °C. This may be caused by the larger kinetic energy of carbon atoms, excessive C60, larger coefficient of thermal expansion (CTE) of SiC, or all of them. Furthermore, C60 power source would be quickly depleted if the source temperature is raised above 650 °C. Hence, T_{C60} = 650 °C was excluded from the evaluation of T_{sub} = 800, 900, and 1000 ^{o}C. The upper limit of heating capability of MBE is 1100 ^{o}C. At T_{sub} = 1050 ^{o}C, 3C-SiC film was observed to easily flake-off due to large lattice mismatch (20%) and CTE mismatch, especially at a high temperature. The design of experiment one (DOE (I)) is described in Table 2.2. In this evaluation, two types of Si wafers, Si (100) and (111), were grown simultaneously in each deposition. The temperatures of C60 source and Si substrate were increased from 450 to 650 ^{o}C and from 700 to 1000 ^{o}C, respectively. The increment step of temperature is 100 ^{o}C for both, growing time is 5 minutes, and the heating and cooling rates are 10 ^{o}C/min. For each growth, the samples were held at growing temperature for about 2 minutes to homogenize SiC film after the growth was over.

Table 2.2: DOE (I) for growing 3C-SiC on Si substrates (001) and Si (111)

S/N	**Substrate temperature (T_{C60})**	**Source temperature (T_{Si})**	**Growth time (min.)**	**Base pressure (torr)**	**Growth pressure (torr)**
1	700	450	5	<6. 0 $\times10^{-10}$	9.1 $\times10^{-9}$
2	700	550	5	<6. 0 $\times10^{-10}$	6.5 $\times10^{-8}$
3	700	650	5	<6. 0 $\times10^{-10}$	9.2 $\times10^{-8}$
4	800	450	5	<6. 0 $\times10^{-10}$	9.6 $\times10^{-9}$
5	800	550	5	<6. 0 $\times10^{-10}$	7.5 $\times10^{-8}$
6	900	450	5	<6. 0 $\times10^{-10}$	1.3 $\times10^{-8}$
7	900	550	5	<6. 0 $\times10^{-10}$	8.2 $\times10^{-8}$
8	1000	450	5	<6. 0 $\times10^{-10}$	3.6 $\times10^{-8}$
9	1000	550	5	<6.0 $\times10^{-10}$	8.9 $\times10^{-8}$

Following the evaluation of growth conditions and characterization of SiC films grown in DOE (I), the source temperature (T_{C60}) of 550 ^{o}C and two substrate temperatures (T_{sub}) of 800 and 1000 ^{o}C were selected as growth conditions for the comparison of SiC films grown on three plane orientations Si (100), (110), and (111), because the flux of T_{C60} = 550 ^{o}C yields more uniform SiC film than T_{C60} = 450 ^{o}C, T_{sub}

= 800 ^{o}C generates more uniform SiC than T_{sub} = 900 and 1000^{o}C, and 1000 ^{o}C generates highest crystallization of SiC film. The growth time for T_{sub}=800 ^{o}C and T_{sub}=1000 ^{o}C are 10 and 20 minutes, respectively. The evaluation growth conditions for DOE (II) are listed in Table 2.3.

Table 2.3: DOE (II) for growing 3C-SiC on Si (100), (110) and (111)

S/N	**Si substrate orientation**	**Substrate temperature (T_{sub})**	**Source temperature (T_{C60})**	**Growth time (min.)**
1	(100), (110), (111)	800	550	10
2	(100), (110), (111)	1000	550	20

2.3 Growth control and results

During the heating, growth, and cooling processes, the liquid nitrogen (LN_2) was introduced through shroud between the inner and outer walls of the growth chamber to cool the inner wall of the chamber, preventing the contaminants deposited on the inner wall of chamber from being re-evaporated and thus being deposited on the sample. During growth, substrate manipulator, i.e., sample holder, was rotated at the rate of 10 rounds per minute (rpm) to homogenize the SiC thin film. The residue gases before and during growth were in-situ monitored by residue gas analyzer (RGA), i.e., mass spectrometry (MS). The cleanliness of Si substrate surface in chamber, and nucleation and growth of the SiC film were in-situ inspected with RHEED. RHEED, low energy electron diffraction (LEED) and auger electron spectroscopy (AES) are the three major surface characterization techniques which are very useful in real time in-situ monitoring of thin-film growth. In RHEED subsystem, a thermionic electron gun was used to emit electrons which are accelerated under electrical field, focused with electromagnetic field, and deflected with electrostatic field toward the substrate surface at a glance incident angle of less than 2^o. If the substrate or thin film surface is clean or atomic flat, the diffract pattern is streaks. During the growth, the streak patterns disappear, and the dots or concentric rings patterns appear as shown in Figure. 2.2 (a) and (b). The streaks patterns are the electron diffraction of flat two-dimension surface and dot patterns are from that of three-dimension surface. SiC thin film grown on a 2-inch Si (111) at the substrate and source temperatures of 800 and 550 ^{o}C, respectively, are shown in Figure 2.3.

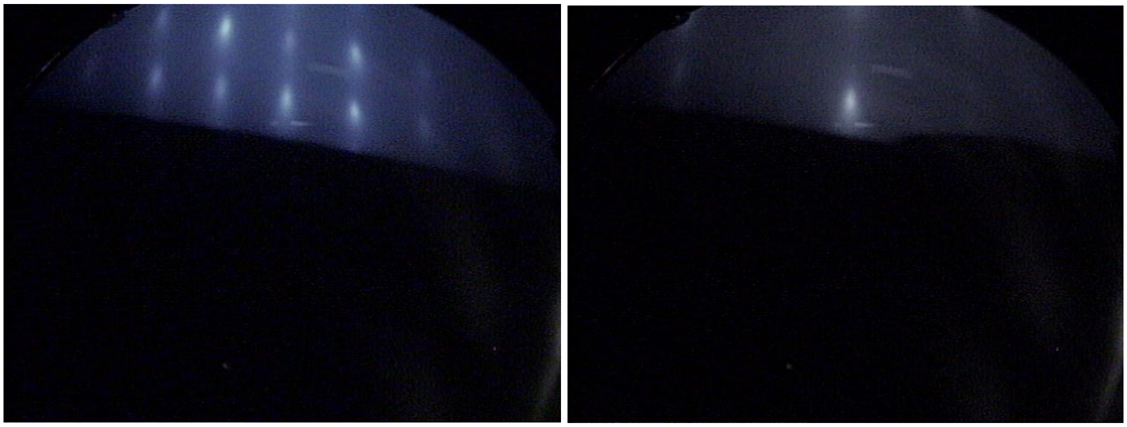

(a) Before growth (b) During growth

Figure 2.2: RHEED patterns in the growth of 3C-SiC thin film on Si substrates. (a) Before growth. (b) During growth.

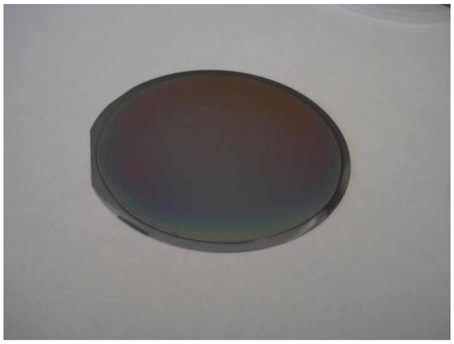

Figure 2.3: 3C-SiC film grown on a 3-inch Si (111) wafer

2.4 Characterization and analyses of samples grown on Si (100) and Si (111)

The surface morphology and topography of 3C-SiC thin films were measured with SEM (JEOL 6460LV and Raith 150) and AFM (Nanoscope SPM V5r30), respectively. The SEM micrographs of the samples grown in DOE (I) are shown in Figures 2.4, 2.5, and 2.6. The corresponding AFM topography images are shown in Figures 2.7, 2.8, and 2.9. In Figures 2.4 and 2.7, it can be seen that at the substrate of 700 ^{o}C, the SiC film gown at T_{C60} = 550 ^{o}C is rougher than that grown at T_{C60} = 450 ^{o}C but smoother than that grown at T_{C60} = 650 ^{o}C. This is because the evaporation flux of C60 at T_{C60} = 450 ^{o}C is lower than that at T_{C60} = 550 ^{o}C and thus is insufficient, resulting in that the SiC grown at T_{C60} = 450 ^{o}C is amorphous and of lower converage. However, the SiC grown at T_{C60} = 550 ^{o}C is more crystalline due to the increase of source temperature which also increases the reaction energy for formation of SiC. This can be corroborated by that the grain size of SiC grown at T_{C60} = 550 ^{o}C as shown in Figures 2.4 (a), (b), (c) and (d). When the temperature of source C60 increases from T_{C60} = 550 ^{o}C to T_{C60} = 650 ^{o}C, the roughness increases, but the grain size decreases. This is because the larger evaporation flux of C60 at T_{C60} = 650 ^{o}C in combination with the low reaction rate at T_{sub} = 700 ^{o}C result in the deposition of excessive decomposed C60 on top of SiC film. There is also excessive decomposed C60 on SiC/Si grown at T_{sub}/ T_{C60} = 700/550 ^{o}C. This can be confirmed by the broad D and G Raman bands of decomposed C60 shown in the corresponding Raman spectra shown in Figures 2.18 (b) and 2.19 (b). The grain size of decomposed C60 is smaller than that of SiC film. The above analyses are applicable to both Si (100) and (111). At the substrate temperature from 800 to 1000 ^{o}C, the roughness of SiC film increases for source temperatures of both 450 and 550 ^{o}C, because the grain size of SiC increases with crystallization. However, for both Si (100) and Si (111), the SiC grown at T_{C60} = 450 ^{o}C is always rougher than that of SiC grown at T_{C60} = 550 ^{o}C, because the evaporation flux of C60 at T_{C60} = 450 ^{o}C is insufficient for providing enough carbon atoms to react with the Si atoms from the substrate. Moreover, the SiC film grown on Si (100) is rougher than that on Si (111), because the area atomic density of Si (111) is higher than that of Si (100) (as indicated in Table 2.7). An obvious observation in Figures 2.5, 2.6, 2.8 and 2.9 is that the grain size increases significantly when the substrate temperature increases from 800 to 900 ^{o}C and from 900 to 1000 ^{o}C, respectively. Probably, nucleation and growth of SiC mainly complete at the temperature above 800 ^{o}C and the coalescence occurs above 900 ^{o}C. This is in agreement with the XRD results in which FWHMs of the 2θ peaks corresponding to 3C-SiC (111) and 3C-SiC (200) drops significantly from 900 to 1000 ^{o}C, as shown in Figure 2.23. Figure 2.10 shows the roughness comparison of SiC grown on Si (100) and (111) at different substrate and source temperatures. At T_{sub} = 700 or 800 ^{o}C, SiC thin films grown on Si (100) and Si (111) at T_{C60} = 550 ^{o}C is rougher than that at T_{C60} = 450 ^{o}C for small domain area, because the extent of SiC crystallization at T_{C60} = 550 ^{o}C is more than that at T_{C60} = 450 ^{o}C, and grain size increases. However, in the large domain area, the film coverage of SiC grown at T_{C60} = 550 ^{o}C is higher than that at T_{C60} = 450 ^{o}C due to the higher C60 evaporation flux at T_{C60} = 550 ^{o}C. At T_{sub} = 900 or 1000 ^{o}C, SiC thin films grown on Si (100) and Si (111) at T_{C60} = 550 ^{o}C is smoother than that at T_{C60} = 450 ^{o}C for small domain area due to the higher C60 evaporation flux at T_{C60} = 550 ^{o}C. At T_{C60} = 550 ^{o}C, SiC grown on Si (111) is always smoother than that on Si (100) for all T_{sub} = 700, 800, 900 and 1000 ^{o}C due to the higher area atomic density of Si (111).

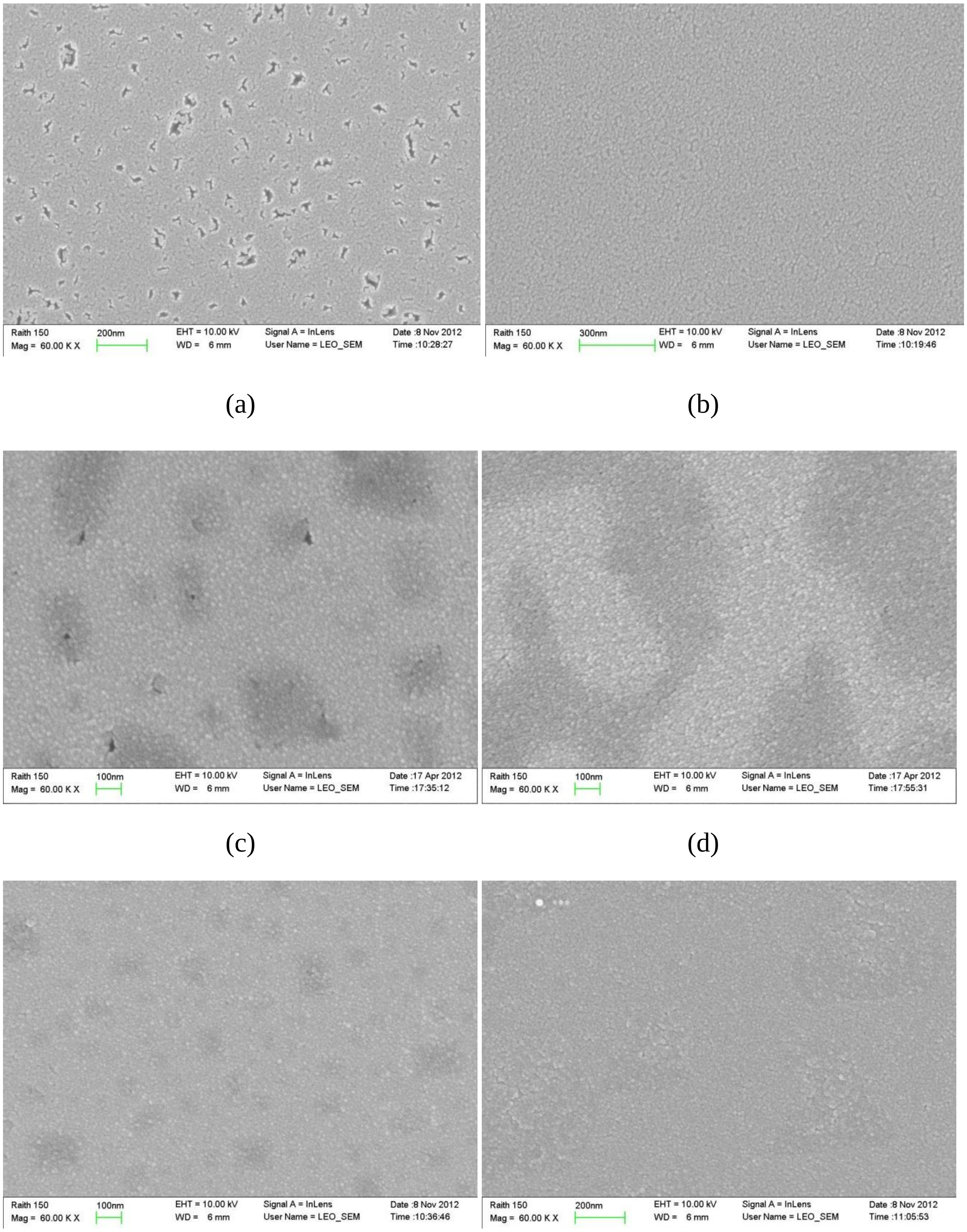

(a) (b)

(c) (d)

(e) (f)

Figure 2.4: SEM micrograph of 3C-SiC grown on Si (100) and Si (111) at T_{sub} = 700 ^{o}C. (a) T_{C60} = 450 ^{o}C, Si (100). (b) T_{C60} = 450 ^{o}C, Si (111). (c) T_{C60} = 550 ^{o}C, Si (100) . (d) T_{C60} = 550 ^{o}C, Si (111). (e) T_{C60} = 650 ^{o}C, Si (100) (f) T_{C60} = 650 ^{o}C, Si (111)

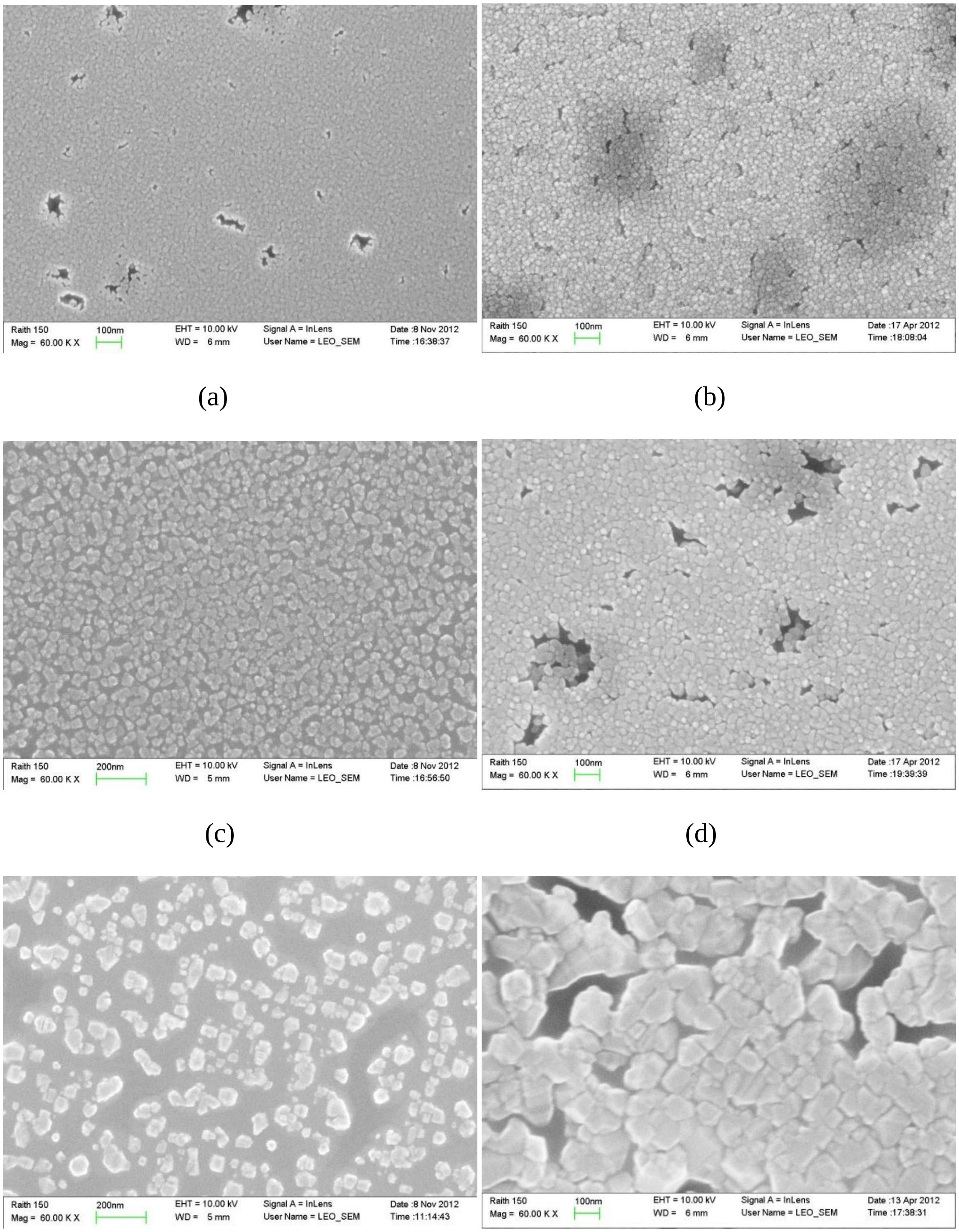

(a) (b)

(c) (d)

(e) (f)

Figure: 2.5: SEM micrograph of 3C-SiC grown on Si (100) substrate. (a) T_{sub} = 800 ^{o}C, T_{C60} = 450 ^{o}C. (b) T_{sub} = 800 ^{o}C, T_{C60} = 550 ^{o}C. (c) T_{sub} = 900 ^{o}C, T_{C60} = 450 ^{o}C. (d) T_{sub} = 900 ^{o}C, T_{C60} = 550 ^{o}C. (e) T_{sub} = 1000 ^{o}C, T_{C60} = 450 ^{o}C. (f) T_{sub} = 1000 ^{o}C, T_{C60} = 550 ^{o}C.

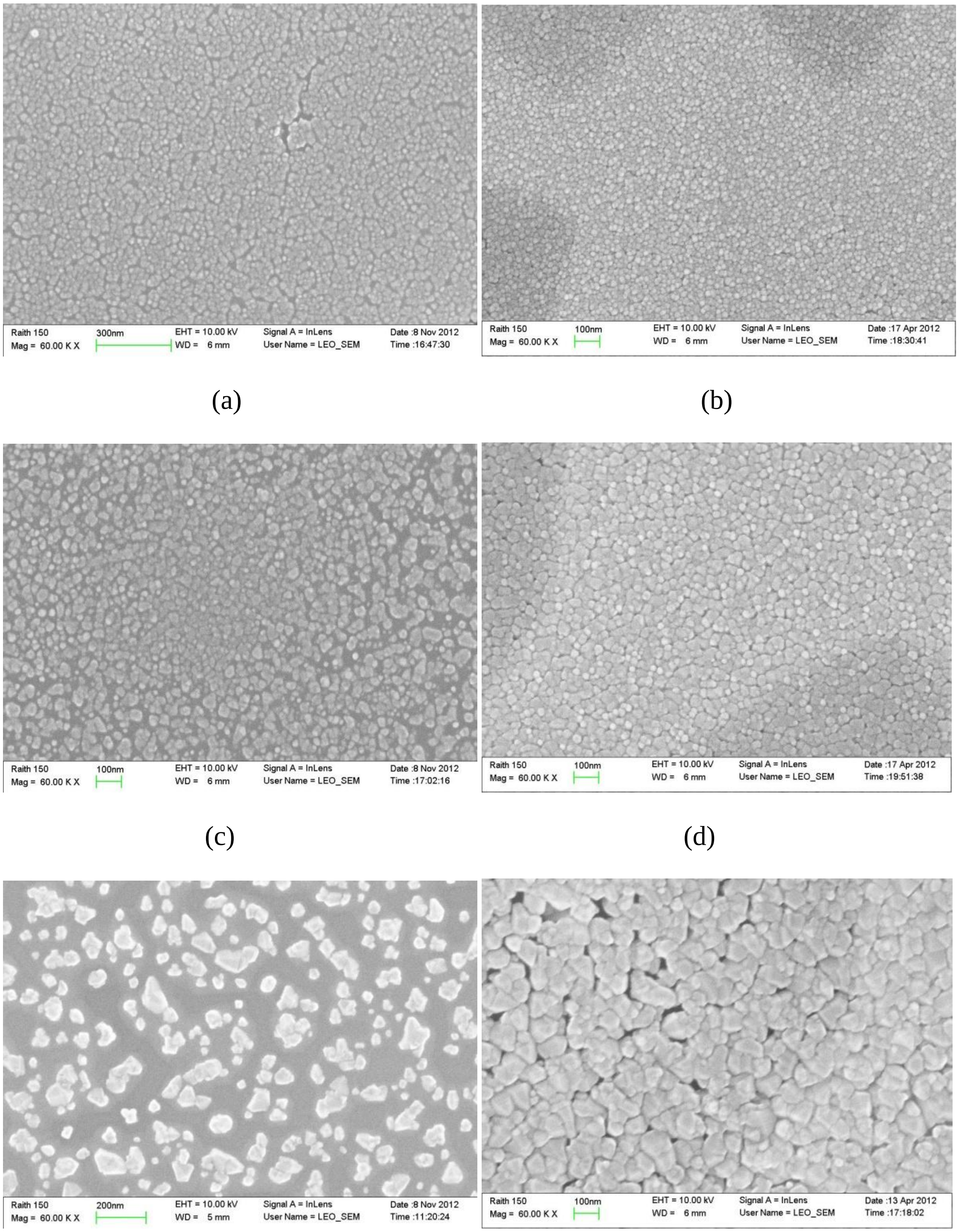

(a) (b)

(c) (d)

(e) (f)

Figure 2.6: SEM micrograph of 3C-SiC grown on Si (111) substrates. (a) T_{sub} = 800 ^{o}C, T_{C60} = 450 ^{o}C. (b) T_{sub} = 800 ^{o}C, T_{C60} = 550 ^{o}C. (c) T_{sub} = 900 ^{o}C, T_{C60} = 450 ^{o}C (d) T_{sub} = 900 ^{o}C, T_{C60} = 550 ^{o}C. (e) T_{sub} = 1000 ^{o}C, T_{C60} = 450 ^{o}C. (f) T_{sub} = 1000 ^{o}C, T_{C60} = 550 ^{o}C.

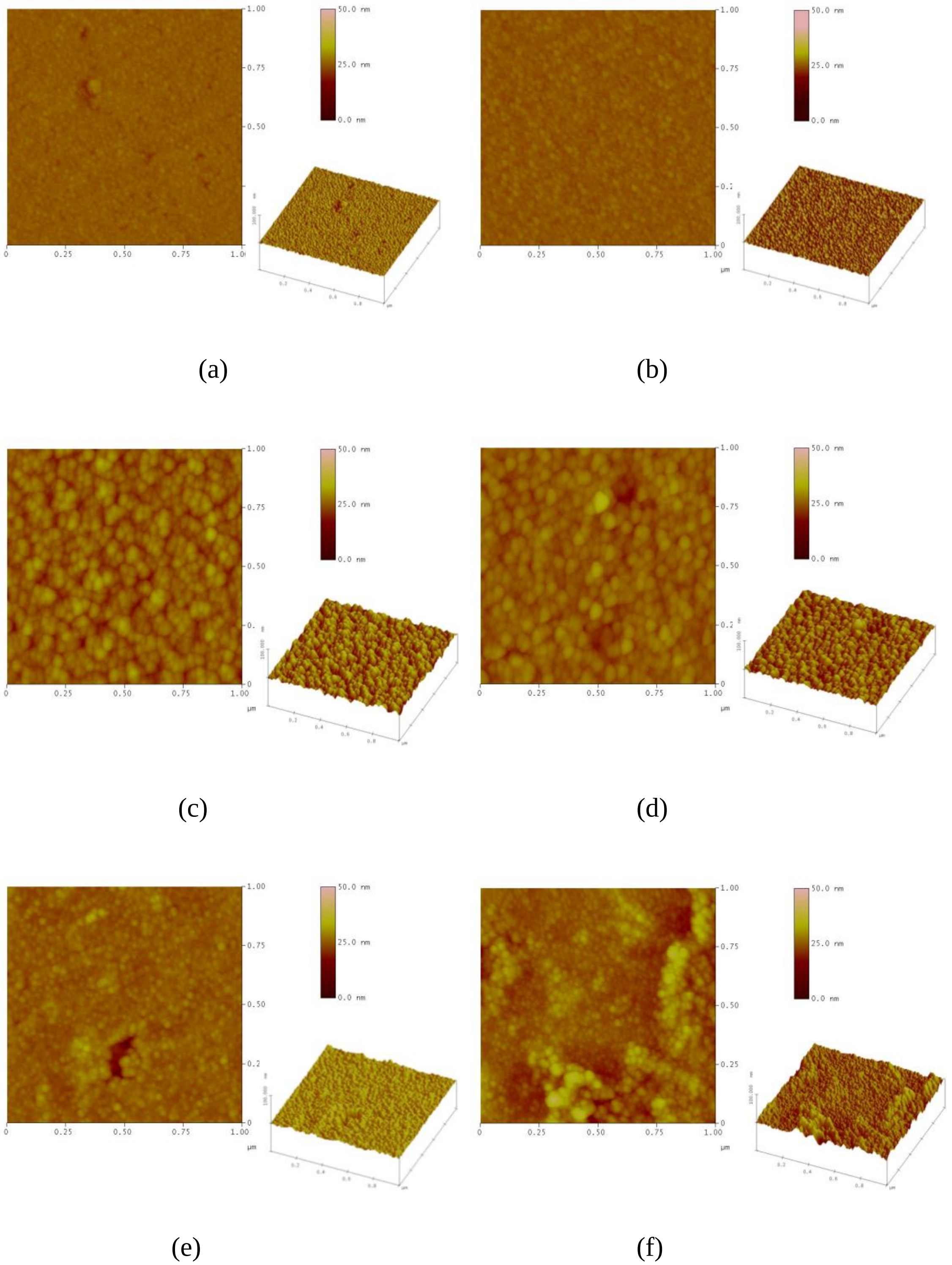

(a) (b)

(c) (d)

(e) (f)

Figure 2.7: AFM topography of 3C-SiC grown on Si (100) and (111) substrates at T_{sub} = 700 ^oC. (a) T_{C60} = 450 ^oC, Si (100). (b) T_{C60} = 450 ^oC, Si (111). (c) T_{C60} = 550 ^oC, Si (100). (d) T_{C60} = 550 ^oC, Si (111). (e) T_{C60} = 650 ^oC, Si (100). (f) T_{C60} = 650 ^oC, Si (111).

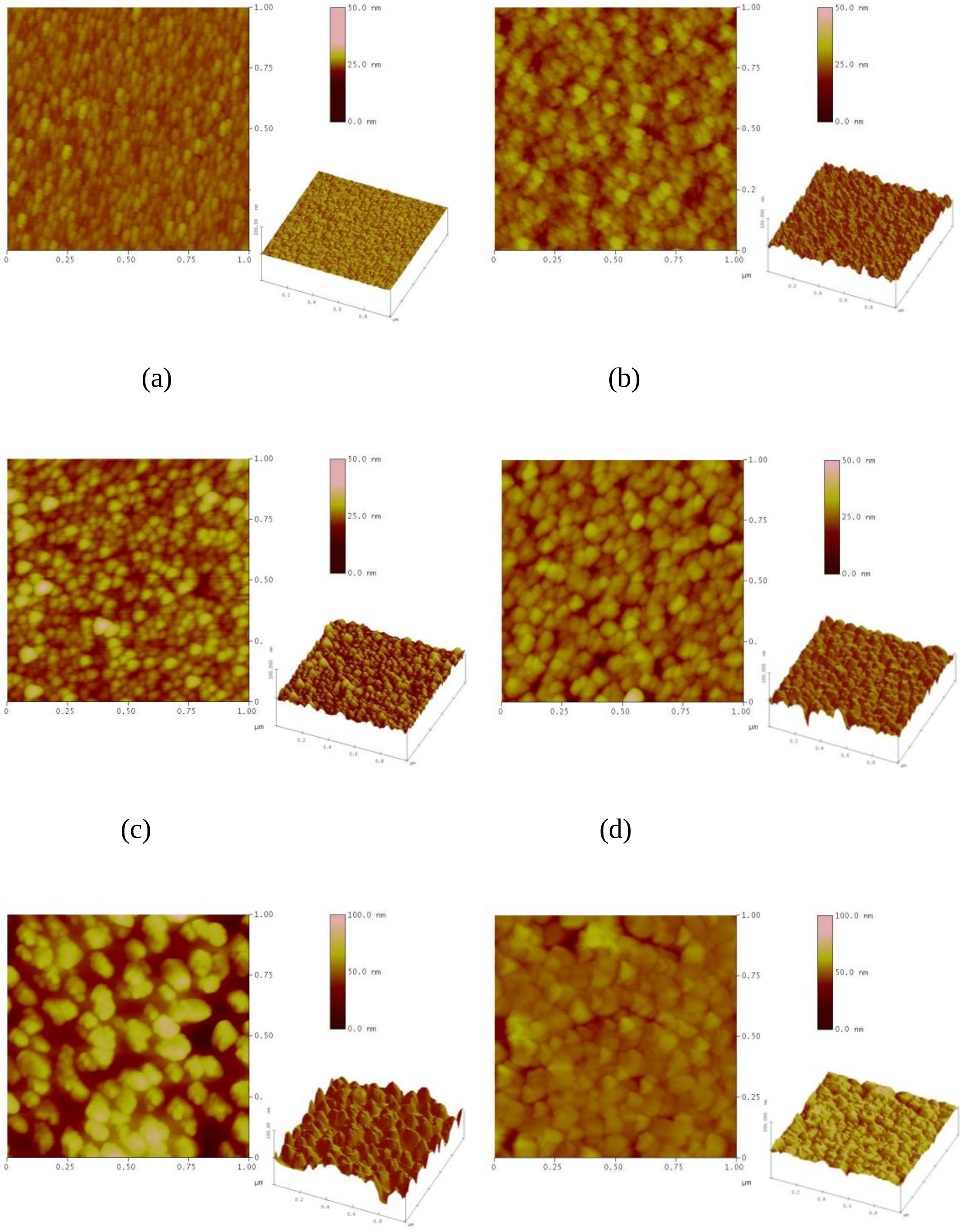

(a) (b)

(c) (d)

(e) (f)

Figure 2.8: AFM topography of 3C-SiC grown on Si (100) substrates. (a) T_{sub} = 800 ^{o}C, T_{C60} = 450 ^{o}C. (b) T_{sub} = 800 ^{o}C, T_{C60} = 550 ^{o}C. (c) T_{sub} = 900 ^{o}C, T_{C60} = 450 ^{o}C. (d) T_{sub} 900 ^{o}C, T_{C60} = 550 ^{o}C. (e) T_{sub} = 1000 ^{o}C, T_{C60} = 450 ^{o}. (f) T_{sub} = 1000 ^{o}C, T_{C60} = 550 ^{o}C.

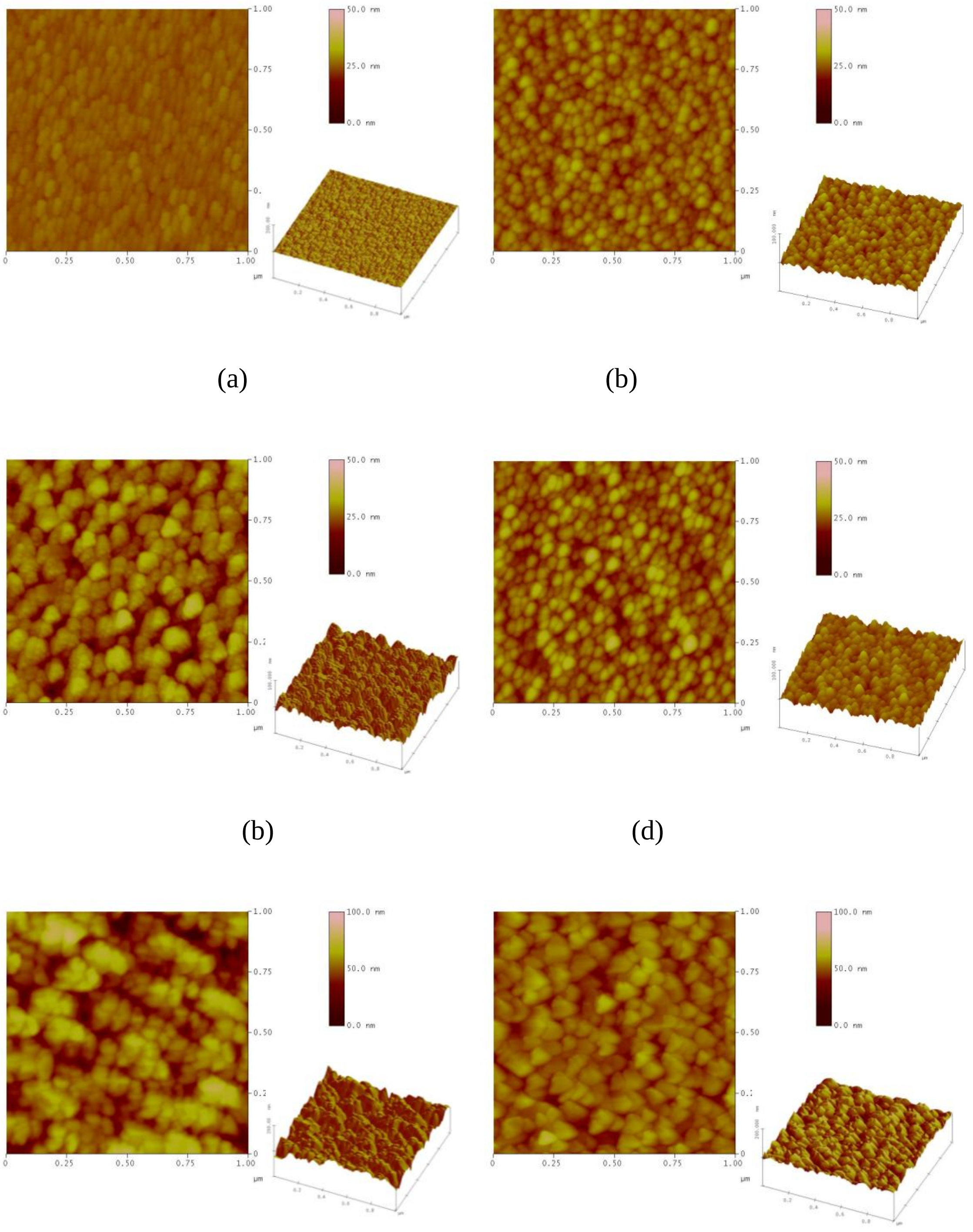

(a) (b)

(b) (d)

(e) (f)

Figure 2.9: AFM topography of 3C-SiC grown on Si (111) substrates. (a) T_{sub} = 800 ^oC, T_{C60} = 450 ^oC. (b) T_{sub} = 800 ^oC, T_{C60} = 550 ^oC. (c) T_{sub} = 900 ^oC, T_{C60} = 450 ^oC. (d) T_{sub} = 900 ^oC, T_{C60} = 550 ^oC. (e) T_{sub} = 1000 ^oC, T_{C60} = 450 ^oC. (f) T_{sub} = 1000 ^oC, T_{C60} = 550 ^oC.

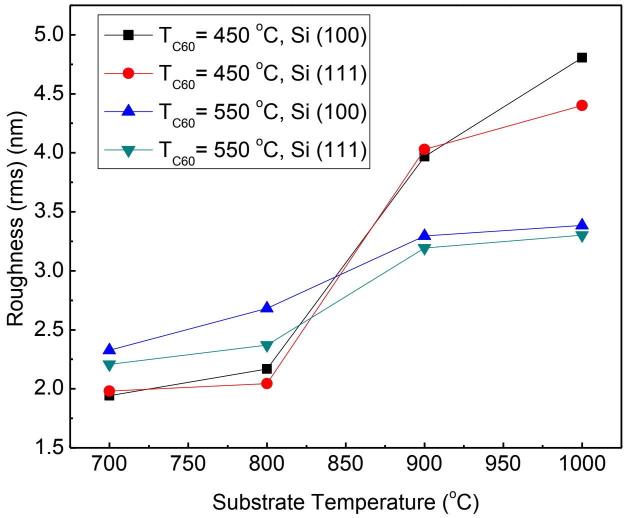

Figure 2.10: AFM roughness (rms) comparison of 3C-SiC grown on Si (100) and (111) at different growth conditions.

To characterize the crystallinity and phonon structures of 3C-SiC films, XRD (PANalytical Inc, Netherland) and Raman spectroscopy (LabRAM HR800, Horiba Jobin Yvon Inc.) were performed on these samples. In XRD setup, the x-ray source is monochromatic Cu (Kα1) with wavelength λ = 1.54056 Å. Triple-axis and rocking-curve configurations were used to scan two theta and omega, respectively. The XRD spectra of the samples grown in DOE (I) are shown in Figure 2.11 (a) and (b). For 3C-SiC films grown on Si (100) substrate, only two samples grown at the substrate/source temperatures are 900/550 ^{o}C and 1000/550 ^{o}C show XRD peaks at $2\theta = 41.5^{o}$ corresponding to 3C-SiC (200) or 6H-SiC (104) planes, which means SiC thin film (if any) grown at other conditions are either amorphous or not well-crystallized. The zoom-in of the peak at $2\theta = 41.5^{o}$ shown in Figure 2.12 (a) indicates the peak is composed of two subpeaks at 41.12^{o} and 41.42^{o}, which correspond to 3C-SiC (200) and 6H-SiC (104), respectively. According to Bragg law, we have Equation (3) as below

$$2d \sin\theta = n\lambda \tag{3}$$

The *d*-spacings of the two types of SiC polytype films, 3C and 6H, are both larger than those of single crystal counterparts, respectively, meaning the crystallization is low and polycyrstalline. The XRD two theta peak of SiC film grown at 1000/550 ^{o}C is shown in Figure 2.13. It is a single peak before and after Lorentzain decomposition and the two theta of 3C-SiC grown at 1000/550 ^{o}C is 41.38^{o} which is very close to that of single crystal 3C-SiC, i.e., 41.385^{o}. Therefore, the *d*-spacing of 3C-SiC film is very close to that of single crystal and 3C phase dominates SiC film. Moreover, the FWHM of 3C-SiC film grown at 1000/550 ^{o}C is much narrower than that of 3C- or 6H- SiC grown at 900/550 ^{o}C. There is a possibility that the two wavelengths of X-ray resulting from unfiltered X-ray source cause two close peaks which are easy to be misinterpreted as two crystalline planes. In order to exclude this possibility, the two theta peak of Si (111) was plotted and inspected in close view as shown in Figure 2.14. It is obvious that the single peak of Si (111) indicates the monochromatic X-ray source. As for those SiC film grown on Si (111) substrates, Figure 2.11 (b) shows all samples grown at T_{C60} = 550 ^{o}C have peaks at about 35.5^{o} corresponding to 3C-SiC (111) or 6H-SiC (102). For those sample grown at T_{C60} = 450 ^{o}C, only the sample grown at T_{sub} = 800 ^{o}C has a two theta peak at about 35.5^{o} which can be Lorentzian-decomposed into two subpeaks: 35.45^{o} corresponding to 3C-SiC (111) and 35.80^{o} corresponding to 6H-SiC (102), as summarized in Table 2.4; all other samples grown at 700/450, 900/450, and 1000/450 ^{o}C do not show such a peak at about 35.5^{o}. This means that 800/450 ^{o}C is a better combination than others with T_{C60} = 450 ^{o}C in growth of uniform crystalline SiC film because the out-diffusion of Si from Si substrate determines the equilibrium and kinetic process in formation, nucleation, and growth of

SiC film on Si (111) substrate. In addition, two tiny peaks at $2\theta = 61.6^{o}$ and 76.3^{o} were observed in Figure 2.11 (a), and two tiny peaks at $2\theta = 25.6^{o}$ and 39.1^{o} in Figure 2.11 (b). In comparison with the XRD database, the peak at $2\theta = 61.6^{o}$ probably corresponds to the plane 6H-SiC (110) ($2\theta = 60.1^{o}$), $2\theta = 76.3^{o}$ to Si (331) ($2\theta = 76.4^{o}$), and $2\theta = 39.1^{o}$ to 6H-SiC (103) ($2\theta = 38.2^{o}$). However, no corresponding plane in XRD database was found close to the planes represented by the peak at $2\theta = 25.6^{o}$. According to Bragg's law, the *d*-spacing of the plane group corresponding to the peak at $2\theta = 25.6^{o}$ should be very large, so there might exist a periodic laminar structure in the SiC thin film.

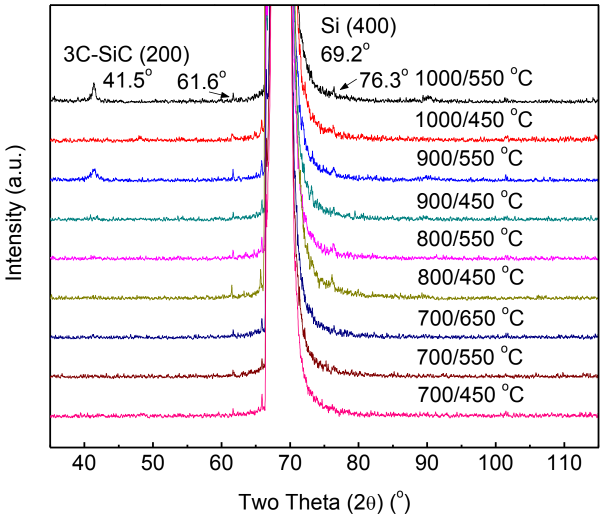

(a)

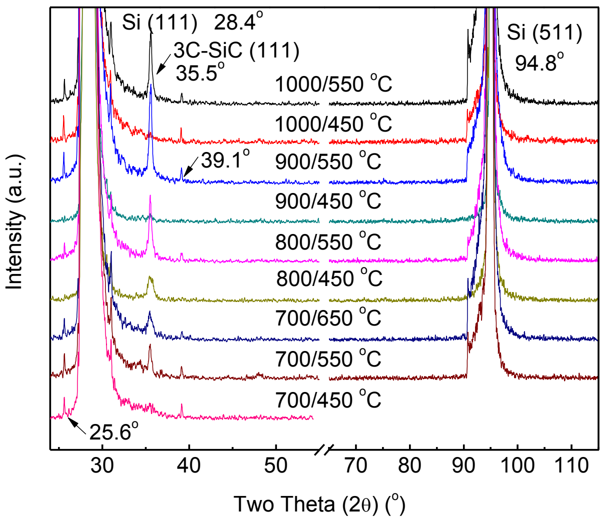

(b)

Figure 2.11: XRD patterns of 3C-SiC thin film grown on Si substrates. (a) Si (100) and (b) Si (111). (Each spectrum is labeled by substrate temperature/source temperature, e.g., 700/450 °C indicates substrate and source temperatures are 700 and 450 °C, respectively).

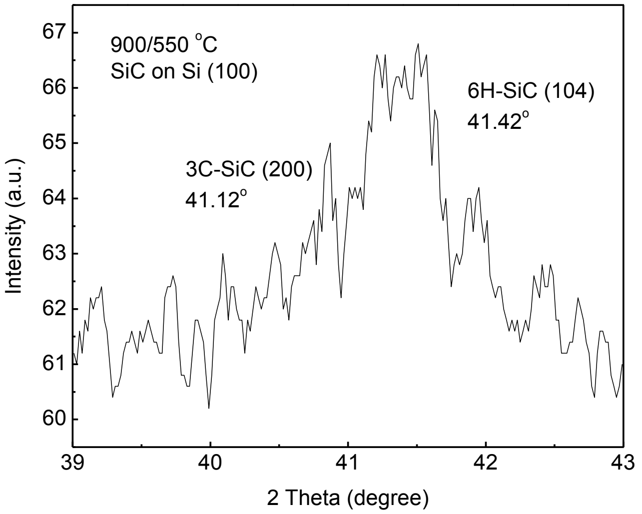

(a)

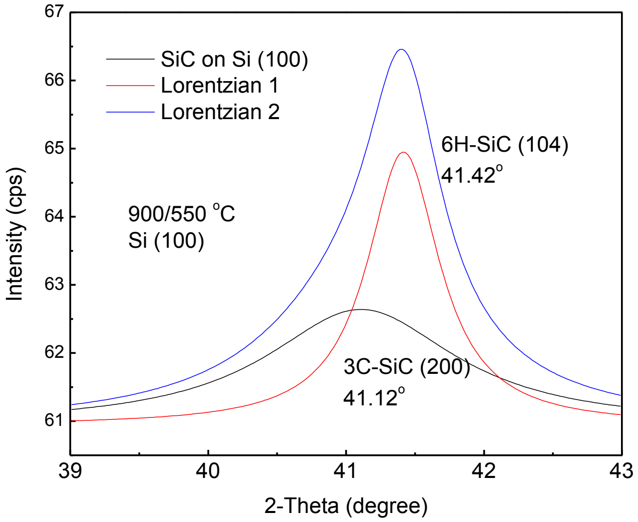

(b)

Figure 2.12: XRD two theta (2θ) peak of SiC grown on Si (100) at the temperatures of T_{sub}/T_{C60} = 900/450 °C. (a) Original data. (b) After Lorentzian deconvolution.

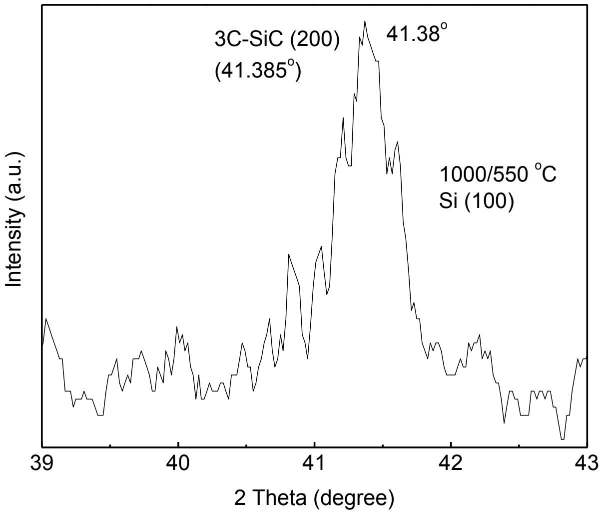

Figure 2.13: XRD two theta (2θ) peak of 3C-SiC grown on Si (100) at the temperature of T_{sub}/T_{C60} = 1000/550 °C.

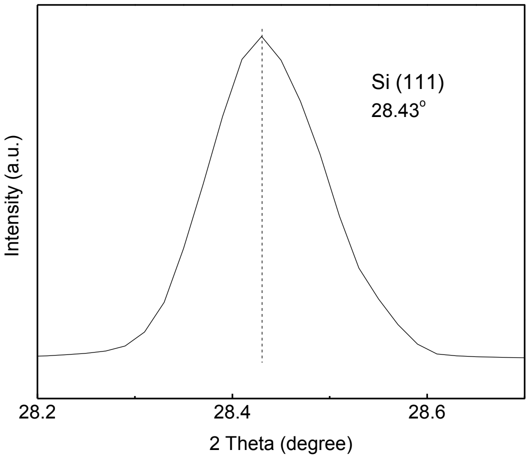

Figure 2.14: XRD two theta peak (2θ) of Si (111).

Figure 2.15 (b) shows the two components resulting from Lorentzian decomposition of the two-theta peak at about 35.6°. The two components of 35.45° and 35.80° corresponds to 3C-SiC (111) (2θ = 35.598°) and 6H-SiC (102) (2θ = 35.729°), respectively. Figure 2.16 shows the two-theta peak before and after Lorentzian decomposition of SiC grown on Si (111) at 800/550 °C are 35.53° and 35.50°, which are practically same or closer to that of 3C-SiC. This means that more 3C-SiC crystallizes at T_{sub} = 800 °C when T_{C60} increases from 450 to 550 °C. The comparison of two-theta peaks and associated FWHM before and after Lorentzian decomposition of SiC grown at other conditions are summarized in Table 2.4. The data are plotted and shown in Figure 2.17. Figure 2.17 (a) shows at T_{C60} = 450 or 650 °C, there are more 6H-SiC at T_{sub} =700 or 800 °C than T_{C60} = 550 °C at which 3C-SiC dominates. It can be seen that at $T_{sub/}T_{C60}$ = 800/550 °C, *d*-spacings of both 3C-SiC (111) and 6H-SiC (102) on Si (111) are closer to that of single crystal 3C-SiC (111) than that of single crystal 6H-SiC (102), and the FWHM of 2θ peak of 3C-SiC (111) is smaller than that of 6H-SiC (102). This means at $T_{sub/}T_{C60}$ = 800/550

^{o}C, 3C-SiC dominates SiC polytype film. Another observation from Figure 2.17 is that at 900/550 and 1000/550 ^{o}C, 3C-SiC dominates SiC polytype films on both Si (100) and Si (111).

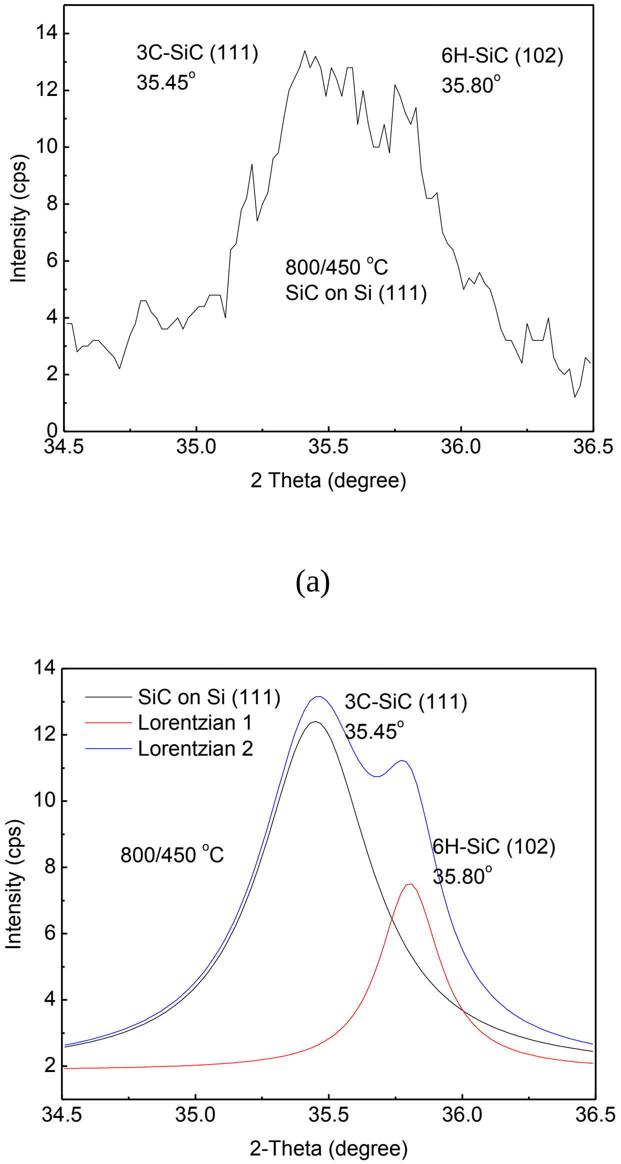

(a)

(b)

Figure 2.15: XRD two theta (2θ) peak of 3C-SiC grown on Si (111) at the temperature of T_{sub}/T_{C60} = 800/450 ^{o}C. (a) Original peak. (b) Lorentzian decomposition.

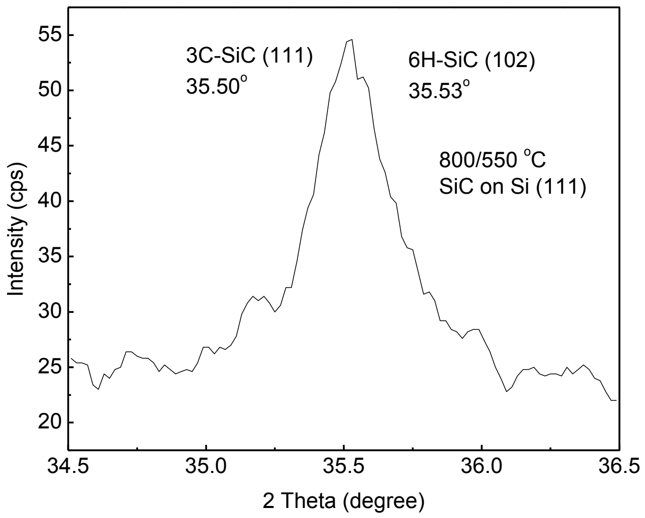

(a)

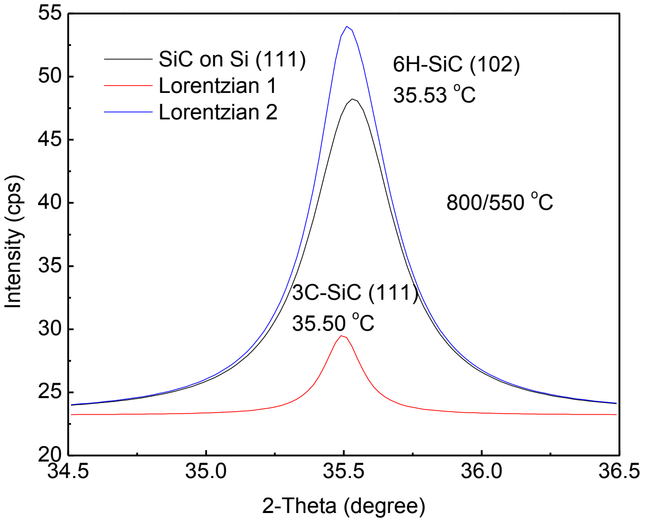

(b)

Figure 2.16: XRD two theta (2θ) peak of 3C-SiC grown on Si (111) at the temperature of T_{sub}/T_{C60} = 800/550 °C. (a) Original peak. (b) Lorentzian decomposition.

Table 2.4: The two-theta and FWHM values of XRD peaks of SiC film on Si (100) and (111) grown at different conditions.

Sub/source/Si	**3C-SiC (111)**		**6H-SiC (102)**	
	2θ (^{o})	FWHM (^{o})	2θ (^{o})	FWHM (^{o})
	35.598		35.729	
700/550/ (111)	35.44267	0.27613	35.56111	0.20185
700/650/ (111)	35.45089	0.50542	35.78001	0.16293
800/450/ (111)	35.44955	0.50299	35.80277	0.27377
800/550/ (111)	35.49629	0.16676	35.5342	0.36962
900/550/ (111)	35.46346	0.2375	35.61767	0.21018
1000/550/ (111)	35.44824	0.09288	35.58803	0.29688
	3C-SiC (200)		**6H-SiC (104)**	
	2θ (^{o})	FWHM (^{o})	2θ (^{o})	FWHM (^{o})
	41.385		41.504	
900/550/ (100)	41.10751	1.68388	41.41637	0.6416
1000/550/ (100)	41.38555	0.44686	41.38555	0.44686

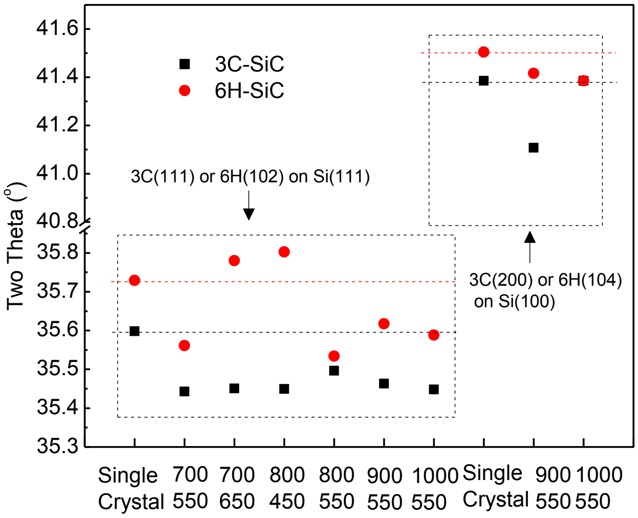

Figure 2.17: Two-theta (2θ) values of XRD peaks of SiC film grown on Si (100) and (111) at different T_{sub}/T_{C60} temperatures. (e.g., in $\frac{700}{550}$, 700 and 500 represent substrate and source temperatures, respectively).

As a complementary characterization to XRD, μ-Raman spectroscopy was performed on these samples in a backscattering configuration. A Nd-YAG solid state laser of 532 nm wavelength and 2-3 mW was used as the excitation source. A 100 X lens with numerical aperture (NA) of 0.9 and working distance (WD) of 0.21 mm was used to focus laser beam onto the test points. The theoretical spot size of laser beam can be calculated by

$$d = \frac{1.22\,\lambda}{NA} \cong 721\ (\mathrm{nm}) \qquad (4)$$

The acquired Raman spectra of all samples are plotted and stacked in Figures 2.18 – 2.20 in consistent with XRD patterns shown in Figures 2.11 (a) and (b), all Raman spectra of those samples grown on Si (111) at 550 ^{o}C show characteristic TO modes of 6H-SiC and 3C-SiC at about 764 and 792 cm^{-1}, respectively, which are slightly redshifted compared with 767 and 796 cm^{-1} of single crystals. This is due to biaxial tensile strain resulting from the lattice mismatch between SiC and Si. The peaks at 618, 670 and 822 cm^{-1} are from Si substrates. The second TO lines at 1519 and 1713 cm^{-1} are also observed from the spectra of SiC on Si (100) and Si (111) at 800/550, 900/550, and 1000/550 ^{o}C. Since both 3C-SiC and 6H-SiC has two second order modes, it is hard to distinguish unambiguously the origins of two modes. Peaks at 1296, 1449 and 1555 cm^{-1} are from Si substrates. One obvious observation from the Raman spectra of SiC polytype films grown on Si (100) and Si (111) at T_{sub}/ T_{C60} = 700/550 ^{o}C and 700/560 ^{o}C shown in Figure 2.18 (b) and Figure 2.19 (b) are two broad peaks at about 1367 to 1605 cm^{-1} standing out. It is due to the decomposition of excessive C60, which is in agreement with the variation of Raman spectrum of C60 with the temperature shown in Figure 2.21. For both Si (111) and (100) substrates, Raman spectra of SiC grown at T_{sub}/ T_{C60} = 700/650 ^{o}C show much stronger and broarder peaks at 1367 to 1605 cm^{-1} than that at T_{sub}/ T_{C60} = 700/550 ^{o}C does, indicating more decomposed C60 on SiC grown at T_{sub}/ T_{C60} = 700/650 ^{o}C than that at T_{sub}/ T_{C60} = 700/550 °C due to the larger C60 evaporation flux at T_{sub}/ T_{C60} = 700/650 °C.

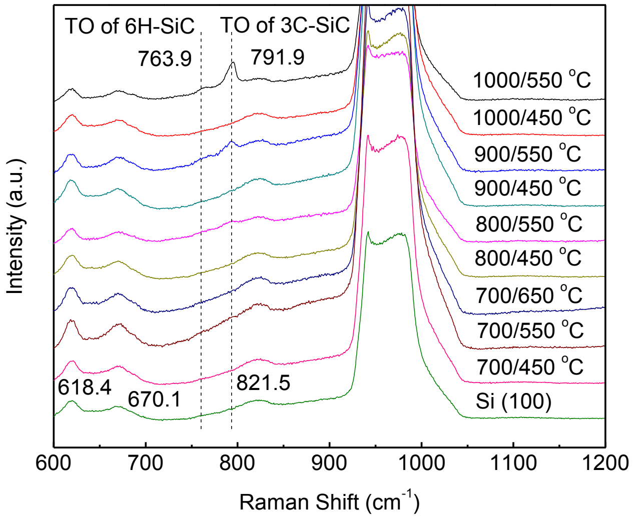

(a)

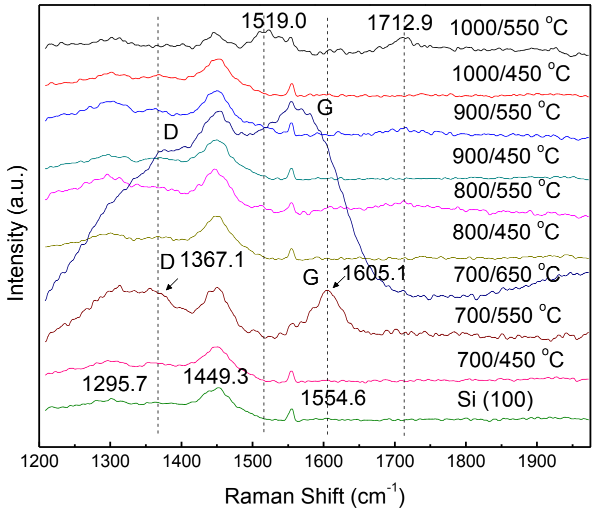

(b)

Figure 2.18: Raman spectra of SiC polytype films grown on Si (100) at different temperature conditions

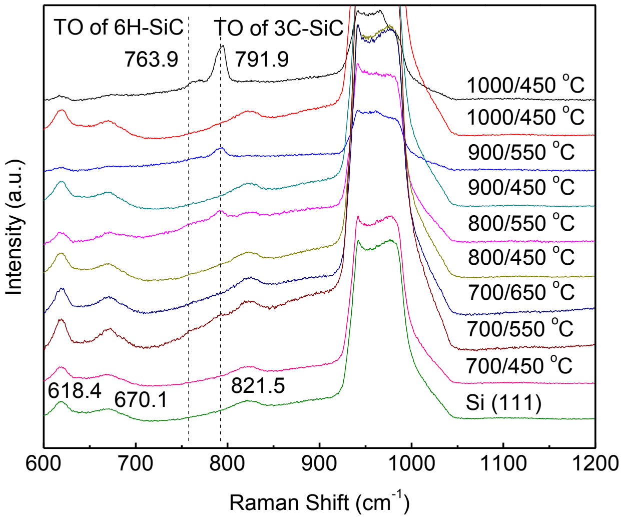

(a)

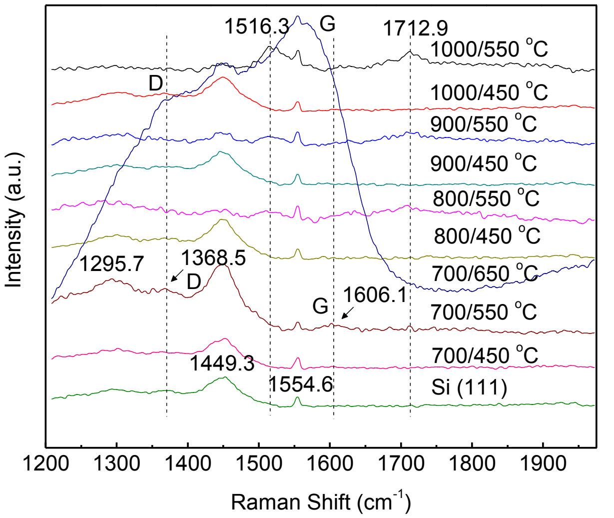

(b)

Figure 2.19: Raman spectra of SiC polytype films grown on Si (111) at different temperature conditions.

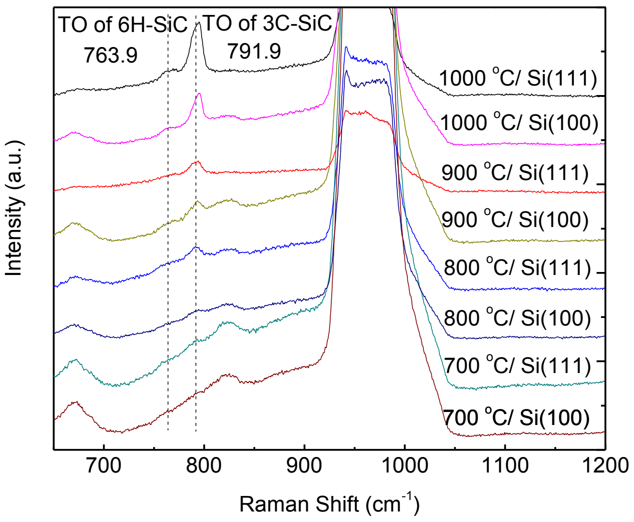

(c)

Figure 2.20: Raman spectra of SiC polytype films grown on Si (100) and (111) at the C60 source temperature of 550 °C.

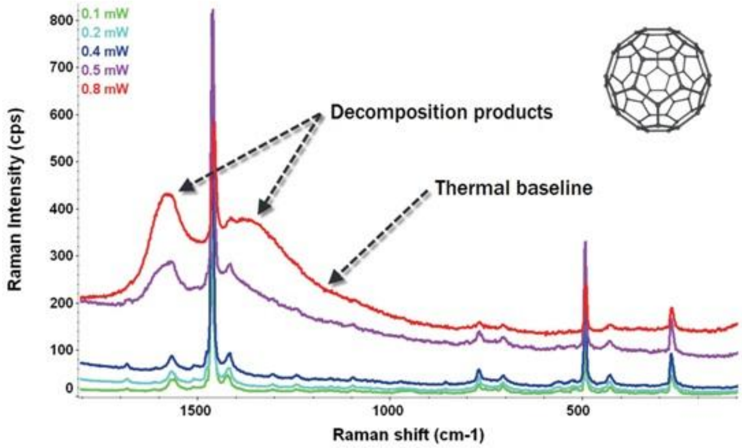

Figure 2.21: The variation of Raman spectrum of C60 with the laser power [186].

In fact, the TO mode of 792 cm^{-1} is the convolution of two subpeaks: one is TO of 6H-SiC and the other is TO of 3C-SiC. Figures 2.22 (a) and (b) show Lorentzian decomposition of the peak at 792 cm^{-1}. According to the phonon mode frequencies of common SiC polytypes listed in Table 2.5 [187], two peaks of 765 and 791 cm^{-1} in Figure

2.22 (a) and two peaks of 765 and 790 cm^{-1} in Figure 2.22 (b) are TO modes of 6H-SiC, and peaks of 796 cm^{-1} in Figure 2.22 (a) and 796 cm^{-1} in Figure 2.22 (b) are TO modes of 3C-SiC. The TO mode of 792 cm^{-1} of SiC polytype films grown at other conditions are decomposed and the decomposed the Lorentzian subpeaks are listed in Table 2.6. All experimental Raman frequencies of SiC polytype films grown at different temperature conditions are summarized and listed in Table 2.6. Therefore, both 3C-SiC and 6H-SiC co-exist in the SiC polytype films grown on Si (100) and (111) substrates.

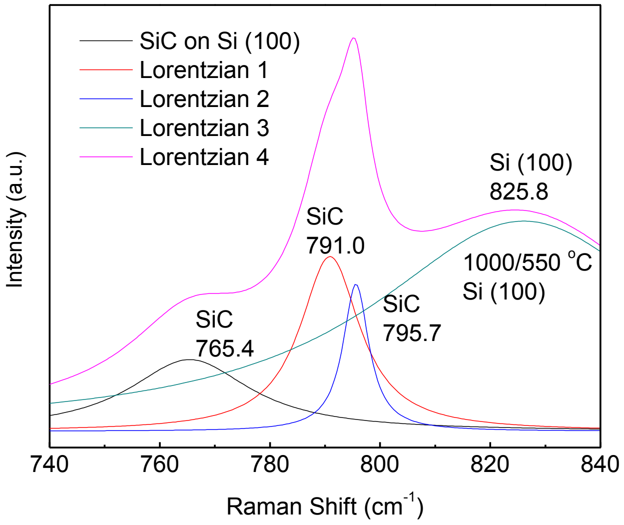

(a)

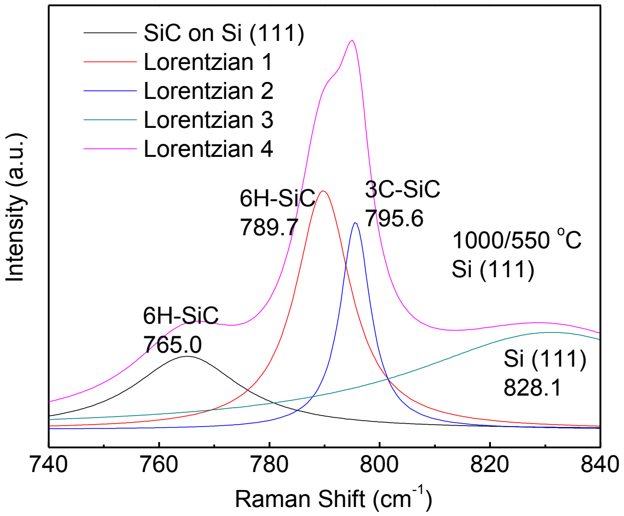

(b)

Figure 2.22: Raman spectra of TO modes of 3C- and 6H- SiC polytypes after Lorentzian decomposition of convoluted peaks.

Table 2.5: Positions of Raman bands for common SiC polytypes in the range of 600-1100 cm^{-1} [187] (The stronger bands are in bold).

SiC polytype	**Raman band position [cm^{-1}]**											
	TA			LA			TO			LO		
3C (*β*)							**796**			**972**		
2H (*α*)	264						**764**	799		**968**		
4H (*α*)	196	204	266	610			**776**	796		838	**964**	
6H (*α*)	**145** **241**	**150** **266**	**236**	**504**	**514**		**767**	**789**	797	889	**965**	
15R (*α*)	**167** **256**	**173**	**255**	**331** **577**	**337**	**569**	**767**	**789**	**797**	800 956	932	938

Table 2.6: Experimental Raman frequencies of SiC grown on Si (100) and (111)

Experimental Raman frequencies of SiC thin film grown on Si [cm^{-1}]							
700/450/ Si (100)		770.5					
700/450/ Si (111)		775.9					
800/450/ Si (100)		768.2					
800/450/ Si (111)	764.5		788.9				√
900/450/ Si (100)	764.3		789.1				
900/450/ Si (111)		774.1					
1000/450/ Si (100)	764.1		787.6				
1000/450/ Si (111)	763.1		787.6				
700/650/ Si (100)		770.4					
700/650/ Si (111)		773.3					√
700/550/ Si (100)	760.1		785.3				
700/550/ Si (111)	762.8		787.8				√
800/550/ Si (100)	765.0			790.4		1519.0	1712.9
800/550/ Si (111)	764.5			791		1516.3	1712.9√
900/550/ Si (100)	765.4			791.9		1519.0	1712.9√
900/550/ Si (111)	766.5			791.7		1516.3	1712.9√
1000/550/ Si (100)	765.4			791	795.7	1519.0	1712.9√
1000/550/ Si (111)	765.0		789.7		795.6	1516.3	1712.9√
Corresponding Raman frequencies of SiC polytypes [cm^{-1}]							
Modes	TO		TO	TO	TO	2nd TO	2nd TO
3C (β)					796 [261]		
6H (α)	**767** [187]		**789** [187]			1516 [188]	1714 [188]

(Note: √ indicates the corresponding XRD spectrum shows a 2-theta peak).

It can be seen from Table 2.6 that, at temperature combinations of T_{sub}/ T_{C60} = 700/450 °C, SiC films grown on both Si (100) and Si (111) are amorphous 6H-SiC. SiC grown on Si (100) at T_{sub}/ T_{C60} = 800/450 °C, SiC grown on Si (111) at T_{sub}/ T_{C60} = 900/450 °C, and SiC films grown on both Si (100) and (111) at T_{sub}/ T_{C60} = 700/650 °C are also amorphous. SiC film grown on Si (111) at T_{sub}/ T_{C60} = 700/550, 800/450 °C and 1000/450 °C are crystalline 6H-SiC, so are SiC film grown on Si (100) at T_{sub}/ T_{C60} = 700/550, 900/450 °C and 1000/450 °C. At the combination temperature are higher than T_{sub}/ T_{C60} = 800/550 °C, SiC films grown on both Si (100) and (111) are coexistence of 6H-SiC and 3C-SiC, and 3C-SiC are well crystallized at T_{sub}/ T_{C60} = 1000/550 °C.

After the identification of 550 ^{o}C as a better source temperature, the crystallization of 3C-SiC thin films grown at different substrate temperatures of 800, 900, and 1000 ^{o}C was investigated by omega (ω) scan and omega-2 theta (ω-2θ) scan, as shown in Figures 2.23 and 2.24. FWHM$_{\omega}$ decreases significantly with the the increasing substrate temperature, indicating the lateral coherence of SiC film increases significantly with the increasing temperature from 800 to 1000 ^{o}C, becuase the lateral diffusion of carbon and silicon atoms increases exponentially with the increasing temperature (Figure 2.23). The decrease in FWHM$_{\omega}$ from 900 to 1000 ^{o}C is larger than that from 800 to 1000 ^{o}C for SiC film on both Si (100) and (111), implying T_{sub} = 1000 ^{o}C is much more effective in improving crystallization than T_{sub} = 1000 ^{o}C. However, the FWHM$_{\omega-2\theta}$ decreases significantly from 800 to 900 ^{o}C but slightly from 900 to 1000 ^{o}C for SiC on Si (100), indicating vertical coherence is very low at T_{sub} = 800 ^{o}C, and increases significantly from T_{sub} = 900 to 1000^{o}C because of the low area atomic density of Si (100) (Figure 2.24 a). In contrast, FWHM$_{\omega-2\theta}$ decreases slightly from T_{sub} = 800 to 1000^{o}C for SiC on Si (111), meaning the vertical coherence increases slightly with T_{sub} = 800 to 1000^{o}C due to the high area atomic density of Si (111). Another obsersation is the samller $(\omega - 2\theta)$ value at T_{sub} = 800 ^{o}C than at T_{sub} = 900 and 1000^{o}C, indicating the compressive strain in SiC on Si (111) at T_{sub} = 800 ^{o}C.

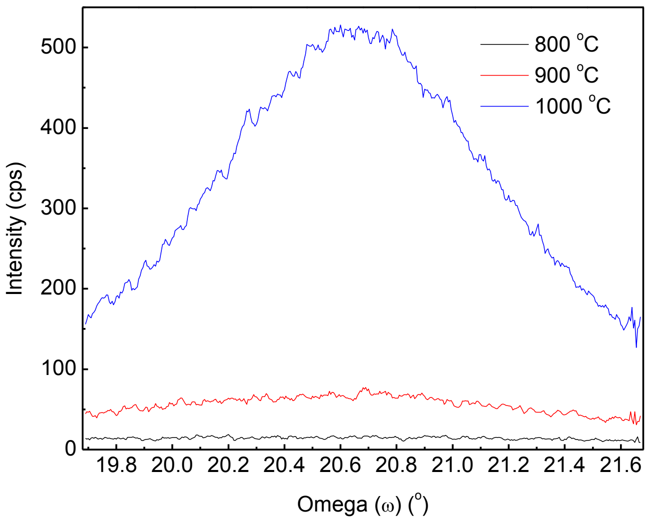

(a)

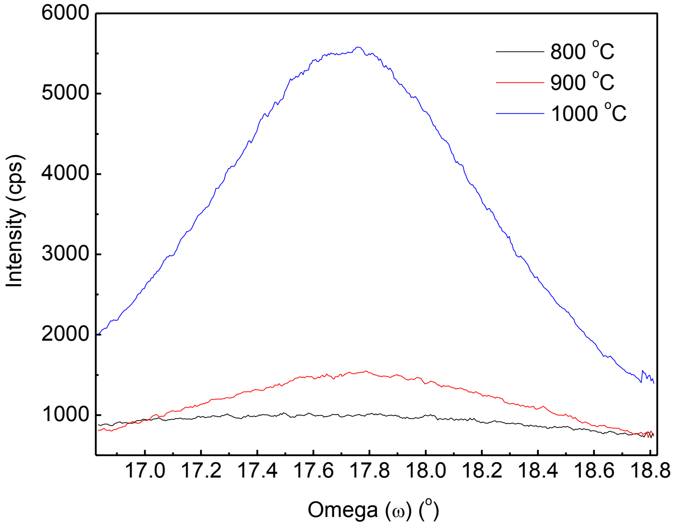

(b)

Fig. 2.23 XRD rocking-curve of 3C-SiC thin films grown on Si substrates at source temperature of 550 °C and different substrate temperatures of 800, 900, and 1000 °C. (a) SiC on Si (100). (b) SiC on Si (111).

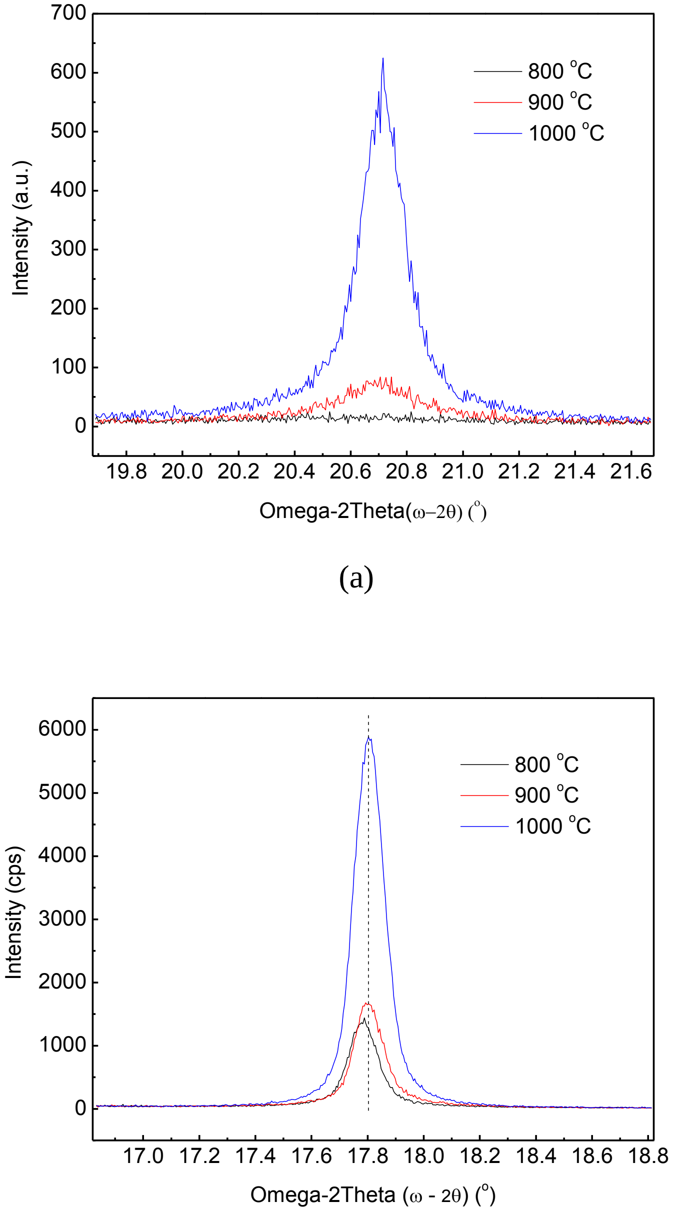

(a)

(b)

Figure 2.24: XRD Omega-2Theta (ω-2θ) curve of 3C-SiC thin films grown on Si substrates at source temperature of 550 °C and different substrate temperatures of 800, 900, and 1000 °C. (a) SiC on Si (100). (b) SiC on (111).

2.5 Characterization and analyses of samples grown on Si (100), Si (110), and Si (111)

To investigate and compare the effect of the Si substrates orientations on SiC films, three Si wafters with different orientations of (100), (110), and (111) were loaded into the MBE chamber simultaneously. The first three different Si wafer substrates were grown at T_{sub}/T_{C60} = 800/550 ^{o}C for 10 minutes. The second three different Si wafer substrates were grown at T_{sub}/T_{C60} = 1000/550 ^{o}C for 20 minutes. The morphology and topography of SiC films were measured with SEM and AFM, respectively. Figures 2.25 and 2.26 show SEM and AFM images of SiC films grown on Si (100), (110) and (111) at T_{sub}/T_{C60} = 800/550 ^{o}C for 10 min. and T_{sub}/T_{C60} = 1000/550 ^{o}C for 20 min., respectively. The surface roughness of the SiC films on Si (100), (110), and (111) is compared and plotted in Figure 2.27. It can be seen that SiC grown at T_{sub}/T_{C60} = 1000/550 ^{o}C is always rougher than their counterpart at T_{sub}/T_{C60} = 800/550 ^{o}C. In general epitaxial growth, the smoothness increases with substrate temperature, but in this study, we found the both grain size and roughness increase with the increasing substate temperatue. This is because the SiC film is formed through inter-diffusion of silicon (from Si substrate) and carbon (from effusive cell) via formed SiC, making the SiC forming mechanism more complicated than normal epitaxial growth (e.g., GaN on sapphire). Moreover, at T_{sub}/T_{C60} = 800/550 ^{o}C, roughness $R_{SiC\ on\ Si\ (100)} > R_{SiC\ on\ Si\ (111)} > R_{SiC\ on\ Si\ (110)}$, but at T_{sub}/T_{C60} = 1000/550 ^{o}C, $R_{SiC\ on\ Si\ (100)} > R_{SiC\ on\ Si\ (110)} > R_{SiC\ on\ Si\ (111)}$. This is because the area atomic density of Si (100) is the lowest, that of Si (110) is the highest, and that of Si (111) falls in between. The atomic distribution of three Si planes (100), (110) and (111) are shown in Figure 2.28, and the area atomic density of three Si planes are calculated and listed in Table 2.7. Since the area atomic density of SiC formed on Si is proportional to that of Si surface for a short growing time, the roughness $R_{SiC\ on\ Si\ (100)} > R_{SiC\ on\ Si\ (111)} > R_{SiC\ on\ Si\ (110)}$ is reasonable at T_{sub}/T_{C60} = 800/550 ^{o}C for 10 min.

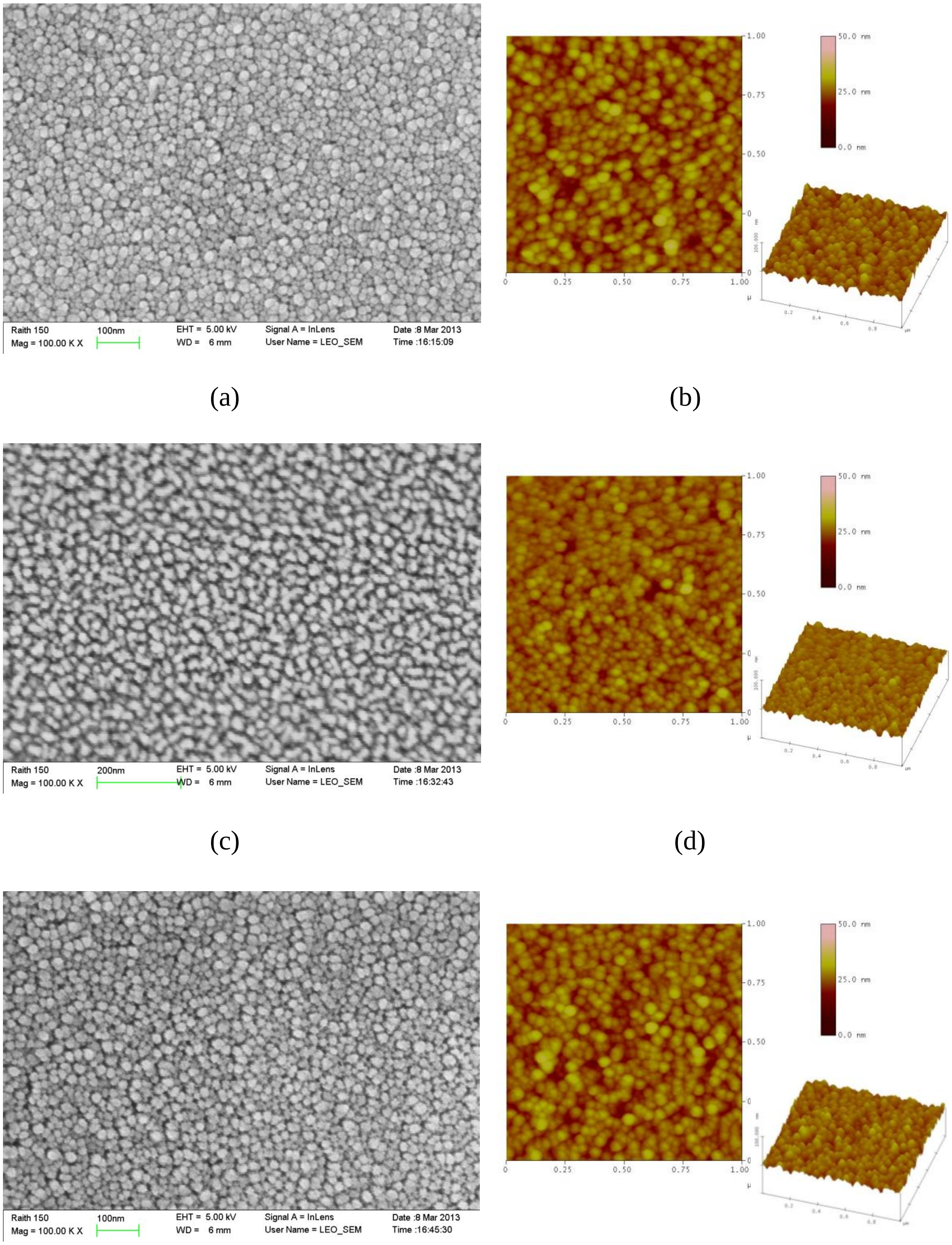

(a) (b)

(c) (d)

(e) (f)

Figure 2.25: SEM and AFM images of 3C-SiC grown on Si (100), (110) and (111) at T_{sub}/T_{C60}=800/550 ^{o}C for 10 minutes. (a) SEM of 3C-SiC on Si (100). (b) AFM of 3C-SiC on Si (100). (c) SEM of 3C-SiC on Si (110). (d) AFM of 3C-SiC on Si (110). (e) SEM of 3C-SiC on Si (111). (f) AFM of 3C-SiC on Si (111).

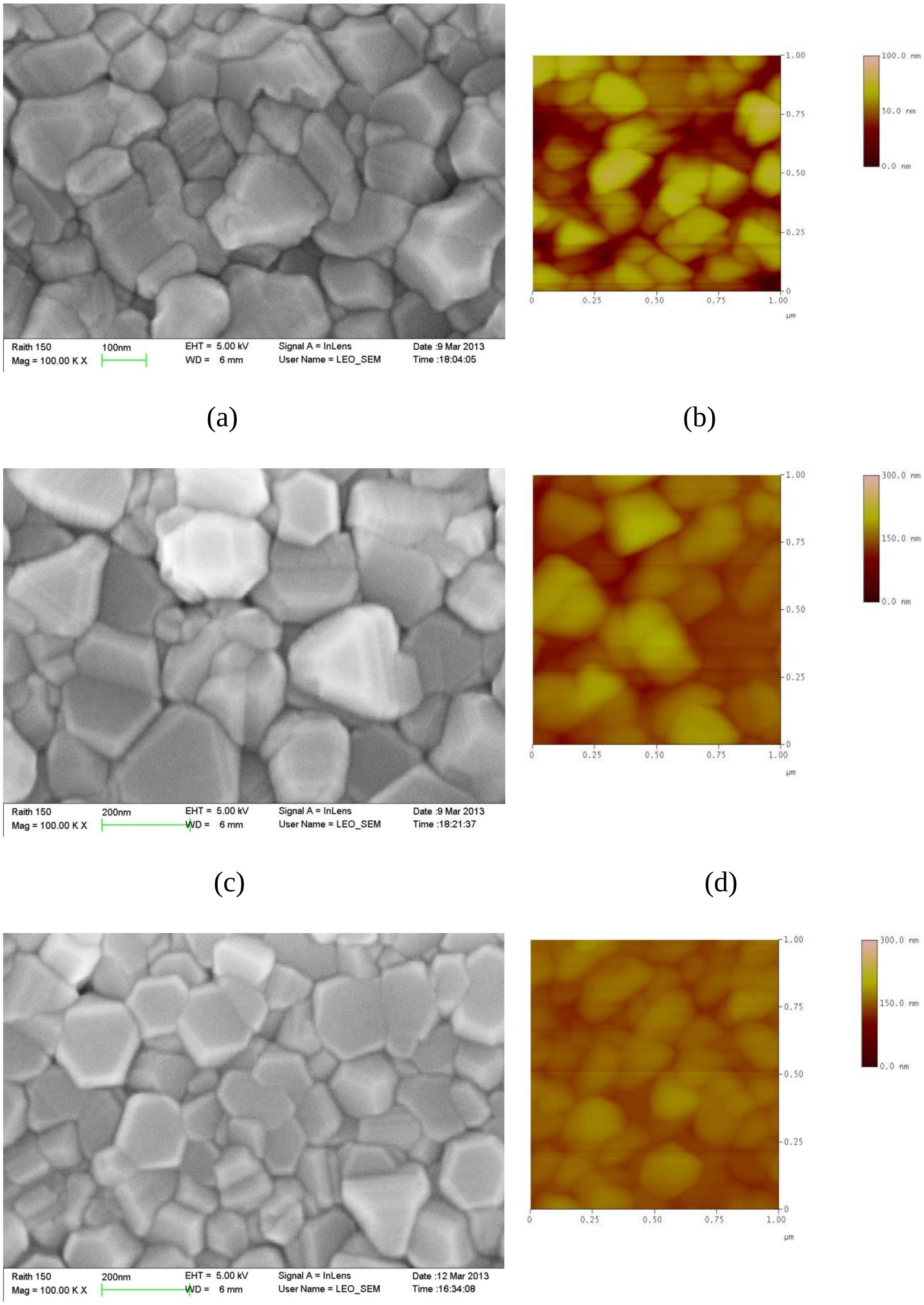

(a) (b)

(c) (d)

(e) (f)

Figure 2.26: SEM and AFM images of 3C-SiC grown on Si (100), (110), and (111) at T_{sub}/T_{C60}=1000/550 °C for 20 minutes. (a) SEM of SiC on Si (100). (b) AFM of SiC on Si (100). (c) SEM of SiC on Si (110). (d) AFM of SiC on Si (110). (e) SEM of SiC on Si (111). (f) AFM of SiC on Si (111).

However, with the increase of substrate temperature and growth time, SiC film become thicker, making it difficult for Si to out-diffuse from the underneath Si substrate, leading to uneven SiC film, especially for the highest area atomic density of SiC on Si (110). As a consequence, excessive decomposed C60 accumulates on SiC surface, contributing to the roughness of SiC film. The SEM image shown in Figure 2.26 (c) displays white particle (decomposed C60) of less than 10 nm in size randomly distributed on SiC film on Si (110). However, the similar white particles are not obviously observed on SiC films on Si (100) and Si (111). These observations are also corroborated by the Raman spectra shown in Figure 2.32 (f) in which Raman peaks at 1358.9 and 1605.4 cm^{-1} are D and G bands of excessive decomposed C60.

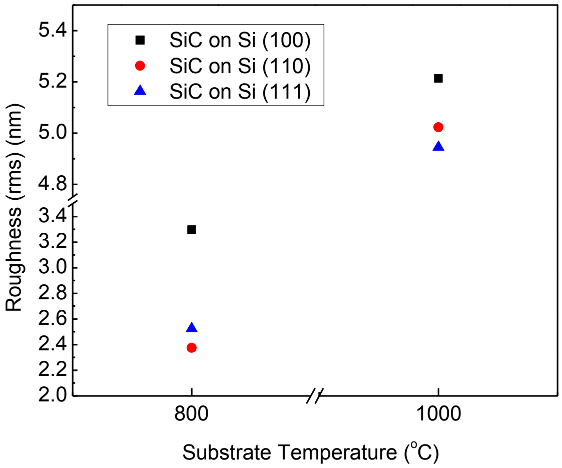

Figure 2.27: Roughness (RMS) comparison of SiC films grown on Si (100), (110) and (111) at T_{sub}/T_{C60} = 800/550 and 1000/550 °C.

Table 2.7: The number of atoms and area atomic density of Si (100), (110) and (111)

Plane orientation	**No. of atoms**	**Density of surface atoms (atoms/cm^2)**
Si (100)	2	6.78×10^{14}
Si (110)	4	9.59×10^{14}
Si (111)	2	7.83×10^{14}

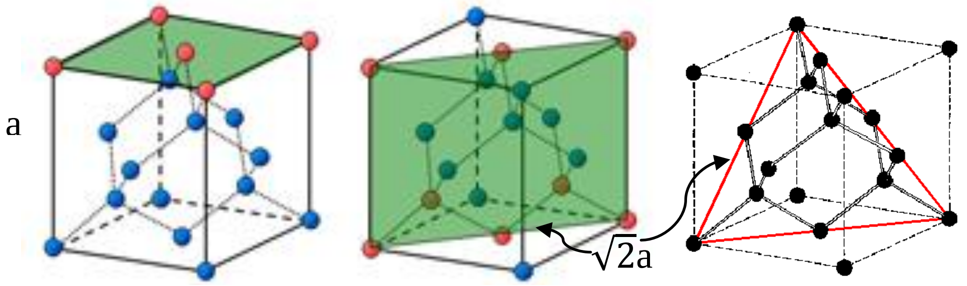

(a) Si (100) (b) Si (110) (c) Si (111)

Figure 2.28: Schematic illustration of atomic distribution of three Si planes. (a) Si (100). (b) Si (110). (c) Si (111).

XRD two-theta scan also were performed on SiC films grown on Si (100), (110), and (111) at $T_{sub}/T_{C60} = 800/550$ and $T_{sub}/T_{C60} = 1000/550\ ^oC$. XRD spectra are shown in Figures 2.29 (a) and (b), respectively. It can be seen 3C-SiC (111) and/or 6H-SiC (102) represented by $2\theta = 35.6^o$ were formed on Si (110) and (111), and 3C-SiC (200) or/and 6H-SiC (104) repsresented by $2\theta = 41.4^o$ were formed on Si (100). Omega scans were also performed on SiC films on three Si plane orientations (100), (110), and (111) and shown in Figures 2.30 (a) and (b). The omega values are calculated and plotted as shown in Figure 2.30 (c). Since the range of omega peak cannot cover the whole peak, it is hard to quantify the FWHM values accurately. From the omega (ω) values, it can be seen that at $T_{sub}/T_{C60} = 800/550\ ^oC$, the omega values of 3C-SiC (200) on Si (100) cannot be surely identified because of the broad and noisy omega peak, that of 3C-SiC (111) on Si (110) is smaller than that of single crystal, and that of 3C-SiC (111) on Si (111) is larger than of single crystal. This means the *d*-spacing of 3C-SiC (111) on Si (111) is smaller than that of single crystal, but d-spacing of 3C-SiC (111) on Si (110) is larger than that of single crystal, implying 3C-SiC (111) films on Si (111) at $T_{sub}/T_{C60} = 800/550$ and $1000/550\ ^oC$ are subject to biaxial tensile strain, and 3C-SiC (111) films on Si (110) at $T_{sub}/T_{C60} = 800/550$ and $1000/550\ ^oC$ are subject to biaxial compressive strain. This can be confirmed by the redshift of LO of 3C-SiC (111) on Si (111) shown in Figure 2.32 (c). Another observation for 3C-SiC (200) on Si (100) is that omega value at T_{sub}/T_{C60} = 1000/550 ^{o}C is closer to that of single crystal than that of T_{sub}/T_{C60} = 800/550 ^{o}C. Therefore, the increase in substrate temperature from 800 to 1000 ^{o}C has more obvious effect on 3C-SiC (200) on Si (100) than 3C-SiC (111) on Si (110) and Si (111).

The crystalline and phonon stucutre of SiC films grown at Si (100), (110) and (111) were also measured with μ-Raman spectroscopy. A 532 nm wavelength Nd-YAG laser with the power of 2-3 mW was focused with 100 × objective lense onto the samples in same acquisition conditions. All spectra were taken in single spectrum window to avoid any potential shift caused by the moving of the grating. The Raman spectra of SiC films grown at T_{sub}/T_{C60} = 800/550 ^{o}C for 10 min. are shown in Figures 2.31 (a) – (c). Figure 2.31 (a) shows that all spectra of SiC on Si (100), (110) and (111) displays the 1st order TO modes of 6H-SiC and 3C-SiC at about 761 and 790 cm^{-1}, respectively. Since the peak of 790 cm^{-1} are actually the combination of two components and the peak intensity is very low, it is hard to compare the relative shift of each spectrum. The Lorentzain decomposition of TO bands of SiC grown on Si (110) is shown in Figure 2.31 (c). There are totally three peaks of 762, 786, and 793 cm^{-1} after Lorentzian deconvolution. The first two peaks are TO bands of 6H-SiC and the third one is TO of 3C-SiC [187]. The spectra in Figure 2.31 (b) show the second order TO at 1517 and 1713 cm^{-1} [187]. The additional peak of 1608.7 cm^{-1} should be G band of the decomposed C60, as shown in Figure 2.21, indicating some excessive carbon atoms on SiC. Figure 2.31 (a) shows TO of SiC grown on Si (110) has the strongest intensity because of the highest area atomic density of SiC on Si (110) resulting from the highest area atomic density of Si (110).

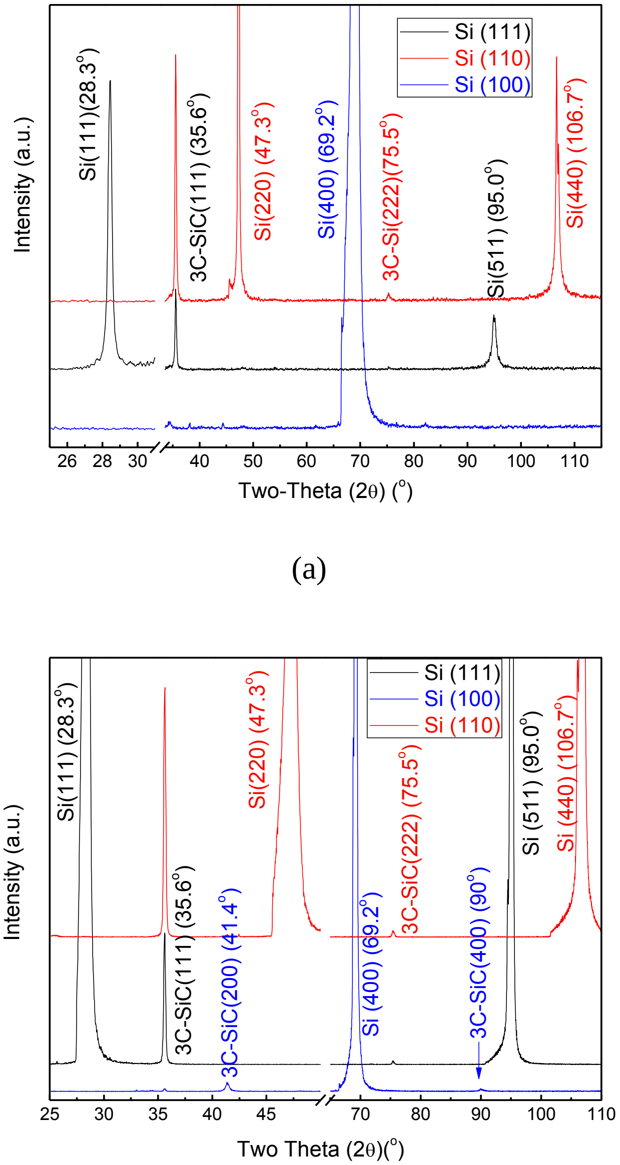

(a)

(b)

Figure 2.29: XRD patterns of 3C-SiC grown on Si (100), (110) and (111). (a) T_{sub}/T_{C60}=800/550 °C for 10 minutes. (b) T_{sub}/T_{C60}=1000/550 °C for 20 minutes.

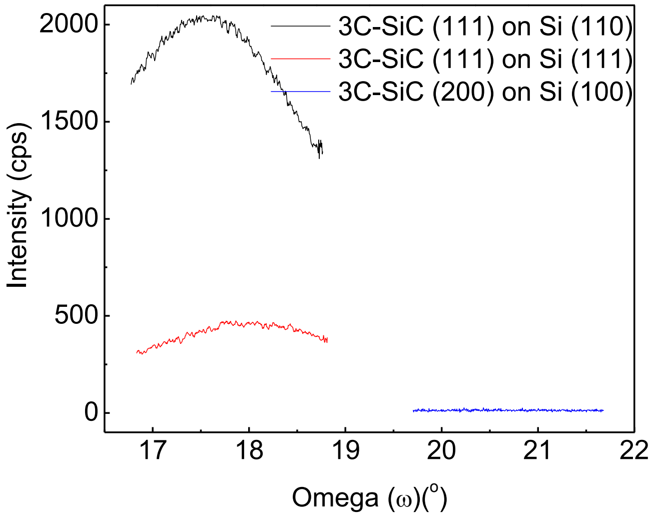
Intensity (cps)
2000
1500
1000
500
0
17
18
19
20
21
22
Omega (ω)(°)
3C-SiC (111) on Si (110)
3C-SiC (111) on Si (111)
3C-SiC (200) on Si (100)

(a)

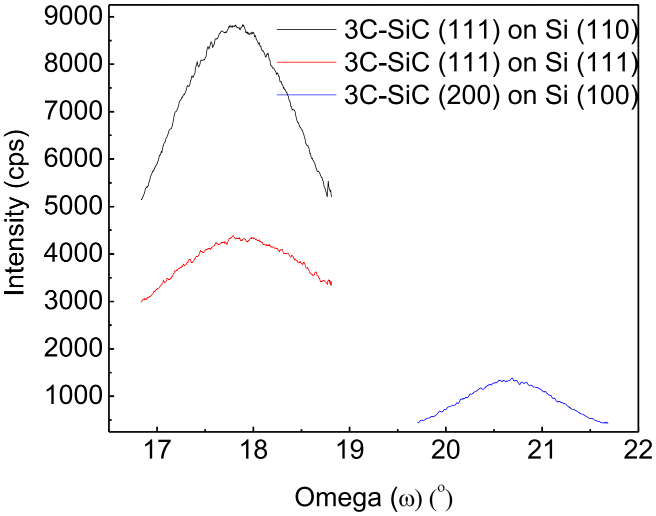
Intensity (cps)
9000
8000
7000
6000
5000
4000
3000
2000
1000
17
18
19
20
21
22
Omega (ω) (°)
3C-SiC (111) on Si (110)
3C-SiC (111) on Si (111)
3C-SiC (200) on Si (100)

(b)

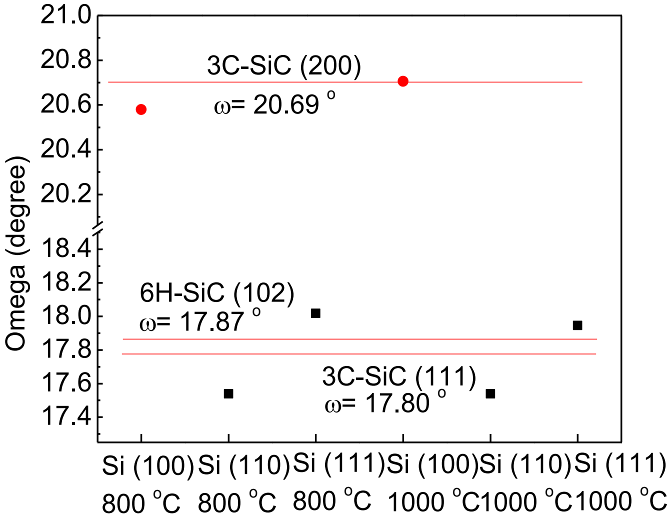

(c)

Figure 2.30: XRD rocking curves of 3C-SiC grown on Si (100), (110) and (111). (a) T_{sub}/T_{C60}=800/550 °C for 10 min. (b) T_{sub}/T_{C60}=1000/550 °C for 20 min. (c) Omega value (the red lines represent the Omega values of single crystals).

The Raman spectra of SiC grown on Si (100), (110) and (111) at T_{sub}/T_{C60}=1000/550 °C for 20 min. are shown in Figures 2.32 (a) to (f). Figure 2.32 (a) and (b) show the frequencies of TO and LO modes of 3C-SiC are 794 and 969 cm^{-1}, respectively, and the frequency of the TO mode of 6H-SiC is 767 cm^{-1}.

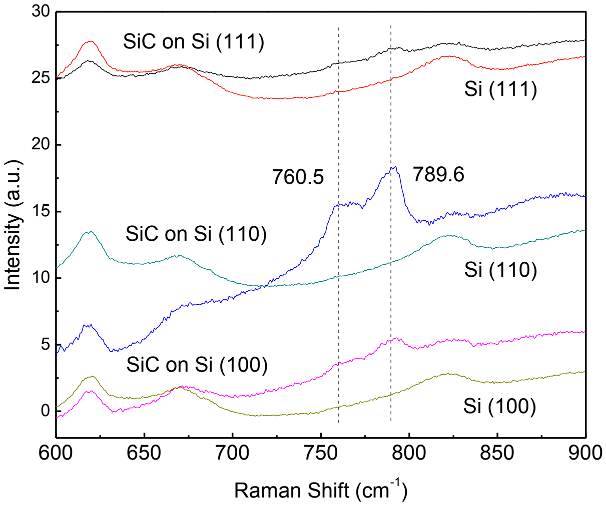
SiC on Si (111)
Si (111)
760.5
789.6
SiC on Si (110)
Si (110)
SiC on Si (100)
Si (100)
Intensity (a.u.)
Raman Shift (cm^{-1})
0
5
10
15
20
25
30
600
650
700
750
800
850
900

(a)

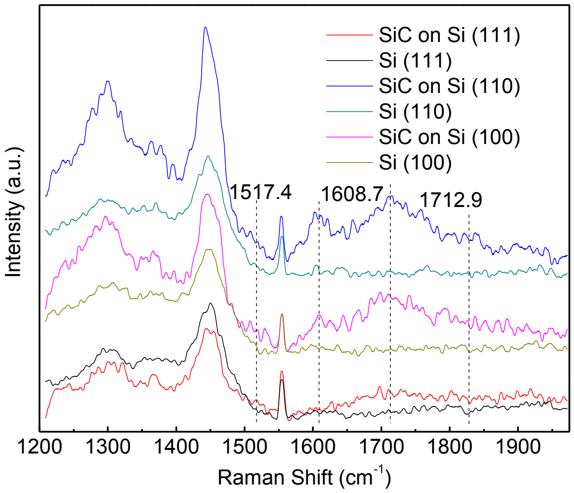
SiC on Si (111)
Si (111)
SiC on Si (110)
Si (110)
SiC on Si (100)
Si (100)
1517.4
1608.7
1712.9
Intensity (a.u.)
Raman Shift (cm^{-1})
1200
1300
1400
1500
1600
1700
1800
1900

(b)

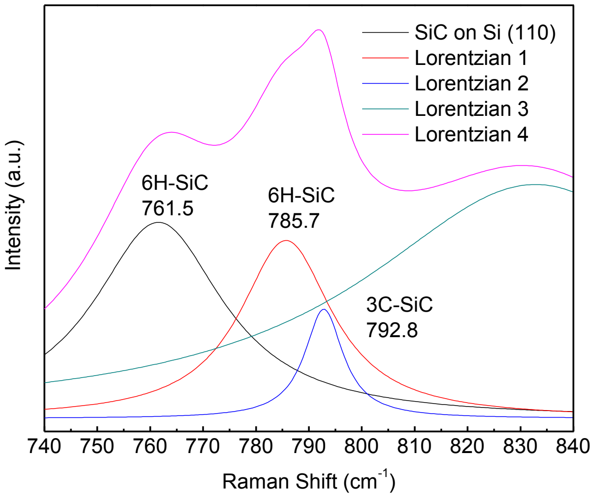

(c)

Figure 2.31: Raman spectra of SiC films grown on Si (100), (110) and (111) at T_{sub}/T_{C60}=800/550 ^{o}C for 10 min. (a) The 1st order TO. (b) The 2nd order TO. (c) Lorentzain decomposition of the 1st order TO of SiC grown on Si (110).

The TO mode of 3C-SiC actually contains two components which can be resolved by Lorentzian decomposition as shown in Figure 2.32 (d). The two components, 791 and 795 cm^{-1} are TO modes of 6H-SiC and 3C-SiC, respectively. The peak at 765 cm^{-1} is also TO mode of 6H-SiC. Figure 2.32 (c) shows that LO mode of 3C-SiC grown on Si (111) redshifts by 1.4 cm^{-1} relative to that of 3C-SiC grown on Si (110) and redshifts by 1 cm^{-1} relative to that of 3C-SiC on Si (100). This means 3C-SiC on Si (111) is subject to more biaxial tensile strain than those on Si (110) and (100) due to the larger lattice mismatch on Si (111). This is in agreement with that smaller *d*-spacing indicated by the smaller omega (ω) value of SiC on Si (111) compared to single crystal SiC, as shown in Figure 2.30 (c). The spectra in Figure 2.32 (e) show two 2nd order TO bands of 6H-SiC with the frequencies of 1517 and 1713 cm^{-1} [187]. Two broad peaks at 1359 and 1605 cm^{-1} in spectrum of SiC on Si (110) are D and G bands of decomposed C60, respectively [186].

The spectrum of C60 was also plotted in pink color in Figure 2.32 (e) as a reference to prove that C60 was already decomposed. Peaks at 1465 and 1588 cm^{-1} belong to C60. The decomposed C60 can also be observed as the particles in white color in the SEM image shown in Figure 2.26 (c). The spectra of SiC on Si (110) in the spectal range from 1300 to 1750 cm^{-1} can be resolved by Lorentzian decomposition as shown in Figure 2.32 (f). Totally, there are four subpeaks: 1359 and 1614 cm^{-1} are D and G bands of decomposed C60, and 1547 and 1711 cm^{-1} are the second order TO bands of SiC grown on Si (110). The intensity of the Raman spectrum of SiC on Si (110) is always higher than those of SiC on Si (100) and Si (111) due to the largest area atomic density of Si (110). It can also be observed from Figure 2.32 (c) that at T_{sub}/T_{C60}/time =1000 ^{o}C/550^{o}C/20 min, there are excessive decomposed C60 on SiC grown on Si (100), (110) and (111), though SiC/Si (110) has most excessive C60, indicating the growth time is too long for obtaining stoichiometric SiC.

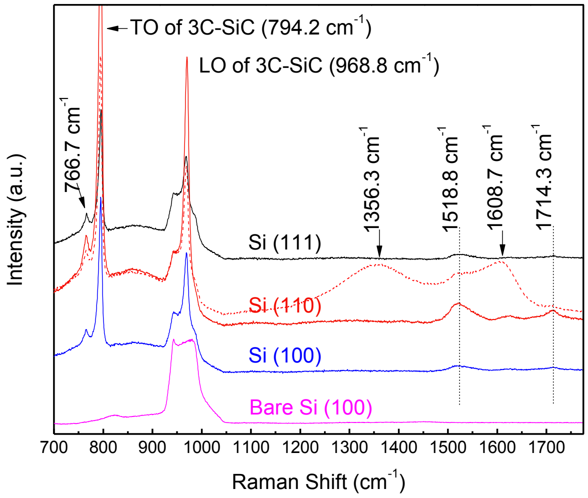

(a)

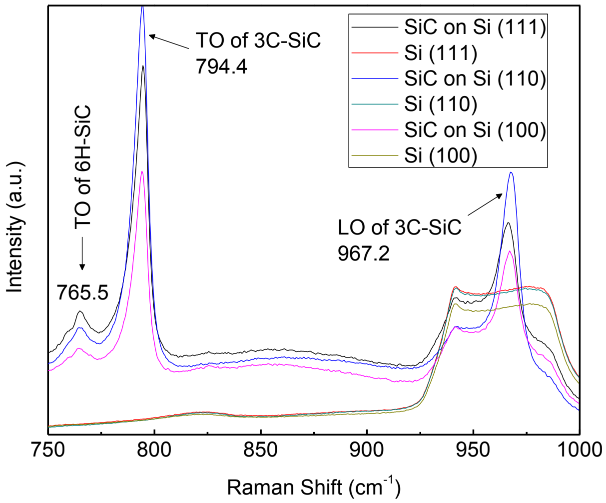
SiC on Si (111)
Si (111)
SiC on Si (110)
Si (110)
SiC on Si (100)
Si (100)
TO of 3C-SiC
794.4
TO of 6H-SiC
765.5
LO of 3C-SiC
967.2
Intensity (a.u.)
Raman Shift (cm^{-1})
750
800
850
900
950
1000

(b)

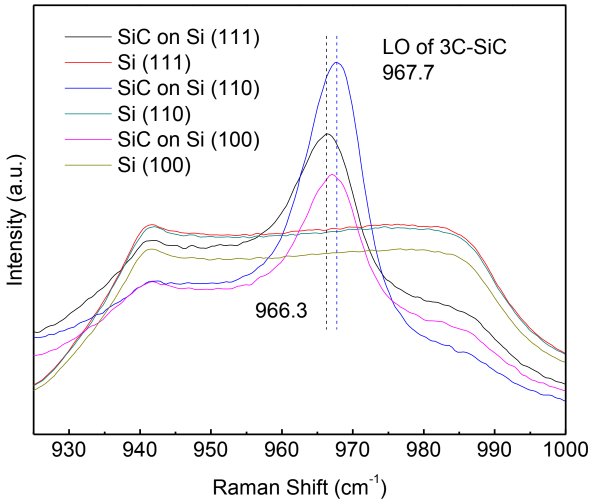
SiC on Si (111)
Si (111)
SiC on Si (110)
Si (110)
SiC on Si (100)
Si (100)
LO of 3C-SiC
967.7
966.3
Intensity (a.u.)
Raman Shift (cm^{-1})
930
940
950
960
970
980
990
1000

(c)

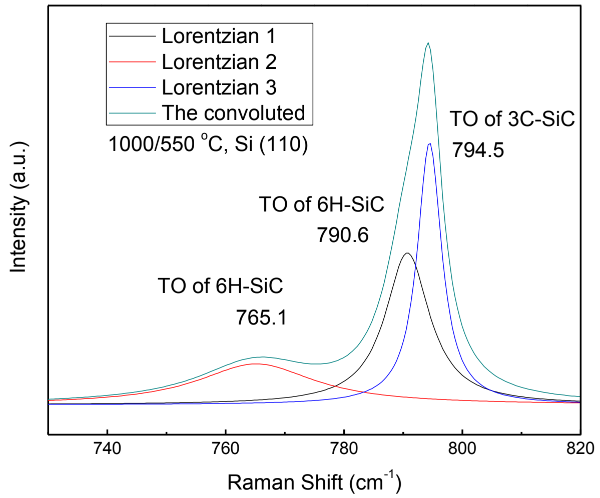
Lorentzian 1
Lorentzian 2
Lorentzian 3
The convoluted
1000/550 °C, Si (110)
TO of 3C-SiC
794.5
TO of 6H-SiC
790.6
TO of 6H-SiC
765.1
Intensity (a.u.)
740
760
780
800
820
Raman Shift (cm^{-1})

(d)

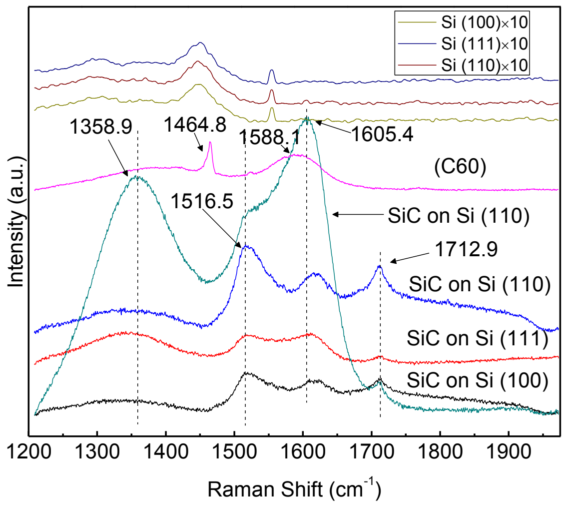
Si (100)×10
Si (111)×10
Si (110)×10
1358.9
1464.8
1588.1
1605.4
(C60)
1516.5
SiC on Si (110)
1712.9
SiC on Si (110)
SiC on Si (111)
SiC on Si (100)
Intensity (a.u.)
1200
1300
1400
1500
1600
1700
1800
1900
Raman Shift (cm^{-1})

(e)

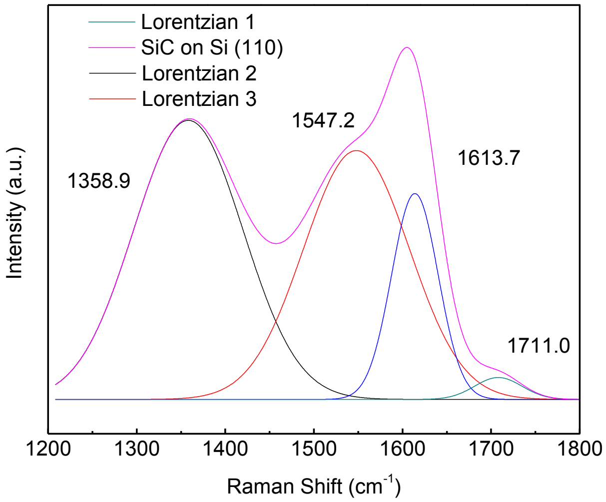

(f)

Figure 2.32: Raman spectra of SiC films grown in Si (100), (110), and (111) at T_{sub}/T_{C60}=1000/550 ^{o}C for 20 min. (a) Overall spectra. (b) The first order modes. (c) LO modes of 3C-SiC. (d) Lorentzian deconvolution of the 1st order TO modes. (e) The 2nd order TO(s) modes. (f) Lorentzain deconvolution of the 2nd order TO modes of SiC on Si (110).

2.6 TEM of SiC on Si (111)

TEM was also used to inspect the crystal structure of SiC on Si (111) grown at T_{sub}/T_{C60}=800/550 ^{o}C for 10 min. The TEM images and corresponding diffraction patterns are shown in Figures 2.33 and 2.34. In small domain, SiC is single crystal structure as shown in Figures 2.33 (a) and (b), and in large domain, SiC is polycrystal structure as shown in Figures 2.34 (a) and (b).

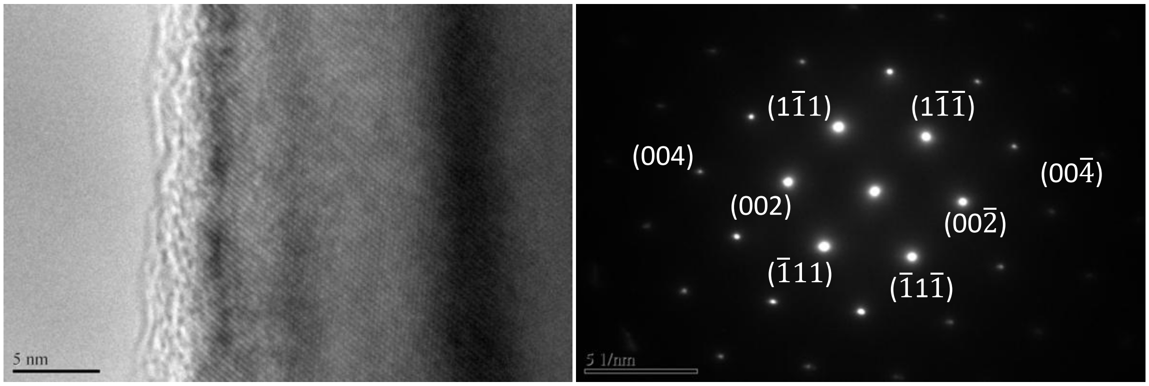

(a) (b)

Figure 2.33: TEM micrograph of SiC on Si (111) in single crystal domain. (a) TEM image. (2) Diffraction pattern of 3C-SiC. [zone axis (110)]

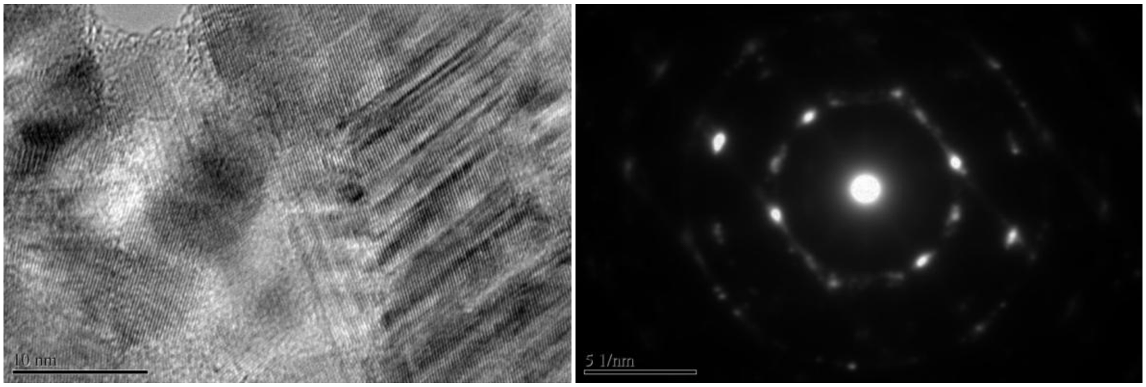

(a) (b)

Figure 2.34: TEM micrograph of SiC on Si (111) in polycrystal domain. (a) TEM image. (b) Diffraction pattern.

2.7 Summary and conclusions

The uniformity of SEM morphology and roughness of AFM topography indicate the source temperature of T_{C60} = 550 ^{o}C is preferable to T_{C60} = 450 ^{o}C because the proper C60 flux at T_{C60} = 550 ^{o}C can cover the Si substrate to form uniform SiC film. For short growth time of 5 minutes, the roughness of SiC film increases with substrate temperature, and grain size and crystallization also increase with substrate temperature, as shown in

Figure 2.35. At T_{sub}/T_{C60}/time = 800 ^{o}C /550 ^{o}C/10 min, SiC on Si (110) is smoothest among three Si palne orientations due to the highest area atomic density of Si (110).

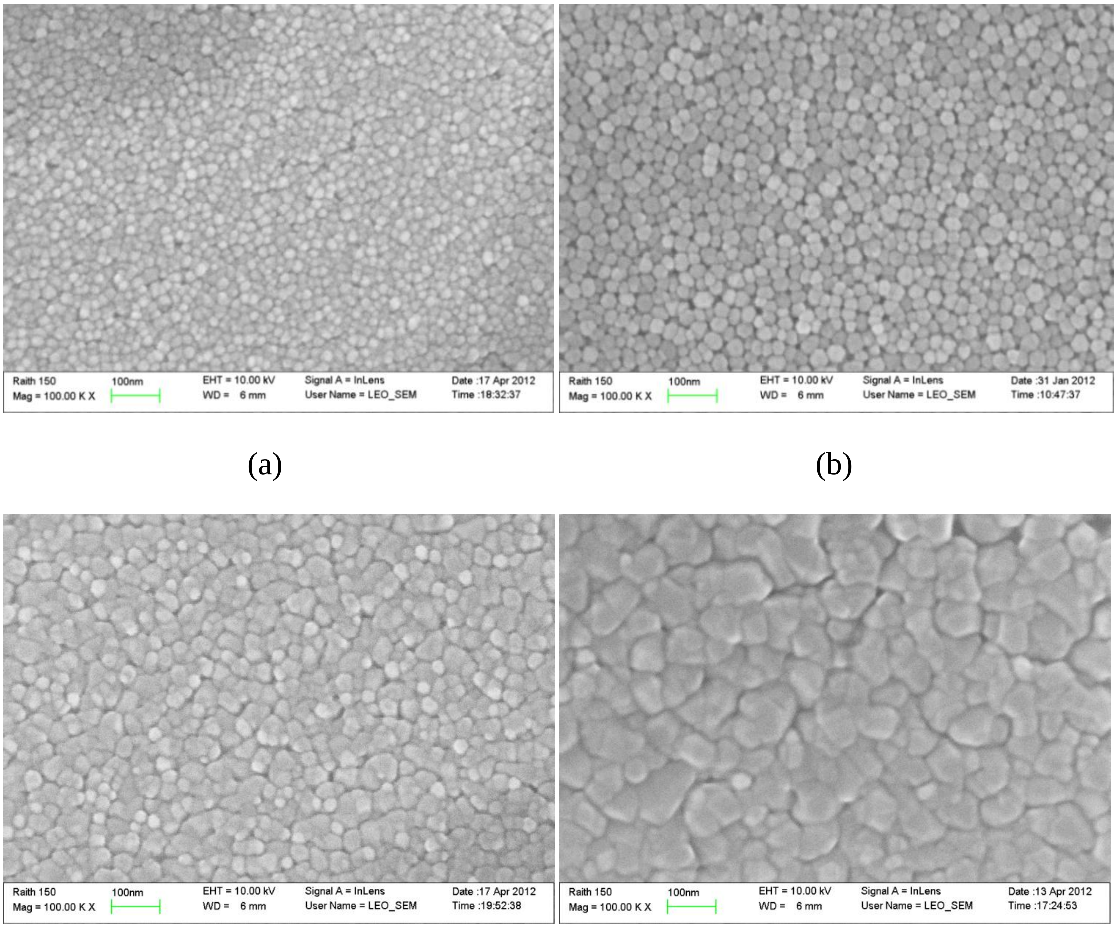

(a) (b)

(c) (d)

Figure 2.35: Morphology evolution of SiC grown on Si (111) with increasing substrate temperature. (a) 700 ^{o}C. (b) 800 ^{o}C. (c) 900 ^{o}C. (d) 1000 ^{o}C.

At T_{sub}/T_{C60}/time = 1000/550 ^{o}C/20 min, SiC on Si (111) is the smoothest because more excessive decomposed C60 (20 min.) on SiC on Si (110) resulting from the difficulty of Si in out-diffusing from Si substrate. On Si (100), SiC starts to crystallize at T_{sub}/T_{C60} = 900/550 ^{o}C, while on Si (111), SiC starts to crystallize at T_{sub}/T_{C60} = 800/450 or 700/550 ^{o}C based on XRD results (Figure 2.11). The crystallization of SiC films at different temperatures is summarized in Table 2.8.

Table 2.8: Crystallization of SiC polytype films grown on Si (100) and (111)

Growth conditions	**Raman modes (cm^{-1})**					**XRD**	**Crystallization**
	6H 1^{st} TO (767)		6H 1^{st} TO (789)		3C 1^{st} TO (796)		
700/450/ Si (100)		770.5					Amorphous 6H
700/450/ Si (111)		775.9					Amorphous 6H
800/450/ Si (100)		768.2					Amorphous 6H
800/450/ Si (111)	764.5		788.9			Yes	Crystalline 6H
900/450/ Si (100)	764.3		789.1				Crystalline 6H (low)
900/450/ Si (111)		774.1					Amorphous 6H
1000/450/ Si (100)	764.1		787.6				Crystalline 6H (low)
1000/450/ Si (111)	763.1		787.6				Crystalline 6H (low)
700/650/ Si (100)		770.4					Amorphous 6H
700/650/ Si (111)		773.3				Yes	Amorphous 6H (low)
700/550/ Si (100)	760.1		785.3				Crystalline 6H (low)
700/550/ Si (111)	762.8		787.8			Yes	Crystalline 6H
800/550/ Si (100)	765.0			790.4			6H+3C (amorphous)
800/550/ Si (111)	764.5			791		Yes	6H+3C (crystalline)
900/550/ Si (100)	765.4			791.9		Yes	6H+3C (crystalline)
900/550/ Si (111)	766.5			791.7		Yes	6H+3C (crystalline)
1000/550/ Si (100)	765.4			791	795.7	Yes	6H+3C (crystalline)
1000/550/ Si (111)	765.0		789.7		795.6	Yes	6H+3C (crystalline)

At lower T_{sub}/T_{C60} temperature combination, the SiC film is amorphous or crystalline 6H-SiC polytype, and with the increase of temperautes, 6H-SiC phase is formed increasingly and more 3C- phase are formed. On Si (111), T_{sub}/T_{C60} = 800/450 or 700/650 °C yields amorphous 6H-SiC, but T_{C60} = 550 °C yields 6H-SiC or the mixture of 6H- and 3C- SiC when T_{sub} is above 700 °C. Therefore, both kinetic energy and flux of decomposed C60 determined by the C60 source temperature contribute the formation and crystallization of

SiC polytypes, i.e., 3C- or 6H- SiC. The higher area atomic density of Si (111) might facilitate the crystallization of SiC on Si (111) at low temperatures. On both Si (100) and (111), at the C60 source temperatue of 550 ^oC and growth time of 5 minutes, FWHM of omega of SiC decreases with the substrate temperature increases from 800 to 1000 ^oC. Therefore, the lateral coherence of SiC film increases and tilt angle decreases with the increasing substrate temperature. At low substrate temperature of 800 ^oC, 3C-SiC (111) on Si (111) and (110) has narrower omega FWHM and thus better crystallization than 3C-SiC (200) on Si (100) (Figures 2.30 (a)). However, at high substrate temperature of 1000 ^oC, FWHM of omega of 3C-SiC (200)/Si (100) is close to that of 3C-SiC (111)/Si (111) and /Si (110), because the high diffusivity of Si and C at high temperature compensate the difference in area atomic density. At T_{sub}/T_{C60} = 1000/550 ^oC and for the growth time of 20 minutes, the FWHM of omega of 3C-SiC (200) is much narrower than those of 3C-SiC (111) on Si (110) and (111). The *d*-spacing of 3C-SiC (111) on Si (111) is closer to that of single crystal 3C-SiC (111) and smallerr than that of 3C-SiC (100) on Si (110). The larger d-spacing of 3C-SiC (111) on Si (110) indicates that SiC film sustains compressive strain caused by the dense SiC film and accessive decomposed C60. Different from the SiC (200) on Si (100) and SiC (111) on Si (110), the SiC (111) films on Si (111) at both T_{sub}/T_{C60} = 800/550 ^oC and T_{sub}/T_{C60} = 1000/550 ^oC are subject to biaxial tensile strain which may help itself to be decomposed into graphene layers under laser illumination as shown in Figure 3.6. TEM images and electron diffraction patterns show the SiC film is single crystal in small domain and polycrystal in large domain. At T_{sub}/T_{C60} = 800/550 ^oC for 10 min., SiC on Si (110) is the smoothest, but at T_{sub}/T_{C60} = 1000/550 ^oC for 20 min, SiC on Si (111) is the smoothest.

CHAPTER 3: LASER-INDUCED GRAPHENE

3.1 Laser annealing technique

A 532nm continuous wave (CW) Nd-YAG laser with maximum incident power of about ~30 mW was used to illuminate and then decompose 3C-SiC (111) on Si (111) into graphene layers. The 532 nm laser is an integrated part of a confocal μ-Raman system (LabRAM HR800, Horiba Jobin Yvon). The beam size of 1-2 mm can be focused down to a diffraction limit spot size of 0.7 μm on the sample surface when a 100x objective lens is used. The Raman signal is collected in backscattering geometry. The Raman mapping is carried out by moving the translational stage where the sample sits, controlled with programmable software. With the addition of an external shutter synchronized with the internal shutter within the spectrometer, the Raman map setup can also be used to control laser illumination in dot, line, or area patterns in micro scale or potential in nanoscale (if shadow masks are used to define the illumination area). Under the laser illumination, 3C-SiC film on Si (111) decomposes, i.e., the Si atoms are sublimated by the local heating, and the remaining carbon atoms reconstruct into graphene layers. The phase transformation mechanism is schematically illustrated in Figure 3.1.

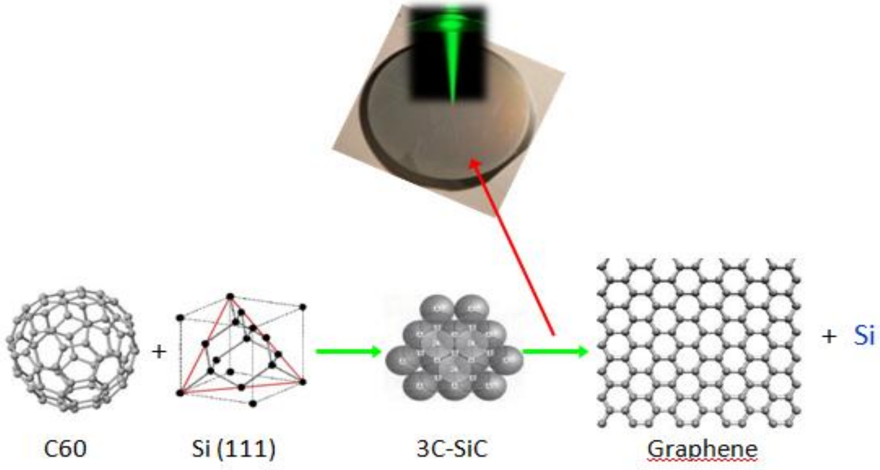

Figure 3.1: Schematic illustration of phase transition of laser-induced graphene.

In recent year, although there are a few research reports related to laser induced graphene (LIG) [119-126], they all focus on illuminating single crystal SiC with high pulsed laser power. This study concentrates on 3C-SiC film directly deposited on a Si substrate. This approach could produce graphene layers directly on Si substrate without any graphene transfer processes which may incur contamination or damage. Moreover, LIG process could locally form graphene in selected locations, desired shapes, and defined dimensions. Specially, LIG technique, with the assist of selective deposition of 3C-SiC film on Si substrate, has potential applications in patterning micro- or even nano-scale periodic graphene structures which could be integrated into Si-based nanoelectronics or graphene-Si superstructure.

In fact, electron beam, similar to photon beam, was also reported in 1982 by Iijima [185] to be able to induce graphitic sheets from 6H-SiC. He also found in the electron diffraction patterns that some narrow bands of concentric rings correspond to single or double graphitic sheets. Actually, the single or double graphitic sheets are single- or double- layer graphene. The earlier graphitization-related laser annealing work was reported by Ohkawara et al. [119] in 2003. This study demonstrated graphitization of sintered 6H-SiC (ploycrystal) using a pulsed 1064nm Nd-YAG laser and confirmed graphitization with SEM, EDS, XRD, and Raman. The Raman spectra showed D and G modes of graphite at 1360 and 1580 cm^{-1}, respectively. However, the spectral range was not long enough to include G′ (2D) peak. Probably, G′ (2D) still existed though not displayed. Since other carbon structures, such as C60, also show the D and G peaks but not G′ (2D) peak, the 2D peak is a more reliable signature for the graphite or graphene structures. Three reaction gases, argon, carbon dioxide, and air, were induced into reaction chamber during laser illumination. However, no difference in graphitization was observed for three different reaction atmospheres. Six years later in 2009, Perrone et al [120] investigated the possibility of graphene growth on 4H-SiC via laser processing. XPS and Raman results of the laser-illuminated 4H-SiC showed a broad G′ (2D) graphene signature in this study. To pursue SLG or FLG, Lee et al [121] and Yannopoulos et al. [122] have developed the laser processes to achieve SLG and FLG in 2010 and 2012, respectively. All reported laser process techniques used to induce graphene from SiC polytypes are listed in Table 2.1. Recently, , laser direct growth of graphene on Si substrate [124] and selective graphene patterning via laser-induced CVD [125].

For us, using laser to convert SiC thin-film into graphene was in fact an accidental finding. At first we measured the Raman spectra of as-grown SiC samples using the full power of the laser ~ 30 mW, using 50x lens, and the graphite or graphene signature peaks D, G, in particular 2D were observed, which initially let us to think graphene was directly grown on Si. However, when we measured the as-grown sample using a substantially

Table 3.1: Research works related to laser induced graphitization from SiC polytypes

Year **Author** **Ref.**	**SiC polytypes**	**Laser type and conditions**	**Results**
2003 **Ohkawara et al.** **[119]**	6H (sintered) Polycrystal	Pulsed 1064 nm Nd: YAG; 5 ms pulse duration; 150 J/cm^2; 1 shot; argon, carbon dioxide, and air, respectively. (peak power density 3×10^4 W/cm^2)	MLG
2009 **Perrone et al.** **[120]**	4H wafer (Cree Inc.) Single crystal	Pulsed 1064 nm Nd: YVO$_4$ (converted from CW with max.1300W/cm^2); 8 ns pulse width (min.); 15W, 5 to 40 kHz; 10 and 15W, 30 and 40 kHz; 20 and 45 μm spot size. (peak power density $1.6\sim 8\times 10^{10}$W/cm^2)	G/D ratio<1 and G′ (2D) MLG
2010 **Lee et al.** **[121]**	4H wafer Single crystal	Pulsed 248 nm KrF; 1 J/cm^2; 25 ns pulse; 20 Hz; 2mm^2 spot size; UVH<10^{-9} torr. (peak power density 4×10^7 W/cm^2)	SLG, BLG, FLG
2012 **Yue et al.** **[126]**	3C on Si Polycrystal	CW 532 nm Nd-YAG; 10~30 mW; air; 700 nm spot size. ($2.6\sim 8\times 10^6$ W/cm^2)	G/D ratio > 1, FLG, MLG
2012 **Yannopoulos et al.** **[122]**	6H Single cystal	CW 10.6 μm CO$_2$, argon gas; 3-4 mm^2 spot size; (laser power was not reported)	G/D>>1, FLG

reduced power, for instance, attenuated by a factor of 10, the graphene related peaks disappear entirely (below the detection limit which is typically below 1 cps) instead of proportionally to the power. Furthermore, if we first illuminated the as-grown sample with the full power in the meantime took the Raman spectrum, then measured by the same attenuated power again, we found that the Raman singal strength only reduced proportionally. These measurements clearly indicate the as-grown sample is not graphene but simple SiC. It is the laser illumination making the local conversion, which is also supported by the corresponding changes in the SiC related Raman features before and after illumination. The conversion can be understood as the result of local heating effect. For the single crystalline SiC sample, it has been estimated that the local temperature change under pulsed laser illumination could be as high as 1573 K using with average power of 15W with 8 ns pulse width. The peak power density used was 1.6 ~ 8 × 10^{10} W/cm^2 [120]. In our case, 10 mW can yield a power density of 2.6×10^6/cm^2. Because our SiC film is polycrystalline with rather small domain sizes, the expected low thermal conductivity could lead to higher temperature increase than in the single crystalline sample for the same laser power density. The low illumination power of polycrystalline SiC is also indicated in ref. [119], in which only 3× 10^4 W/cm^2 was used; the power density is about two orders of magnitude lower than that used in this study. The SiC in ref. [119] was polycrystalline bulk sintered from SiC powders, while the SiC in this study was polycrystalline SiC thin film on single crystal Si substrate, because Si substrate may dissipate more heat than SiC polycrystalline bulk does.

To induce graphene from 3C-SiC, the laser power of 20-30 mW focused by 100× lens integrated with Raman system was used. In Raman measurement, the incident laser power was reduced down to 1 to 2 mW to avoid any laser-heating effect. The Raman spectra of LIG and 3C-SiC without laser illumination were plotted in Figure 3.2 (a). It can be seen that after laser illumination, three strong peaks of 1348, 1583, and 2691 cm^{-1}, which correspond to D, G, and G′ (2D) bands of graphene, emerge. Also, the intensity of TO mode of 3C-SiC drops significantly. These variations in Raman peaks indicate the generation of graphene and decomposition of 3C-SiC. Since the Raman spectrum of C60 also presents D and G bands though broad, we measured as-received C60 powders and LIG using the same acquisition conditions, and plot their Raman spectra in Figure 3.2 (b). The spectrum comparison between laser-illuminated 3C-SiC and C60 shows the spectrum of the latter does not have a peak at 2690 cm^{-1} corresponding to G′ (2D) even though two broader peaks at 1350 and 1580 cm^{-1} also pop up. This means that the three sharper peaks are not from C60. These spectra comparison convincingly confirms that under the laser irradiation, 3C-SiC was decomposed and graphene layers were induced.

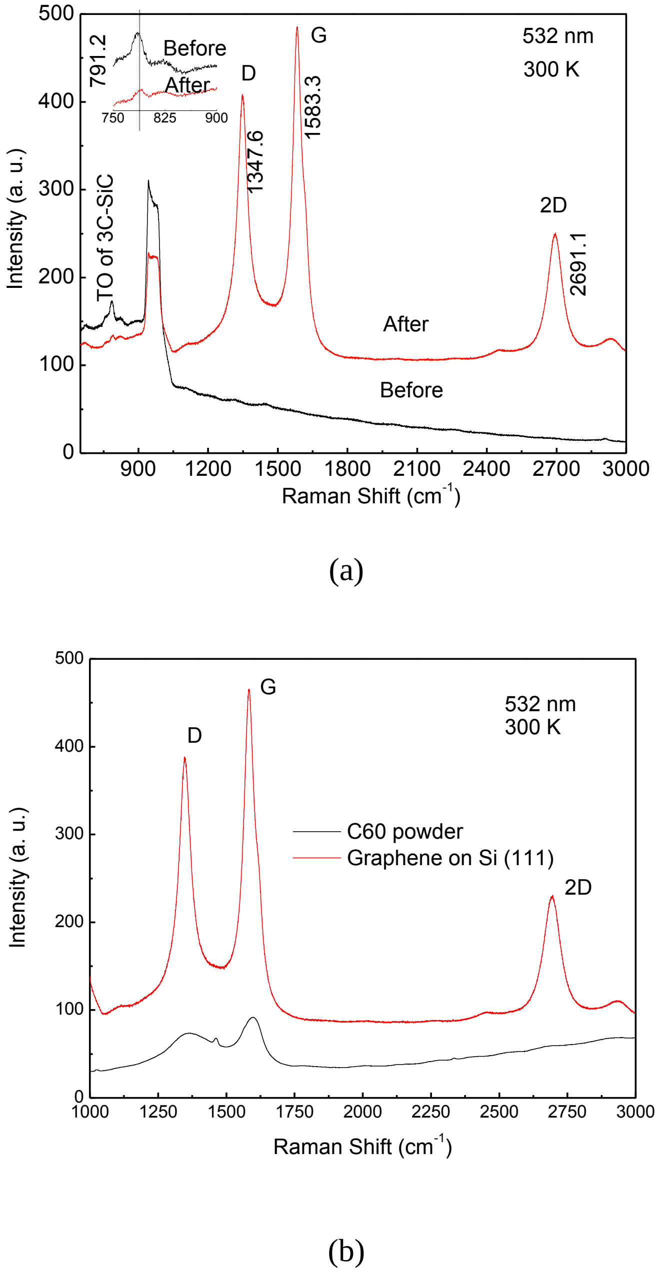

(a)

(b)

Figure 3.2: Raman spectra of laser-illuminated 3C-SiC, as-grown 3C-SiC, and as-received C60. (a) Graphene versus 3C-SiC. (b) Graphene versus C60.

This observation inspires us to develop laser annealing process into a technique for synthesizing graphene, especially for patterning small feature size graphene.

3.2 Characterization of laser-induced graphene (LIG) from 3C-SiC on Si (111)

In addition to Raman spectroscopy, TEM (JEOL2100) and AFM (Nanoscope SPM V5r30, Veeco. USA) were also used to further confirm graphene sheets. The *d*-spacing between graphene layers was measured to be about 3.70 Å from TEM image shown in Figure 3.3 (This is the separation between layers in graphite; it should be ~ 3.35 Å) . This value is larger than that of the crystalline graphite with A-B stacking (Bernal stacking, c/2 = 3.35 Å), but close to the theoretically predicted graphene layers separation of 3.61 Å (0 K) for the A-A stacking (turbostratic stacking) [189], implying that the stacking order of the multi-layer graphene is different from that in the crystalline graphite such as HOPG [190], and expecting weaker interlayer coupling. The turbostratic stacking results from extremely fast heating and cooling rates of laser which may not give graphene layers enough time to equilibrate into the energetically favorable stacking order. The number of graphene layers was found to be about 8-9 layers, falling in the range of FLG. As corroborative evidence, the tapping mode AFM image shown in Figure 3.4 revealed a flake with thickness of 3.517 nm, which is approximately the thickness of 3.517/3.7 = 9 ~ 10 layers in agreement with the result from TEM image.

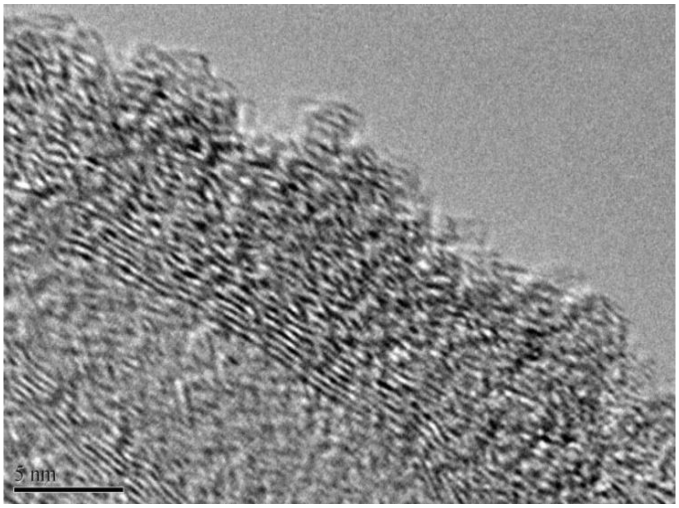

Figure 3.3: TEM image of laser-induced graphene layers on 3C-SiC (111)/Si (111)

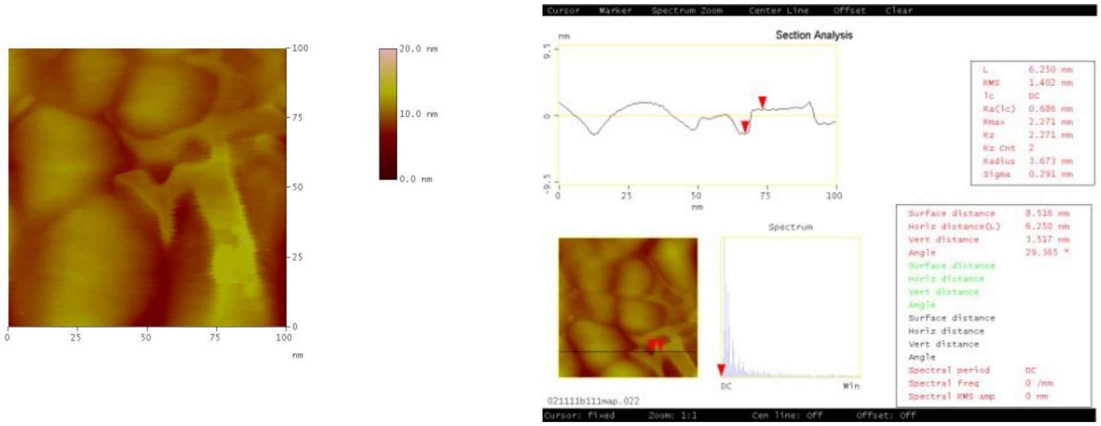

L	6.250 nm
RMS	1.402 nm
lc	DC
Ra(lc)	0.686 nm
Rmax	2.271 nm
Rz	2.271 nm
Rz Cnt	2
Radius	3.673 nm
Sigma	0.291 nm

Surface distance	8.516 nm
Horiz distance(L)	6.250 nm
Vert distance	3.517 nm
Angle	29.365 °
Surface distance	
Horiz distance	
Vert distance	
Angle	
Surface distance	
Horiz distance	
Vert distance	
Angle	
Spectral period	DC
Spectral freq	0 /nm
Spectral RMS amp	0 nm

(a) (b)

Figure 3.4: AFM results of laser-induced graphene on 3C-SiC (111)/Si(111). (a) Height image. (b) Thickness.

After the characteristic confirmation of laser-induced 3C-SiC with μ-Raman, TEM, and AFM, a 20 μm long graphene ribbon was written on 3C-SiC (111)/Si(111) and characterized with μ-Raman mapping, as shown in Figure 3.5. The Figure 3.5 (b) is Raman intensity image of G′ (2D) peak in the spectral range of 2650-2750 cm^{-1}. The comparison of Figure 3.5 (a) with Figure 3.5 (b) show that graphene layers distribute within the 20 μm long ribbon scanned with a 532nm laser focused with 100 × lens. The optical image shown in Figure 3.5 (a) displays that the line width of about 1 μm results from the laser spot size of about 0.7 μm. The comparison of Raman image shown in Figure 3.5 (b) with optical image shown in Figure 3.5 (a) indicates that the graphene layers distribute uniformly within the ribbon, which is further confirmed by the spectral comparison between illuminated and non-illuminated areas, as shown in Figure 3.5 (c). These promising results provide inspiring possibility for patterning electronic devices and electron-photon superstructures which will be explored in the following chapters.

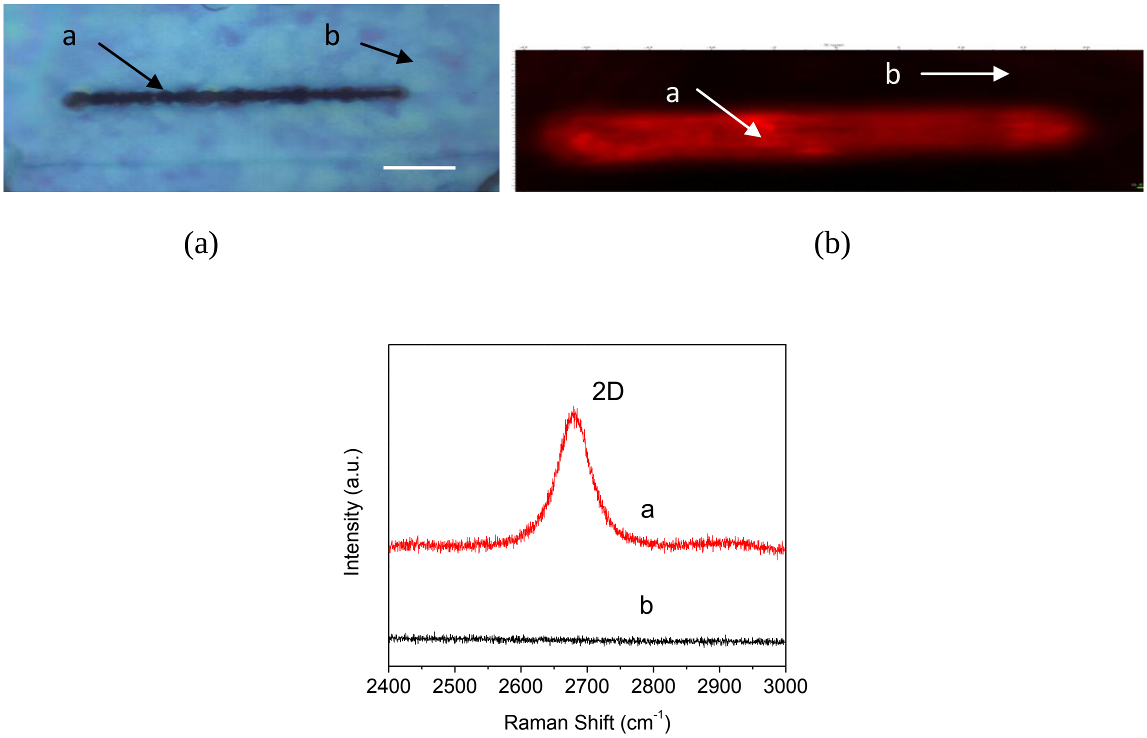

(a) (b)

(c)

Figure 3.5: Raman map results of LIG. (a) Optical image (scale bar: 5 μm). (b) Raman map image (image size: 50 ×10 μm^2; spectral range: 2650~2750 cm^{-1}). (c) Raman spectra selected from different points.

3.3 Comparison of LIG on three Si substrates (100), (110), and (111)

As discussed in Chapter 2, the crystalline structures of 3C-SiC films depend on the crystalline plane orientation of the Si substrates. Similarly, the quality of LIG also depends on the crystalline structure of 3C-SiC films. Therefore, it is necessary to compare LIGs derived from three different Si substrates (100), (110) and (111). Laser irradiation on three types of 3C-SiC thin films grown on three Si substrates (100), (110) and (111) were performed with same illumination conditions and the LIG graphene layers were characterized using μ-Raman with same acquisition conditions. Raman spectra are plotted and shown in Figure 3.6.

In order to find out the variations before and after laser illumination to identify the features resulting from laser illumination, two spectra at each test point before and after illumination were collected. Also, the spectrum of bare Si (100) was collected as a reference to identify the weak peaks from thin 3C-SiC. When comparing the spectra, since multi-spectral windows have to be used to cover a large spectral range including phonon modes of silicon, 3C-SiC, and LIG graphene, TO of standard Si (100) wafer was used as a reference to calibrate the relative spectral shift of each spectrum caused by the potential mechanical errors due to moving grating. All spectra are shown in Figure 3.6. It can be seen that graphene layers can be induced from all 3C-SiC grown on three different Si substrates (100), (110) and (111). However, 3C-SiC (111)/Si (111) shows much stronger G′ (2D) band and much lower D to G ratio than those of 3C-SiC(100)/Si(100) and 3C-SiC (111)/Si(110), and 3C-SiC (200)/Si (100) has weakest G′ (2D) band and largest D to G ratio. This means that it is easier for graphene layer to be laser-induced from 3C-SiC (111)/Si (111) than from 3C-SiC (200)/Si (100) and 3C-SiC (111)/Si (110), and Si (111) is the most suitable substrate for growing 3C-SiC (111) for graphene conversion. The decomposition of 3C-SiC can also be confirmed by the drop in intensity of TO mode at 793 cm^{-1} of 3C-SiC. It can be seen that the intensity of TO of 3C-SiC(111)/Si(111) drops significantly after laser illuminated, while the other two drop only slightly. As analyzed in chapter 2, 3C-SiC on Si (111) substains tensile strain, while 3C-SiC on Si (100) and Si (110) sustain compressive strain. This is one reason that it is easier to decompose 3C-SiC on Si (111) than those on Si (100) and (110) and more obvious graphene Raman signature was observed on Si (111) after laser illumination. Moreover, the G bands of graphene layers on 3C/SiC(100)/Si(100) and 3C-SiC (111)/Si(110) blue-shift with respect to that of 3C-SiC(111)/Si(111), which means that graphene layers on the former two might undergo compressible strain/stress due to the larger lattice mismatch between graphene and underlying 3C-SiC.

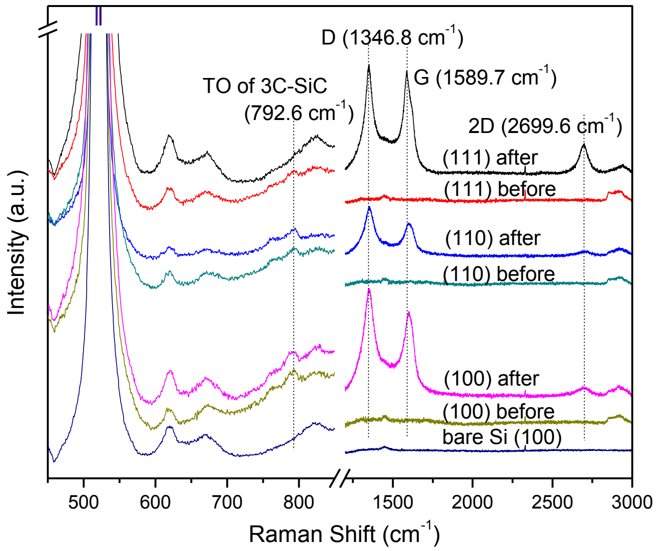

Figure 3.6: Raman spectra of laser-induced graphene on 3C-SiC grown on Si (100), (110) and (111).

3.4 Phonon modes of graphene and laser energy dependence

Since both D and G′ (2D) bands of graphene layers are double resonant phonon modes and thus laser-energy dispersive [191], the Raman spectrum of laser-induced graphene on 3C-SiC(111)/Si(111) was measured with three excitation lasers with three different wavelengths of 442, 532, and 633 nm, respectively, as shown in Figure 3.7. It can be seen from Figure 3.7 (a) that both D and G′ (2D) blue-shift along with the increasing excitation laser energy, but the increase rate of the G′ (2D) band is almost double that of the D band. The linear extrapolation of the plot of D and G′ (2D) band wavelength versus laser energy shown in Figure 3.7 (b) shows $\Delta\omega_D/\Delta E_{laser} = 49.1\ cm^{-1}/eV$, and $\Delta\omega_{2D}/\Delta E_{laser} = 103.4\ cm^{-1}/eV$, which is close to $\Delta\omega_D/\Delta E_{laser}{\sim}50\ cm^{-1}/eV$ and $\Delta\omega_{2D}/\Delta E_{laser}{\sim}100\ cm^{-1}/eV$ [191]. Another observation is the intensity ratio of (D/G) decreases with increasing laser energy. This is because the laser spot size decreases with the decrease in wavelength (i.e., increase in laser energy), and the defects or disorders concentrate mostly on the edge of the illuminated area. Larger laser spot size collects more signal from edge, while smaller spot size collects less signal from edge. However, the signal of G mode changes slightly with the spot size. Therefore, the D/G ratio of LIG increases with decreasing wavelength and increasing laser energy.

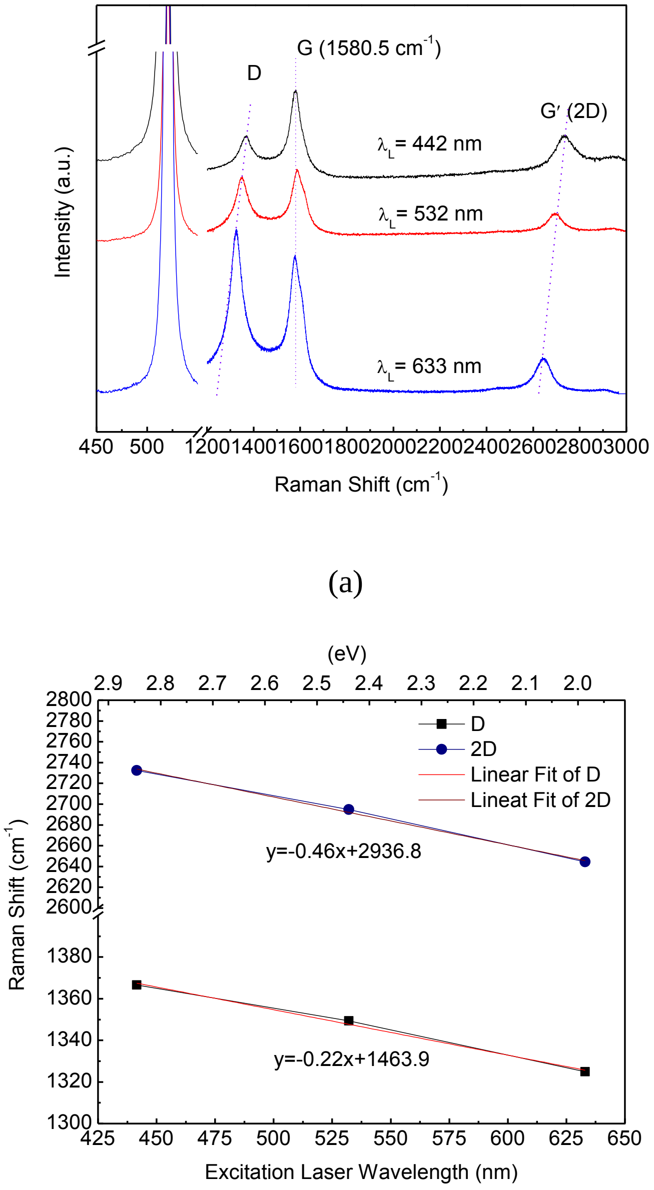

(a)

(b)

Figure 3.7: Laser energy dependence of Raman spectra of laser-induced graphene on 3C-SiC (111)/Si(111). (a) Raman spectra. (b) Linear dispersion of D and G′ (2D) band.

The excitation energy dependence of D and G′ (2D) bands of graphene can be explained by the resonance Raman processes illustrated in Figure 3.8. For example, the D band is inter-valley double resonant (DR), and Raman scattering is a fourth order process as shown in Figure 3.8 (d) : (1) a laser induces excitation of an electron-hole pair; (2) electron (or hole) - phonon inelastic scattering with an exchanged momentum $q \sim$ K; (3) elastic scattering of the electron (or hole) by a defect; and (4) the recombination of the excited electron and hole. The second and third steps can be exchanged.

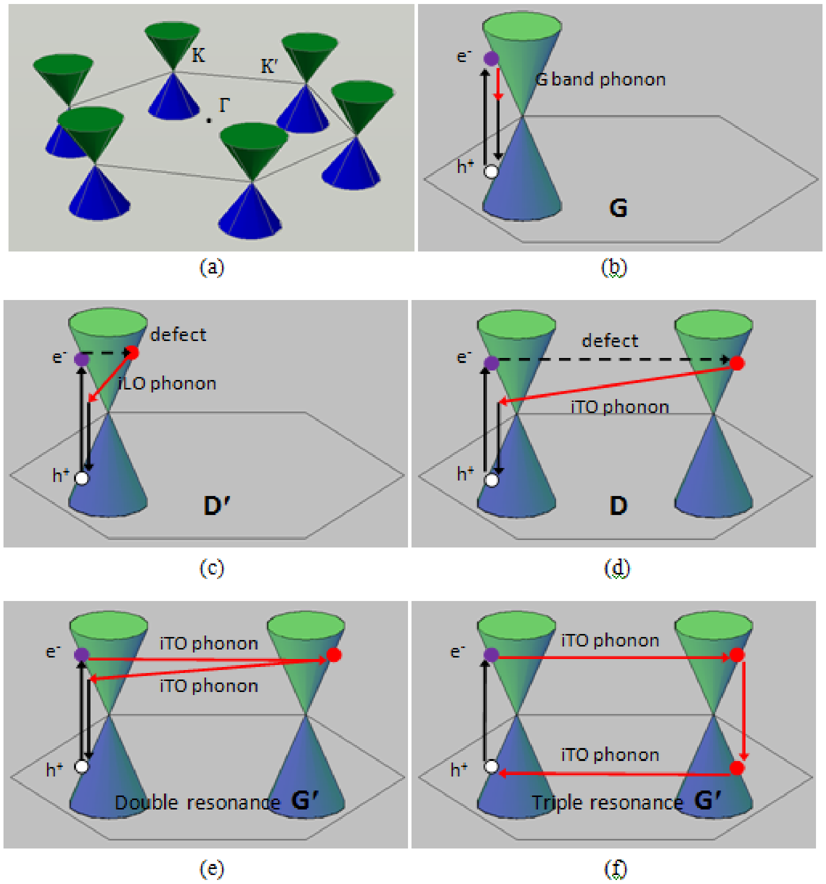

(a) (b) (c) (d) (e) (f)

Figure 3.8: Schematic illustration of resonant phonon modes of graphene.

3.5 Raman spectra comparison of LIG, natural graphite, and graphene on other substrates

In order to compare quality of laser-induced graphene on 3C-SiC(111)/Si(111) with natural graphite or monolayer graphene on other substrates, we collected different samples listed in Table 3.2 and illustrated in Figure 3.9. Among these samples, only LIG and graphene on Ni/sapphire were synthesized by us. The graphene on Ni/sapphire was grown by evaporating C60 on Ni/sapphire substrate at about 700 ^{o}C. The carbon atoms were decomposed from C60 and then dissolved into Ni. During cooling down process, carbon atoms segregate from Ni and reconstruct into graphene layers. The the number of graphene layer depends on the growth temperature and cooling rate.

First, Raman spectra were collected from all available graphene samples and overlayed together with that of LIG as shown in Figures 3.10 and 3.11. It can be seen that D mode of laser induced graphene is much higher than those of natural graphite and monolayer graphene on different substrates. However, since the LIG graphene layers were induced by a laser spot size of about 0.7 μm and measured with the same laser spot size, the defects or disorders which most likely concentrated on the edges are also collected as Raman signal, contributing to the intensity of defective D mode. The 2D peak shape of LIG is symmetrical and close to that of single layer graphene de-convoluted from natural graphite, indicating stacking order of laser-induced graphene is turbostratic or A-A stack instead of Bernal or A-B stack.

Table 3.2: List of LIG, graphite, and monolayer graphene on different substrates

S/N	Name	Description
1	Asbury graphite	Natural graphite, bulk
2	Graphene on Ni	MLG grown on Ni/sapphire substrate by us
3	Graphene on SiO_2/Si	SLG graphene (CVD) transferred on SiO_2
4	Graphene on SS	SLG graphene (CVD) transferred on stainless steel
5	Graphene on quartz	SLG graphene (CVD) transferred on quartz
6	LIG	Laser induced graphene from 3C-SiC on Si (111)

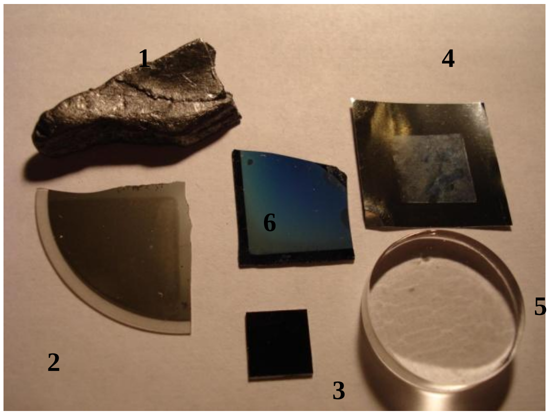

Figure 3.9: Optical images of LIG, graphite and graphene samples

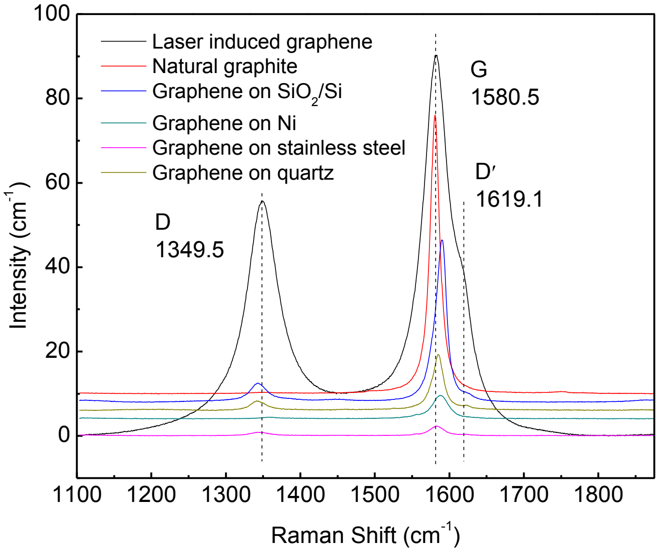

(a)

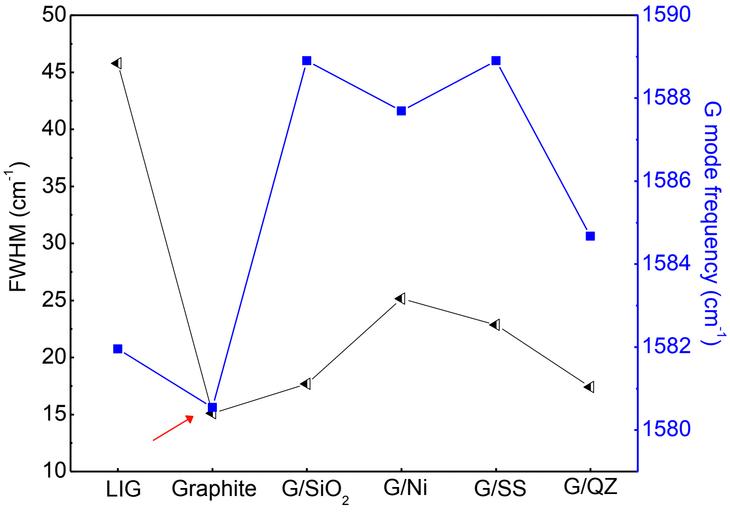

(b)

Figure 3.10: D and G bands spectra of LIG and monolayer graphenes on other substrates. (a) Raman spectra. (b) FWHM and G mode frequency.

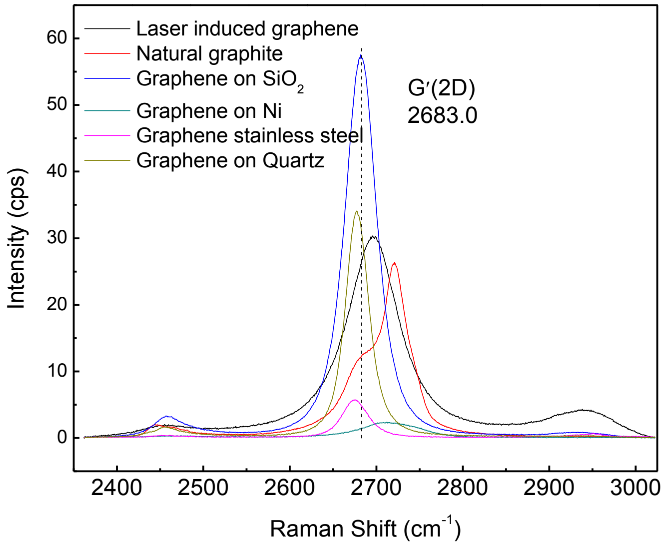

(a)

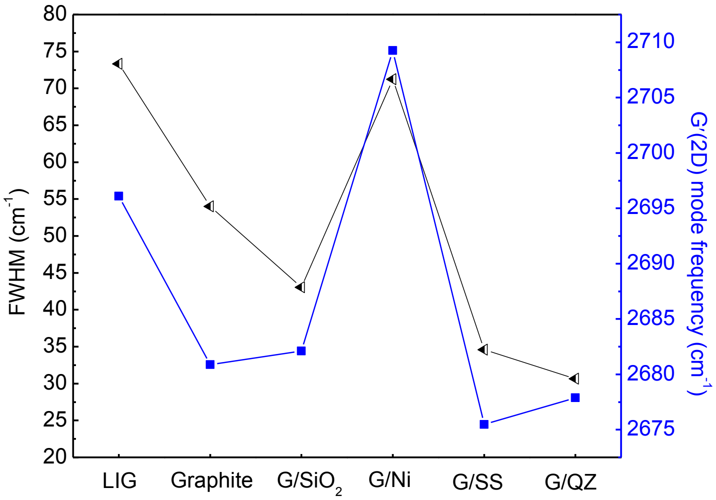

(b)

Figure 3.11: G′ (2D) band spectra of LIG and monolayer graphenes on other substrates. (a) Spectrum. (b) FWHM and G′ (2D) mode frequency.

From Figure 3.10 (b), it can be seen that G bands (in blue color) of all SLG or MLG on Ni upshift/blueshift by 2 to 8 wavenumbers with respect to that of natural graphite. This means monolayer graphene transferred onto alien substrates are either subjected to compressive strain or are doped with charge carriers (electrons or holes) [192]. This may be due to the lattice mismatch or chemical doping caused by charge transfer, and both electron and hole transfers cause blueshifting of G band [192]. Compared with SLG transferred on SiO_2/Si, stainless steel, and quartz, as well as MLG grown on Ni, the G band of LIG graphene layers blueshifts less, i.e., one wavenumber, implying LIG graphene layers sustain less compressive strain or less chemical doping. Although G band frequency of LIG is closer to that of graphite, FWHM is much larger and about 3 times that of graphite, because LIG is polycrystalline or an ensemble of small graphene domains, associated with the polycrystalline structure of the SiC film. The doublelet structure of the 2D peak is a good indication of *c*-axis ordering and thus turbostraticity [193]. In particular, it was reported that turbostratic graphene, i.e., with A-A stacking, has a single 2D peak and FWHM of ~ 72 cm^{-1}, which is double that of the 2D peak of graphene (~30 cm^{-1}) and is upshifted by 20 cm^{-1} [193]. This report is in agreement with the results observed in Figures 3.11 (a) and (b): the FWHM of 2D peak of LIG is ~ 74 cm^{-1}, larger than that of graphene on quartz (~ 30 cm^{-}1) by ~ 20 cm^{-1}. Therefore, the FWHM of 2D peak of LIG shows the *c*-axis stacking of LIG is turbostratic ordering (A-A stacking) instead A-B stacking, which is consistent with the layer separation from the TEM image shown in Figure 3.3. With respect to the G′/2D band of natural graphite, that of LIG graphene layers blueshifts by ~ 16 cm^{-1}, implying doping by hole [192]; that of SLG on SiO_2 blueshifts by ~ 2 cm^{-1}, implying doping by holes; that of MLG on Ni blueshifts by ~ 34 cm^{-1}, implying doping by holes; however, those of SLG on stainless steel and quartz redshift by 5 and 2 cm^{-1}, implying doping by electron, respectively. In terms of small peak shift and narrow FWHM, quartz substrate stands out as the best substrate candidate to support single layer graphene. In Figure 3.10 (a), there is obviously a shoulder peak of 1619.1 cm^{-1} on the right-handed side of G peak of the LIG spectrum. The shoulder peak is designated as D′ which is also a defect or disorder induced peak, but it is an intra-valley single resonant mode as shown in Figure 3.8 (c). D′ peak can be resolved by using Lorentzian decomposition as shown in Figure 3.12. The G′ (2D) peak of natural graphite is actually composed of two components which can be resolved and shown in Figure 3.13 (a), and G′ (2D) of LIG contains only one symmetric but broader as shown in Figure 3.13 (b). For graphene layers grown on Ni/sapphire should be MLG because Lorentzian decomposition of asymmetric G′ (2D) peak shows that the G′ (2D) peak can be resolved into two subpeaks, as shown in Figure 3.14.

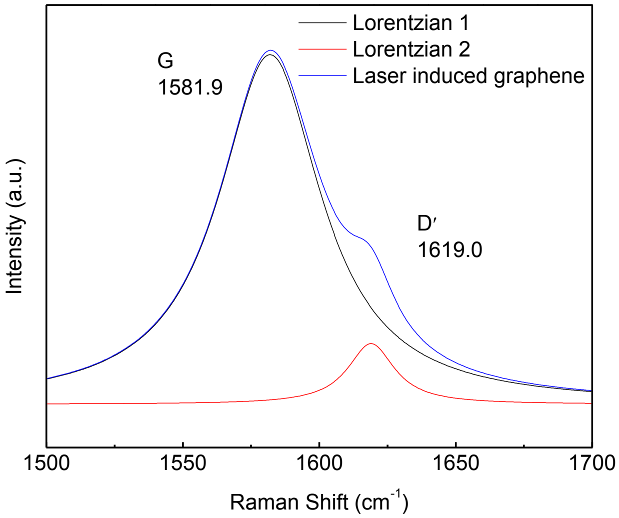

Figure 3.12: Lorentzian decomposition of the convoluted G peak.

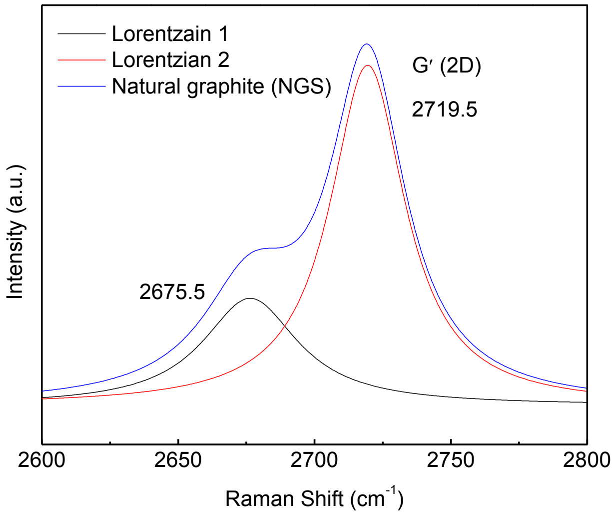

(a)

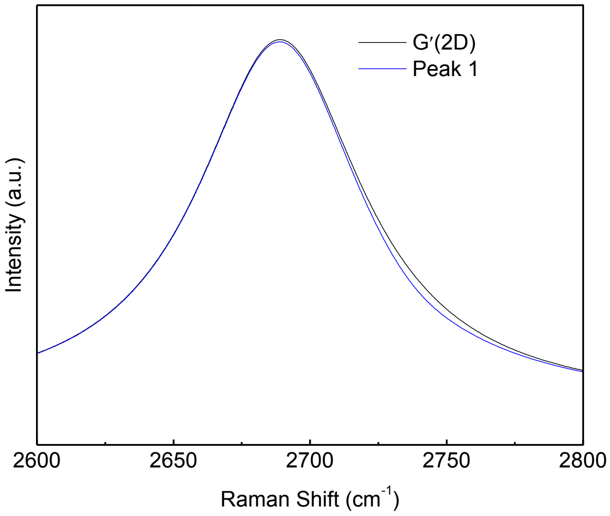

(b)

Figure 3.13: Lorentzain decomposition of G′ (2D) peak of (a) Natural graphite. (b) LIG.

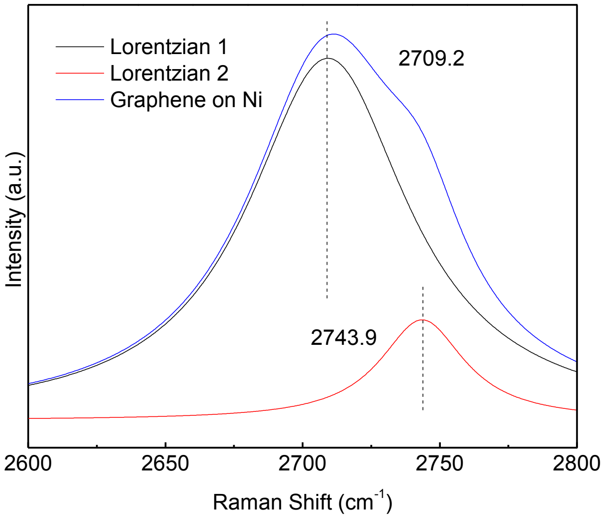

Figure 3.14: Lorentzain decomposition of G′ (2D) peak of MLG on Ni/sapphire.

Besides three major phonon modes of graphene, there are a few higher order modes. Therefore, the extended spectral range was selected to include these modes. Figure 3.15 shows three Raman spectra of LIG, natural graphite and monolayer graphene on SiO_2/Si in the spectral range from 1000 to 4500 cm^{-1}. In addition to D, D′, G, and G′ (2D), there are four (4) more peaks: 2450, 2928, 3247, and 4306, which are designated to (T+G), (D+G), 2D′, and (G′+G), respectively.

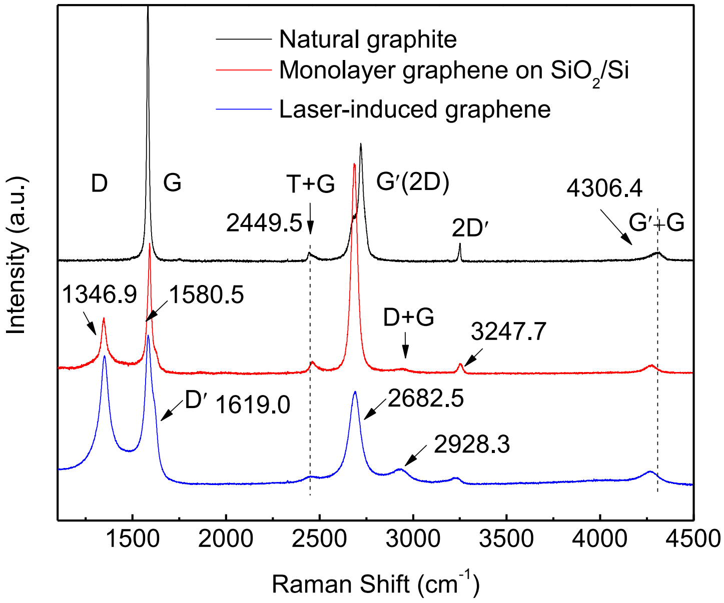

Figure 3.15: Raman spectra of LIG, natural graphite and monolayer graphene on SiO_2/Si in extended range.

3.6 Summary and conclusions

Laser induced graphene was demonstrated and proved to be an effective graphene synthesis technique. LIG graphene layers in turbostratic (AA) stacking order have larger interlayer *d*-spacing than that of natural graphite in Bernal (AB) stacking order. The graphene micro-ribbon was produced by LIG technique and characterized with Raman mapping. LIG graphene layers derived from 3C-SiC on Si (111) have the best quality graphene among Si (100), (110) and (111) due to the larger tensile strain in 3C-SiC on Si (111). Compared with monolayer graphene transferred onto other substrates such as SiO_2/Si, stainless steel, or quartz, LIG graphene layers are subjected to less compressive strain/stress or less chemical doping than SLG on other substrates [192]. The charge doping of LIG on SiC/Si (111) is probably hole doping if any [192]. The relatively strong 2D mode and large FWHM indicate LIG graphene are composed of non-uniform nanoscale graphene domains (maybe due to the fact that the SiC is polycrystalline) formed in non-equilirium conditions resulting from extremely rapid heating and cooling rates. The graphene layers grown on Ni/sapphire should be MLG, and both G and G′ (2D) are blueshifted due to the compressive stain/stress or doping charge transfer from the substrate. The phonon energy of D and G′ (2D) bands of LIG depends on the laser excitation energy; the D and G′ (2D) bands are blue-shifted with the increasing laser energy at the rate of about ~ $49.1\ cm^{-1}/eV$ and $103.4\ cm^{-1}/eV$, respectively. Also, the D/G ratio of LIG decreases with the increasing laser energy. This is because the laser spot size decreases with the decrease in wavelength (i.e., increase in laser energy), and the defects or disorders concentrate mostly on the edge of the illuminated area. Larger laser spot size collects more signal from the edge, while smaller spot size collects less signal from the edge. However, the signal of G mode changes slightly with the spot size. Therefore, the D/G ratio of LIG increases with decreasing wavelength and increasing laser energy. The higher order Raman bands of LIG were measured in an extended spectra range with the comparison with those of natural graphite and SLG on SiO_2/Si. Four more bands were observed: (T+G) (2450 cm^{-1}), (D+G) (2928 cm^{-1}), 2D′ (3248 cm^{-1}), and (G′+G) (4306cm^{-1}).

CHAPTER 4: SELECTIVE DEPOSITION OF 3C-SiC ON Si WAFER

4.1 Three approaches to farbicate graphene micro- and nano-structures using laser

Laser conversion technique has been proven to be an effective way to induce graphene layers from 3C-SiC grown on Si (111) with μ-Raman, AFM, and TEM in Chapter 3. Unlike other typical synthesis methods such as CVD on metal and thermal decomposition of single crystal SiC bulk which are more suitable for producing large area graphene, laser conversion technique, is more applicable and effective for patterning graphene nanostructures used in nanoelectronics or electron-photon superstructure. Three approaches are proposed to pattern graphene micro- or nano- structures based on laser illumination technique: (1) direct writing (DW), (2) illumination mask (IM), and (3) Pre-pattern (PP), as schematically illustrated in Figure 4.1.

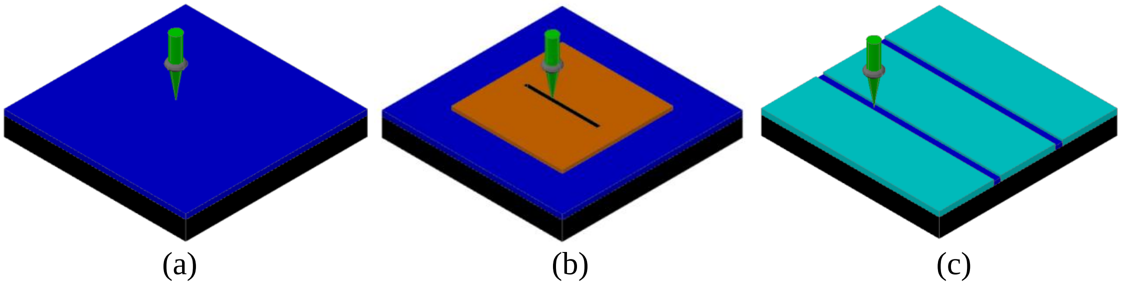

Figurre 4.1: Three approaches to pattern graphene micro- or nano-structure using laser annealing technique. (a) Direct writing. (b) Illumination mask. (c) Pre-patterning. (black-Si, blue-SiC, brown-illumination mask, light blue-SiO_2, and green-laser).

Each approach has its pros and cons. The first method-DW is the simplest but the minimum feature size is limited by the smallest achievable laser spot size, i.e. diffraction limit feature size. The second one-IM can reduce the feature size by using an illumination mask with the aperture size below the diffraction limit. The third one-PP, though more complicated, is capable of patterning nanoscale size graphene by selectively depositing nanoscale 3C-SiC using e-beam lithography and MBE. This approach is based on the fact SiC can be selectively grown on exposed Si area but not on the area covered by SiO_2 [195]. Both the 2nd and 3rd methods can in principle overcome the diffraction limit and yield nanoscale size graphene structures. The capability of patterning graphene nanostructure is probably a major advantage of this study over other reported SiC-related laser-induced graphene.

4.2 Selective deposition of SiC film on Si substrates

The feasibility evaluation started with photolithography process. A photomask consisting of 5 μm line/5 μm spacing was employed to pattern 5 μm SiO_2/5 μm Si by depositing SiO_2 with plasma enhanced chemical vapor deposition (PECVD) and etching SiO_2 with reactive ion etching (RIE) , as shown in Figure 4.2. A bare Si (111) wafer was cleaned with standard cleaning processes as depicted in Table 2.1. A SiO_2 layer of 120 nm in thickness was deposited on the cleaned Si wafer with PECVD. Amorphous SiO_2 can be conformally coated by the decomposition of tetraethyl orthosilicate (TEOS) or the reaction between silane (SiH_4) or laughing gas (N_2O). Positive tone photoresist Shipley 1813 was spin-coated on the SiO_2-coated Si wafer. The photoresist-coated SiO_2/Si wafer was soft-baked at 90 ^{o}C for 1 min, and then underwent UV exposure and developing of exposed photoresist, followed by hard baking at 105 ^{o}C for 10 minutes. Subsequently, the sample was transferred to RIE chamber for dry-etching the exposed SiO_2 with 30 milli-torr CF_4 plasma induced by 150 W forward RF power. After RIE etching, the sample was cleaned with acetone and methanol for 5 minutes each, blown dry with nitrogen gas, and then loaded into MBE chamber for selective deposition of SiC on exposed Si. A 30×50 μm^2 rectangular area was selected for laser illumination. The laser illumination was performed in the step size of 0.3 μm. Meanwhile, the Raman signal was collected at each illuminated point. The optical and Raman G′ (2D) images are shown in Fig. 4.3. It is apparent that Raman intensity/color image is correlated to the optical image of the laser-illuminated area, meaning only the selectively deposited 3C-SiC was converted into graphene layers by laser illumination. These preliminary results prove the feasibility of selective deposition of 3C-SiC on Si (111) and the conversion from patterned 3C-SiC to graphene by laser illumination to achieve the patterned feature size.

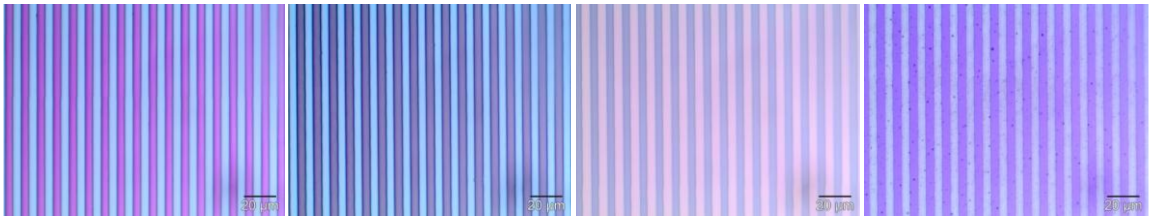

(a) (b) (c) (d)

Fig. 4.2. Process flow for selectively depositing 3C-SiC on patterned Si (111). (a) After the developing of photoresist. (2) After RIE. (3) After stripping of photoresisit. (4) After MBE growth.

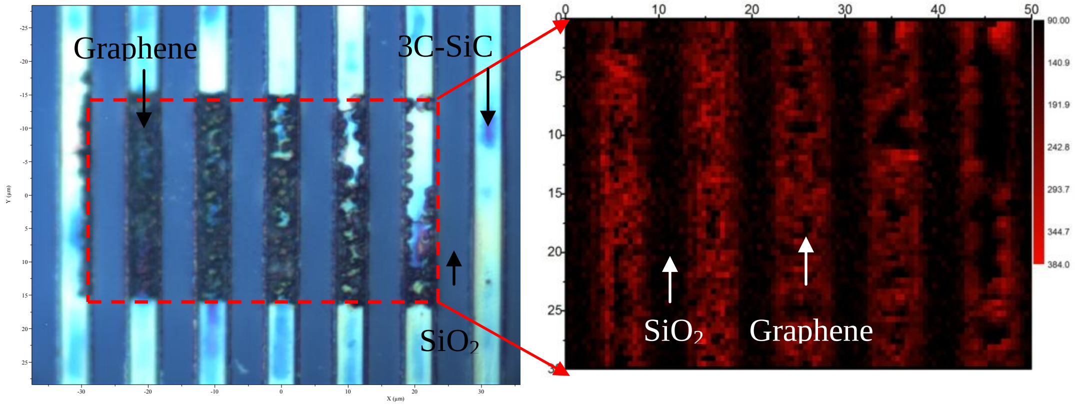

(a) (b)

Figure 4.3: Optical and Raman images of selective deposited 3C-SiC/Si (111) (5μm SiC/5μm SiO$_2$). (a) Optical image. (2) Raman map image (2650-2750 cm^{-1}).

Following the successful demonstration of selective deposition of 3C-SiC and then selective laser-induced graphene over the selective deposited 3C-SiC, e-beam lithography instead of photolithography was employed to pattern smaller feature size Si for subsequent selective deposition of 3C-SiC. The detailed process flow is schematically illustrated in Figure 4.4. With e-beam lithography, sub-100 μm feature size of selectively deposited SiC (e.g., SiC nanoribbon or nanodot) could be achieved. The nanoscale feaure size also presents challenges for the process control in RIE process and MBE growth.

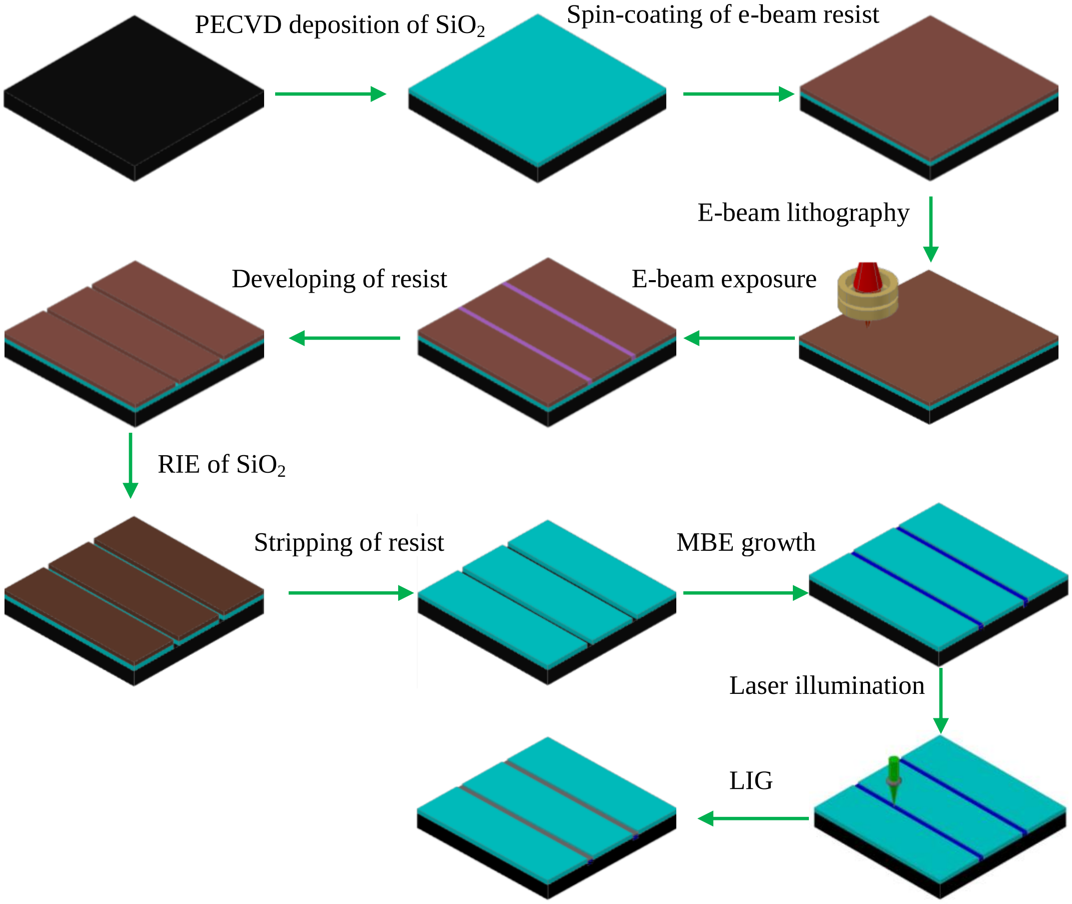

Figure 4.4: Schematic illustration of process flow chart for selective deposition of SiC on Si (111).

4.3 Process control, results and characterization

Similar to the photolithography processes used in the preliminary evaluation shown in Figure 4.2, positive tone e-beam resist, ZEP 520A-7 was spin-coated on 120 nm thick SiO_2 at the rotation speed of 5,000 rpm for 60 seconds. The spin-coated SiO_2/Si was pre-baked at 180 ^oC on a resistively heated hotplate for 3 minutes. Raith 150 was used to write a pattern designed with GDS II software. The beam current, area dose, and line dose are 27.59 pA, 30 μAs/cm^2 and 100 pAs/cm, respectively. The exposed e-beam resist was developed in pentyl acetate solution and then rinsed in methyl isobutyl ketone (MIBK) for 60 seconds each, followed by further cleaning with DI water and blowing dry with nitrogen gas. Before being loaded into the chamber for dry etching, the patterned sample was post-baked at 105 ^oC for 5 minutes to improve the adhesion of resist to the substrate.

The evaluation of the exposable linewidth and electron dose was carried out with the design of lines in different width and spacing shown in Figure 4.6 (a). It was found the line of 100 nm linewidth could be exposed with the minimum area and line doses of 25 μAs/cm^2 and 80 pAs/cm, respectively. The minimum exposable linewidth is 79 nm shown in Figure 4.5 (b). After the pattern was written on ZEP 520A-7, the sample was loaded into the RIE chamber for dry-etching. The inductively coupled reactive ion etcher (ICP-RIE) (SPTS, Inc., UK) was employed to etch SiO_2 with the introduction of gas mixture of CF_4: Ar: H_2 = 70:25:5 for 4 minutes. Following RIE etching, the resist residue left on the pattern was stripped by soaking the sample in NMP solution heated up to 40 ^oC with the assist of unltrasonification for 10 minutes. Then, the sample was cleaned with acetone and methanol solution with the assist of ultrasonification for 5 minutes each and blown dry with nitrogen gas.

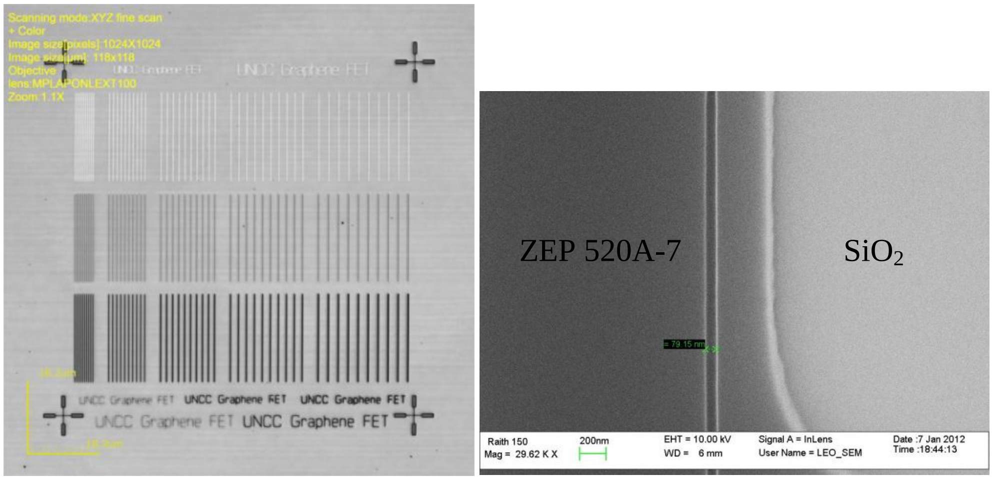

(a) (b)

Figure 4.5: Optical and SEM images of e-beam exposed lines (after developing). (a) (Optical) Exposed lines with different widths. (b) (SEM) 79 nm wide exposed line.

After RIE etching and post-cleaning, the Si substrate was loaded into MBE growth chamber for selectively depositing 3C-SiC on the exposed Si (111) using the processes described in Chapter 2. The substrate temperature, source temperature, and growing time are 800 ^{o}C, 550 ^{o}C, and 8 minutes, respectively. Figure 4.6 shows 20 μm long 3C-SiC ribbons in the spacings of 0.5 and 1 μm. The minimum linewidth of 3C-SiC ribbon is 108 nm. Through further optimization of the process variables such as electron acceleration voltage, electron does and etching parameters, linewiths of 97 and 89 nm were achieved and shown in Figure 4.7 (a) and (b) , respectively.

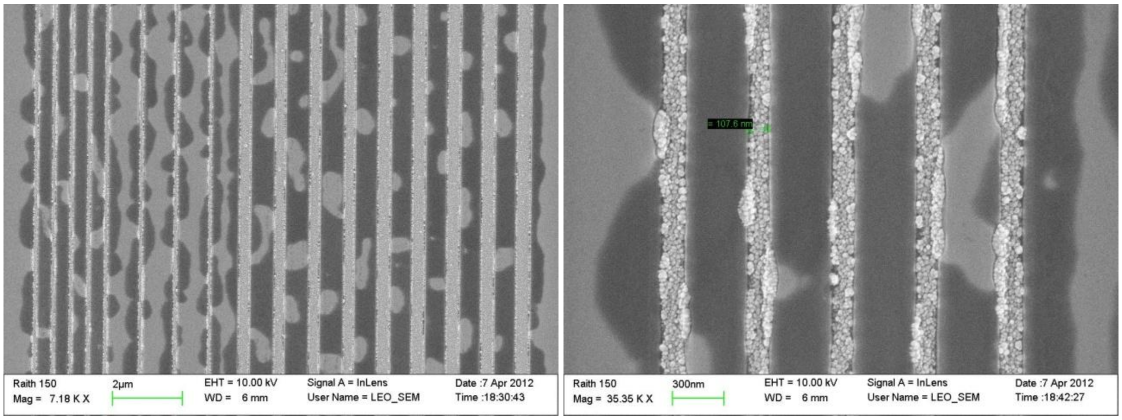

(a) (b)

Figure 4.6: SEM images of 3C-SiC micron-ribbons deposited on Si (111) patterned with SiO_2. (a) SiC ribbons with different linewidths and line spacings. (b) 107 nm wide SiC ribbons in 500 nm spacing.

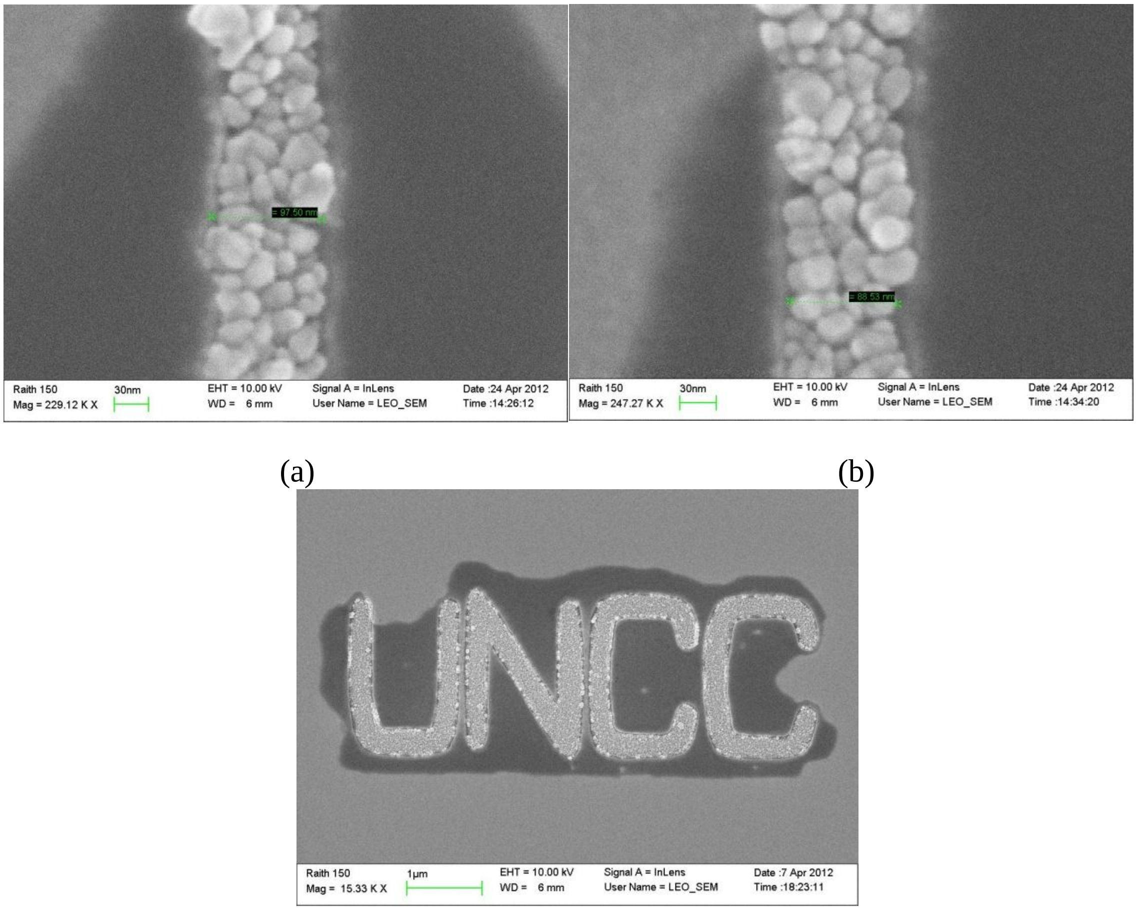

(a) (b)

(c)

Figure 4.7: SEM images of 3C-SiC nano-ribbons deposited on Si (111) patterned with SiO_2. (a) 97.5 nm linewidth. (d) 88.5 nm linewidth. (e) UNCC letters made of 3C-SiC.

The feasibility of selective deposition of 3C-SiC nanoribbon has been evaluated and confirmed, as shown in Figure 4.7. The sub-100 nm wide 3C-SiC nanoribbons could in principle be converted into graphene nanoribbons (GNRs) as the conductive channel in field effect transistors (FETs). In order to incorporate the selectively deposited 3C-SiC nanoribbon into FET transistor fabrication, three configuration designs were proposed: (1) single side-gated FETs with two different side-gated designs, shown in Figure 4.8, (2) single side-gated FETs with double sources and double gates shown in Figure 4.9 (a) and (b), respectively. Unlike other graphene-based FETs [24], all FET configurations in this study make use of existing SiO_2 deposition mask as the dielectric for the side gates, avoiding additional processes to place a top dielectric layer on the graphene channels. Thus, these designs are two dimensional device architectures, which offer more flexibility in the gate design.

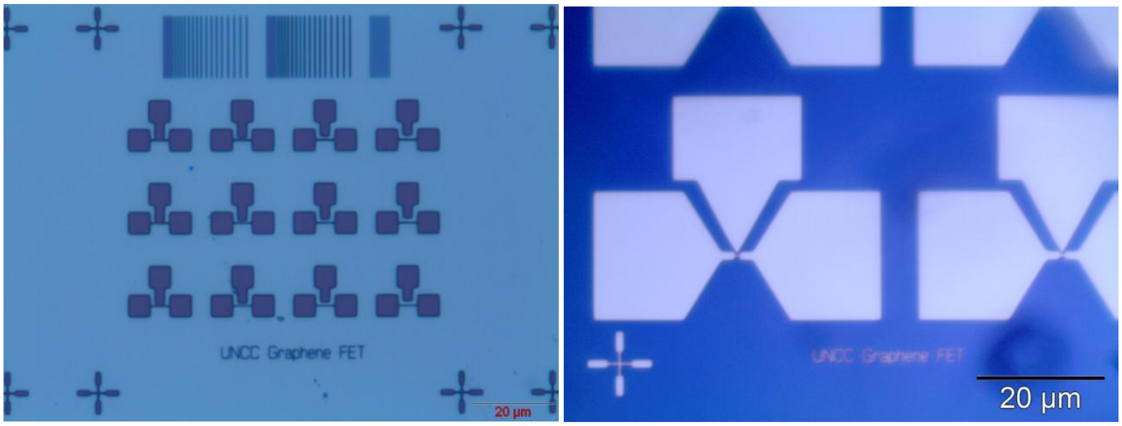

(a) (b)

Figure 4.8: (Optical image) Single side-gated FETs after e-beam lithography and developing. (a) and (b) Single side-gated FET configuration

After e-beam lithography and developing of ZEP520A-7, the patterned samples underwent ICP-RIE. During dry-etching, helium gas was induced to circulate the bottom

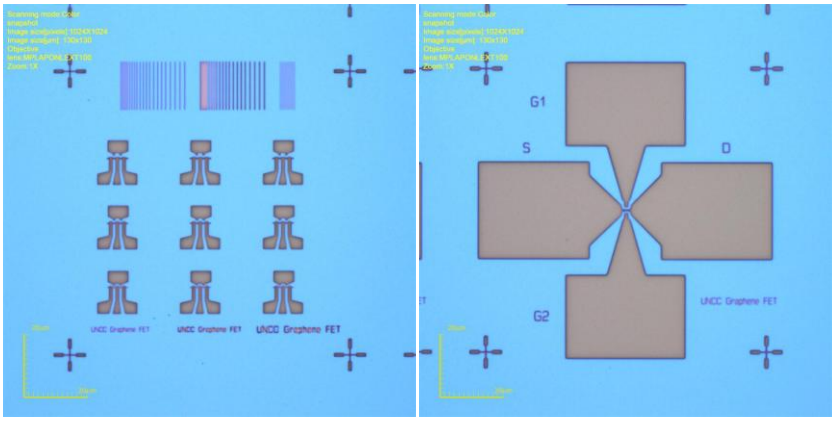

(a) (b)

Figure 4.9: (Optical image) Single side-gated FETs after e-beam lighography and developing. (a) Double-source FET configuration. (b) Double-gate FET configuration.

of sample in chamber to cool down the sample, avoiding burning the residual e-beam resist. The residual e-beam resist was removed by soaking sample in NMP solution at 40 ^{o}C with the assist of sonification vibration for about 10 minutes. Before MBE deposition of C60, the samples were cleaned in actone and methanol solution with assist of ultrasonification for 5 min. each, and blown dry with nitrogen gas. Figures 4.10 (a) and (b) a FET configuration and a 73 nm wide trench after RIE and resist striping, respectively.

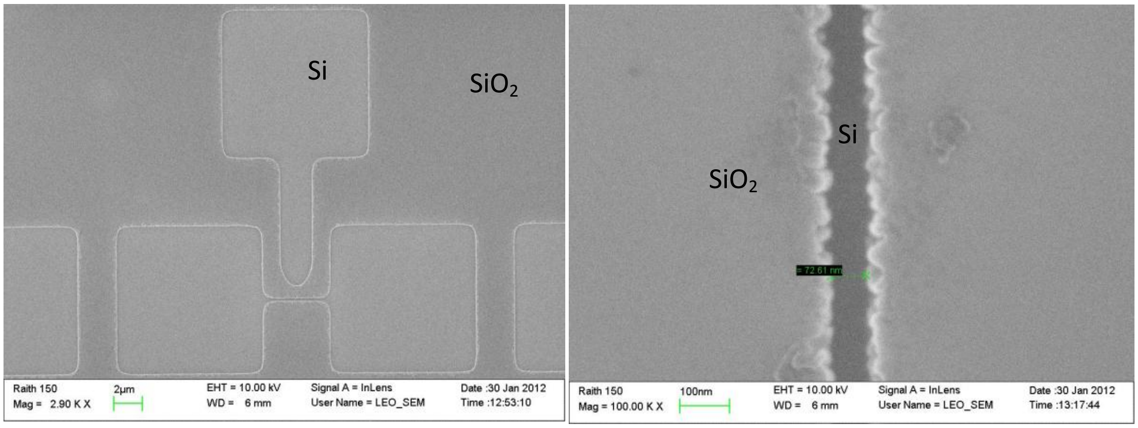

(a) (b)

Figure 4.10: FET configuration patterns after RIE etching and resist stripping. (a) FET (b) 73 nm wide trench.

After RIE etching, stripping of residual resist, and post-cleaning, the pattern substrate was loaded into MBE growth chamber for selective deposition of 3C-SiC with the process control as described in Chapter 2. The substrate temperature, source temperature, and growth time are 800 ^oC, 550 ^oC, and 8 minutes, respectively. During deposition, the sample spinner should be turned on to reduce shadow effect which is more significant for nanoscale structures. Figures 4.11 and 4.12 show SEM images of 3C-SiC selectively grown on the patterned Si substrates.

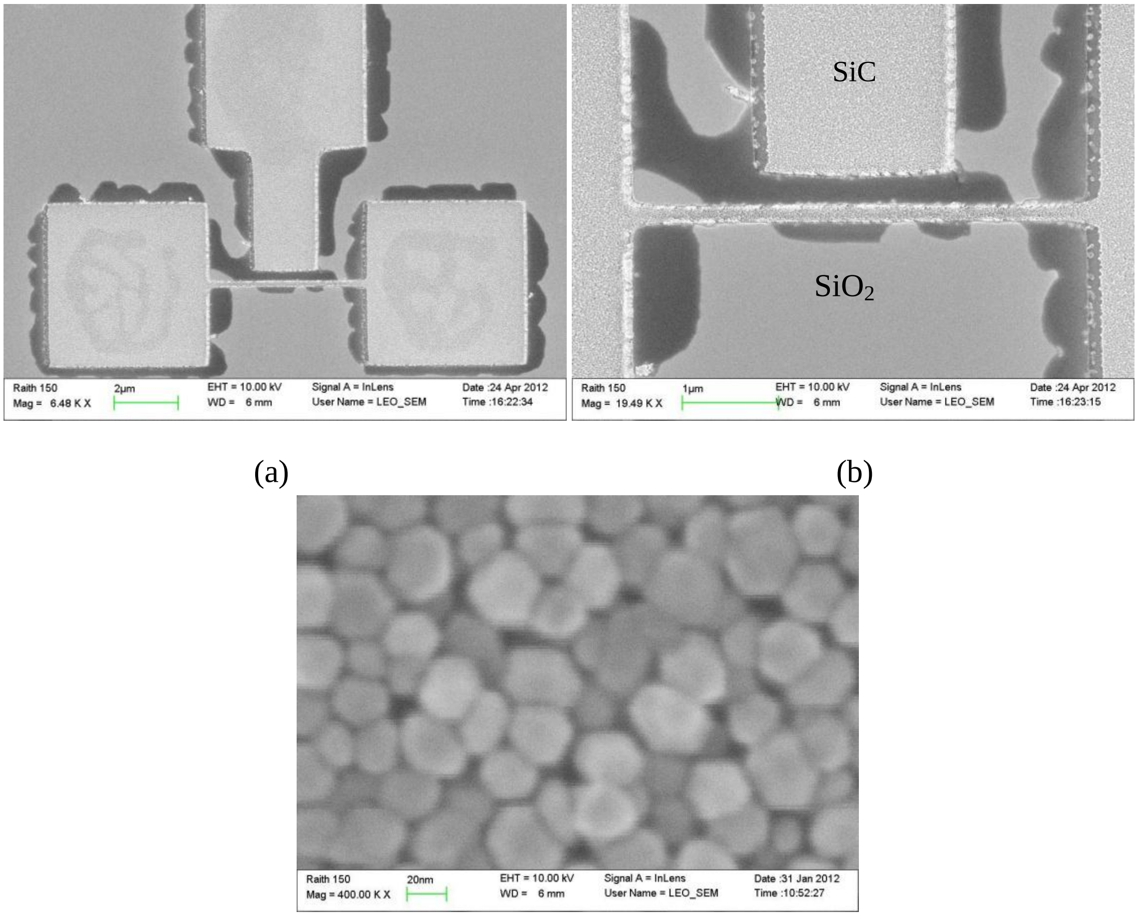

(a) (b)

(c)

Figure 4.11: SEM images of FET single side-gated configuration. (a) FET. (b) High magnification. (c) 20 ~ 25 nm polycrystal SiC grains.

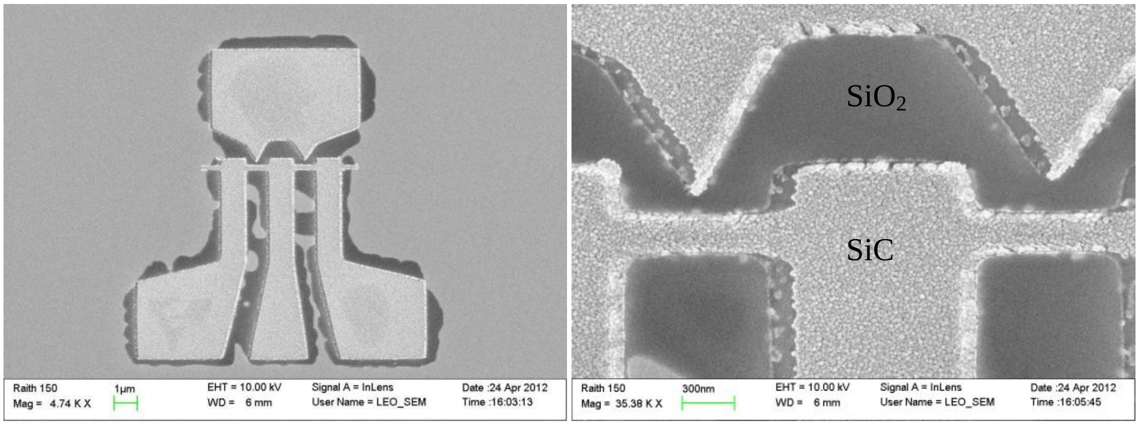

(a) (b)

Figure 4.12: SEM images of FET configuration made up of selectively deposited 3C-SiC on SiO_2 patterned Si (111). (a) FET. (b) Zoom-in view.

A simpler structure has also been fabricated for testing the conductivity of the graphene nanoribbon, i.e., one micron- or nano-scale SiC ribbon deposited by MBE with three electrodes deposited with e-beam evaporation, as shown in Figure 4.13.

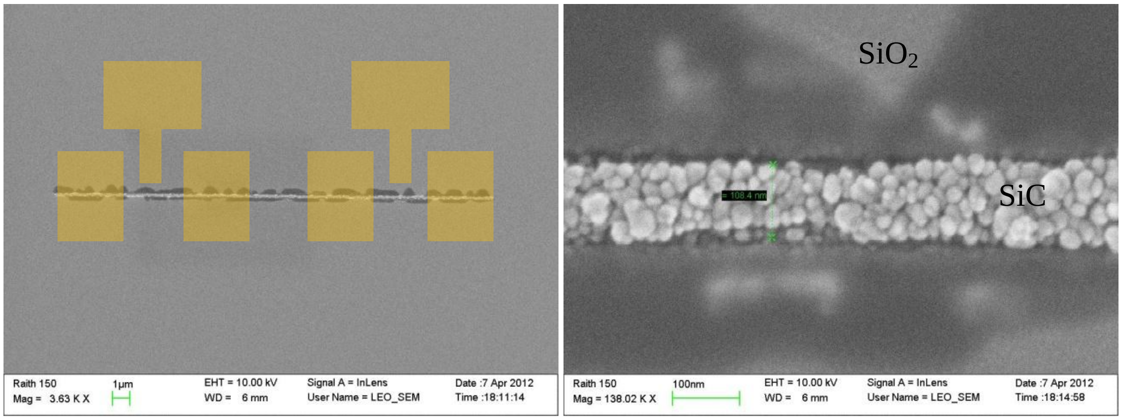

(a) (b)

Figure 4.13: A 3C-SiC ribbon selectively deposited for fabricating graphene ribbon. (a) A 20 μm long SiC ribbon. (b) Zoom in view.

Figure 4.14 shows letters were selectively deposited on a prepatterned Si (111) substrate. The letters are made up of 3C-SiC.

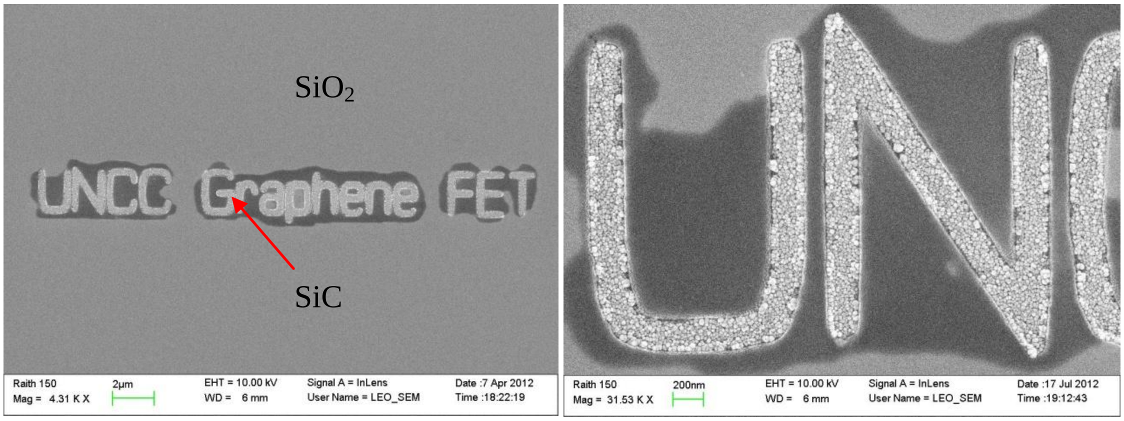

(a) (b)

Figure 4.14: SEM images of letters selectively deposited on Si (111). (a) Full view. (b) Zoom-in view.

Either the gate channel or all selectively deposited 3C-SiC areas could be converted into graphene, and then three electrodes, source, gate and drain, be deposited with 10 nm Ti/ 30 nm Au using an e-beam evaporation technique. Figure 4.15 shows the 10 nm Ti was deposited on three electrodes as a seed or adhesion layer, and then 30 nm Au was deposited on top as a conductive layer. A single side-gated FET configuration is shown in Figure 4.15.

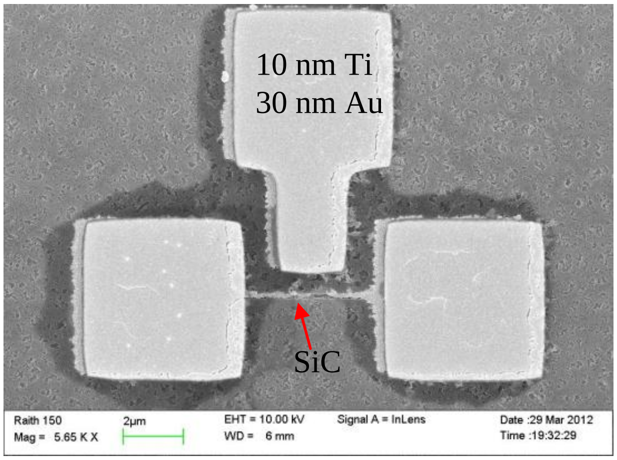

Figure 4.15: SEM image of single side-gated FET with 10 nm Ti/ 30nm Au e-beam evaporated on three terminals.

When attempting to convert selectively deposited 3C-SiC, we found that the currently available laser power about 30 mW was unable to convert small (below the laser spot size) SiC ribbons. The reason for this difficulty might be insufficient laser power on the SiC region to be absorbed by SiC or the SiC is too thin.

4.4 Summary and conclusions

Selecitve deposition of SiC on Si substrate has been demonstrated and proved to be an effective method to pattern micro-scale SiC structures that could in-principle be converted into graphene-based nanostucutres. Preliminarily, the SiC to graphene conversion with LIG process has been demonstrated for a structure with 5 μm SiC lines/5 μm SiO_2 spacings, achieved with photolithography and MBE growth . Raman mapping near 2D band shows graphene signature matching the illuminated areas. Subsequently, e-beam lithography, as a replacement for photolithography, was used to patterned submicron SiC structures. A SiC ribbon with the minimum linewidth of 88.5 nm was successfully deposited on Si susbtrate. Different FET configurations were selectively deposited on Si substrate with SiC. Since C60 flux is incident on Si substrate at about 45 degree rather 90 degree, the SiO_2 depostion mask would cause shadowing effect during MBE deposition; longer growth time should be used than that used for the growth on the whole wafer if same SiC thickness is expected. Another method to compensate shadow effect is to reduce the thickness of SiO_2. The rotation of substrate during growth also reduces shadowing effect and increase the homogeneity of SiC film. The thickness of selectively deposited SiC determined the absorption of light, so a thick SiC film helps to reduce the threshold laser power needed in converting SiC film into graphene layers. The electrode of 10 nm Ti/ 30 nm Au was successfully deposited on the selectively deposited

SiC using e-beam lithography and e-beam evaporation. The proposed technique for fabricating graphene nanoelectronic devices could be integrated into Si-based nanoelectronics. This study openes a route for integrating graphene synthesis process with conventional silicon device processes.

In addition, the fabricated SiC nanostructures on their own could be of interest for exploring their properties in the future.

CHAPTER 5: POWER AND TIME DEPENDENCE OF LASER-INDUCED 3C-SiC TO GRAPHENE CONVERSION

5.1 Experimental setup and sample selection

Since the quality of laser-induced graphene layers depends on laser power and illumination time, it is necessary to evaluate the correlation between graphene quality and illumination conditions. In this part of the study, μ-Raman spectroscopy was used as a monitoring technique. The Raman spectrum was collected right after laser irradiation. The changes in intensity, line position, line shape, and line width of G′ (2D) mode were monitored, acquired, and compared at different sets of power and time. A variable attenuator (Thorlab, Inc.) and a transistor-transistor-logic (TTL)-controlled shutter (Standford Research System, Inc.) were used to control irradiation power and time, respectively. The TTL pulse signal was generated by a function generator. The instrument set-up is shown in Figure 5.1.

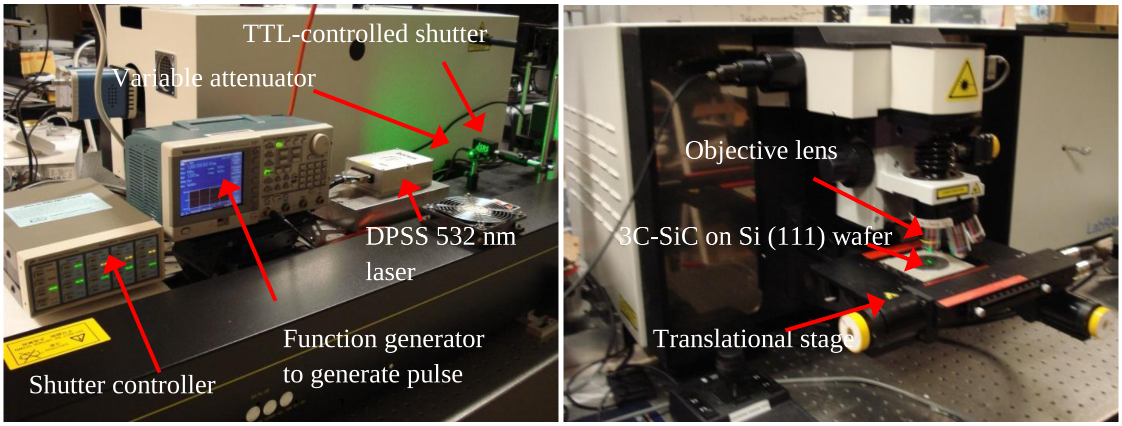

Figure 5.1: Experimental setup for writing graphene on 3C-SiC/Si (111). (a) Control of laser power and illumination time. (b) Focusing and positioning laser beam for forming graphene.

Three samples were selected for this evaluation. All three samples were grown at the substrate and source temperatures of 800 and 550 ^{o}C, respectively, for 10 minutes. The only differences between three samples are the cleaning processes which are listed in Table 5.1.

Table 5.1 Cleaning processes of three different samples

Sample	**Cleaning processes**
A	Acetone and methanol each for 5 minutes and blow dried with nitrogen
B	Same as the processes described in Table 2.1
C	RIE etching plus the cleaning process of A (selective growth)

The morphologies of the three samples are shown in Figure 5.2. It can be seen that sample A is roughest with an average domain size of 100 nm and smaller particle size, sample C is most uniform in grain size, and sample B falls in between grain size uniformity. The thickensss of three samples can be measured in SEM cross-section images as shown in Figure 5.3; the thickness of SiC films of samples A, B, and C are 188 nm, 188 nm and 51 nm, respectively. Although these three samples were grown with same growth conditions, the thickness of samples A and B are same and are more than three times that of sample C. This is caused by shadow effect during deposition in pre-patterned sample C. In other words, since the C60 source flux is incident on substrate at about 45 degree rather than 90 degree, only partial flux of source C60 was received by patterned substrate, resulting in that less carbon atoms reach the prepatterned trench (~ 100 nm) and thus thinner SiC. The minimum powers (thresholds) required for conversion were 10, 17 and 22 mW, which correspond to power densities of 2.6×10^6 W.cm^{-2}, 4.42×10^6 W.cm^{-2}, and 5.72×10^6 W.cm^{-2}, respectively, for three samples A, B, and C. 3C-SiC to graphene conversion occurred instantaneously under laser illumination with the power larger than the threshold value. The conversion time is shorter than 1 second. If the illumination time is longer than 1 second, the intensity of G′(2D) band will decrease , suggesting that the graphene material would be damaged by introducing defects or disorders. Therefore, the time scale was limited less than 1 second. In addition, the minimum exposure time of shutter is limited to 4 ms. Therefore, the illumination time varied from 1 s to 4 ms, with a 200 ms step from 1 s to 100 ms, 20 ms step from 100 ms to 10 ms, and 2 ms step from 10 ms to 4 ms.

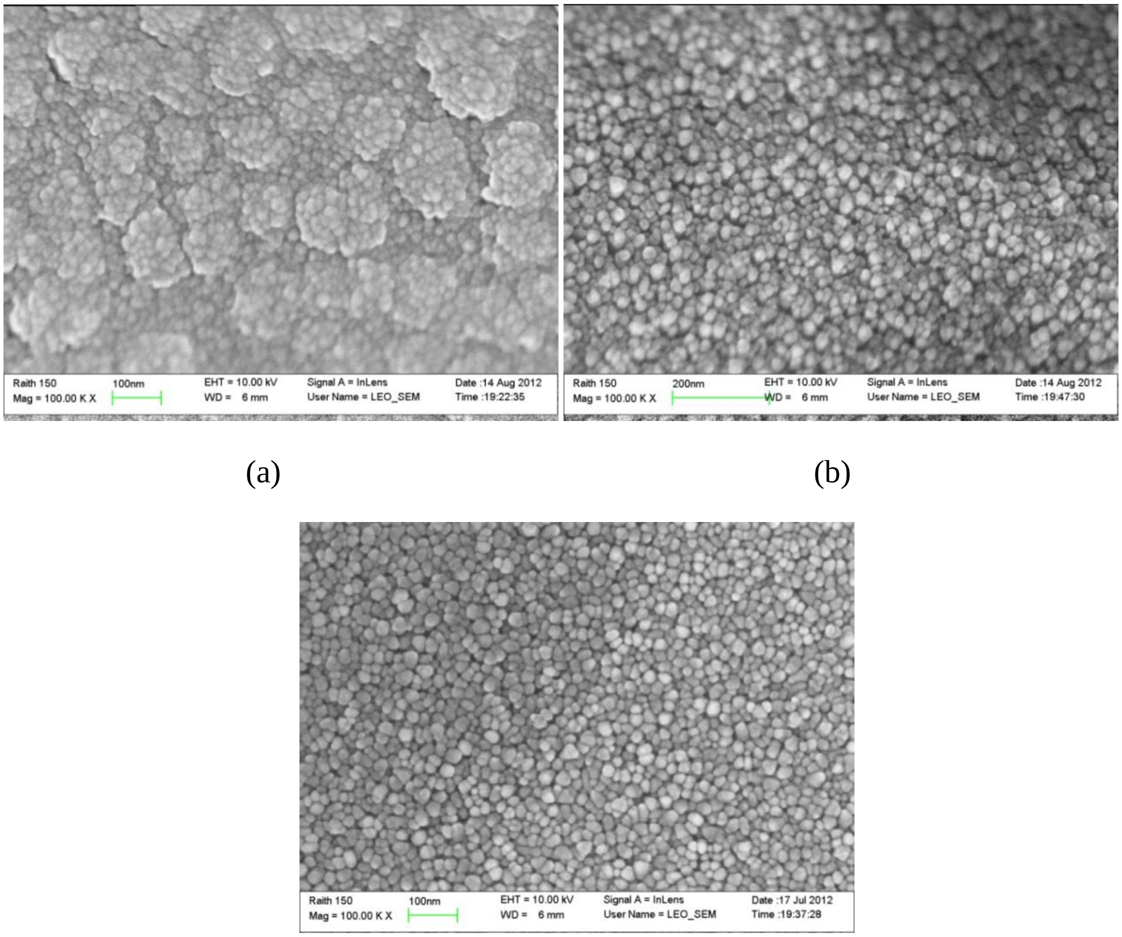

(a) (b)

(c)

Figure 5.2: SEM micrographs of 3C-SiC (111) grown on Si (111) substrates cleaned with three different conditions. (a) Sample A. (b) Sample B. (c) Sample C.

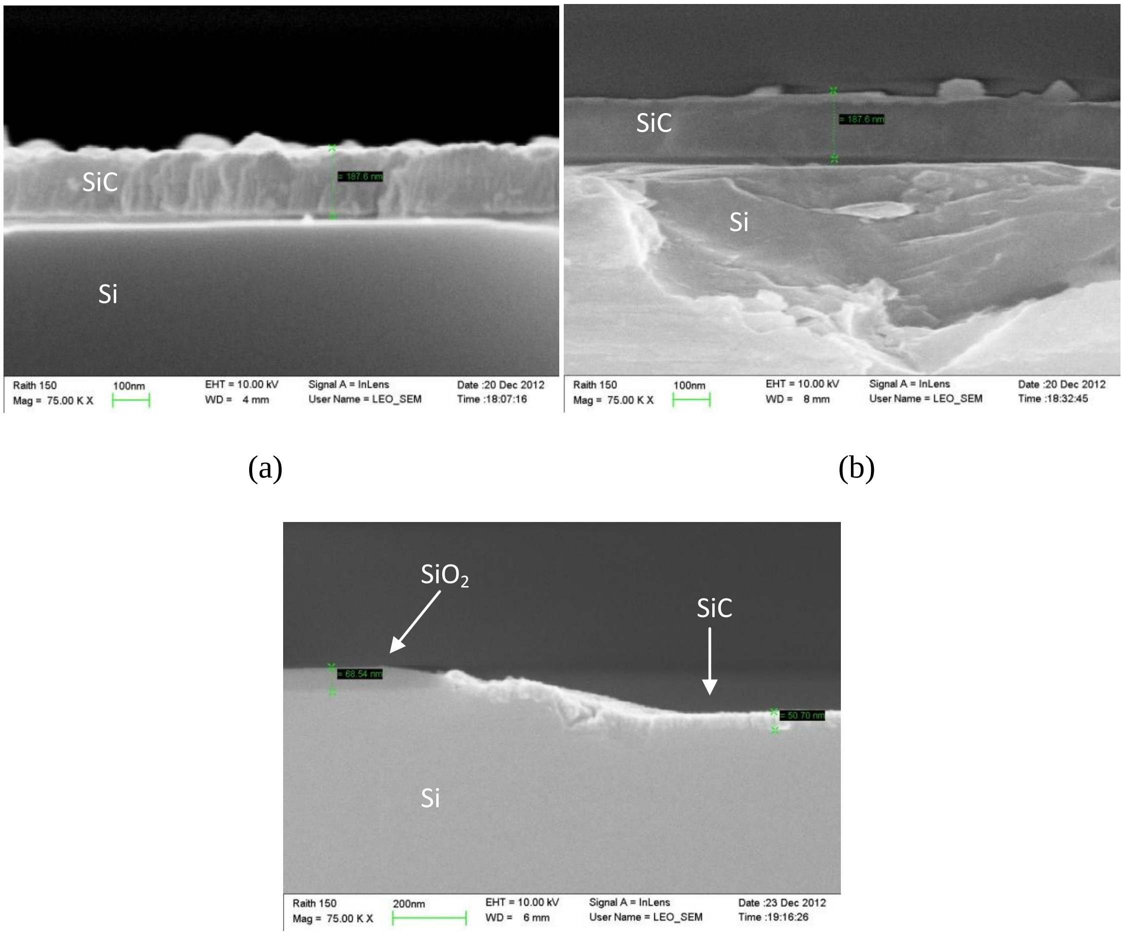

(a) (b)

(c)

Figure 5.3: SEM cross-section images of 3C-SiC (111) grown on Si (111). (a) Sample A (188 nm thick). (b) Sample B (188 nm thick). (c) Sample C (51 nm thick).

For sample A, we selected three illumination power values: 10, 12, and 14 mW. In order to make sure all spectra are comparable, 2D Raman mode of graphene is collected in one single spectrometer window. At each set of power and time, ten spots are first illuminated and measured with reduced power to avoid laser heating. The spectrum which occurred most frequently is selected for subsequent comparison with the spectra of other illuminated conditions. The Raman spectra near 2D band are compared in Figure 5.4. It can be seen that for the three illumination powers, the stronger 2D peaks concentrate on the illumination times of 4 and 6 ms or even shorter time which the shutter is incapable of controlling. The optimal illumination time might be shorter than 4 ms for three laser power values. The 2D peaks also upshift or downshift randomly without a clear relationship with respect to illumination time.

For sample B, five illumination power values were selected: 17, 19, 21, 23 and 25 mW, and the same evaluation method as sample A was used. The spectra comparison of different illumination conditions are shown in Figure 5.5. It can be seen that with the power increased from 17 to 25 mW, the optimal illumination time decreases from 1s to 8 ms. For sample C, five illumination power values were selected: 22, 23, 24, 25 and 26 mW, and the same evaluation method as sample A was used. The spectra comparison of different illumination conditions are shown in Figure 5.6. It can be seen that the optimal illumination time decreases from 1s to 80 ms along with the power increased from 22 to 26 mW. It can also be observed from three samples that 2D peak position shifts with the illumination condition. However, it changes randomly without clear relation with the illumination condition due to the inhomogeneity of SiC thin film.

5.2 Characterization and results

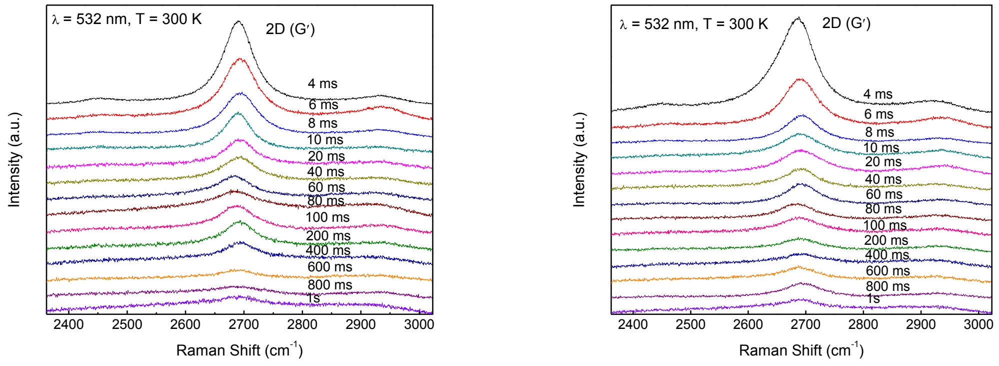

(a) (b)

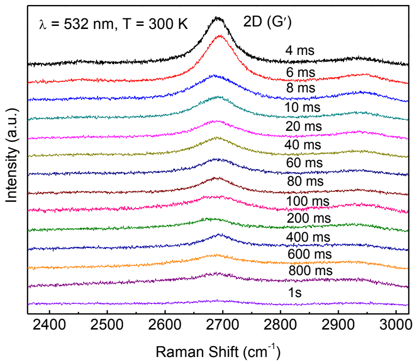

(c)

Figure 5.4: Raman spectra near the 2D band of laser-induced graphene on sample A at different powers and times: (a) 10 mW, (b) 12 mW, and (c) 14 mW.

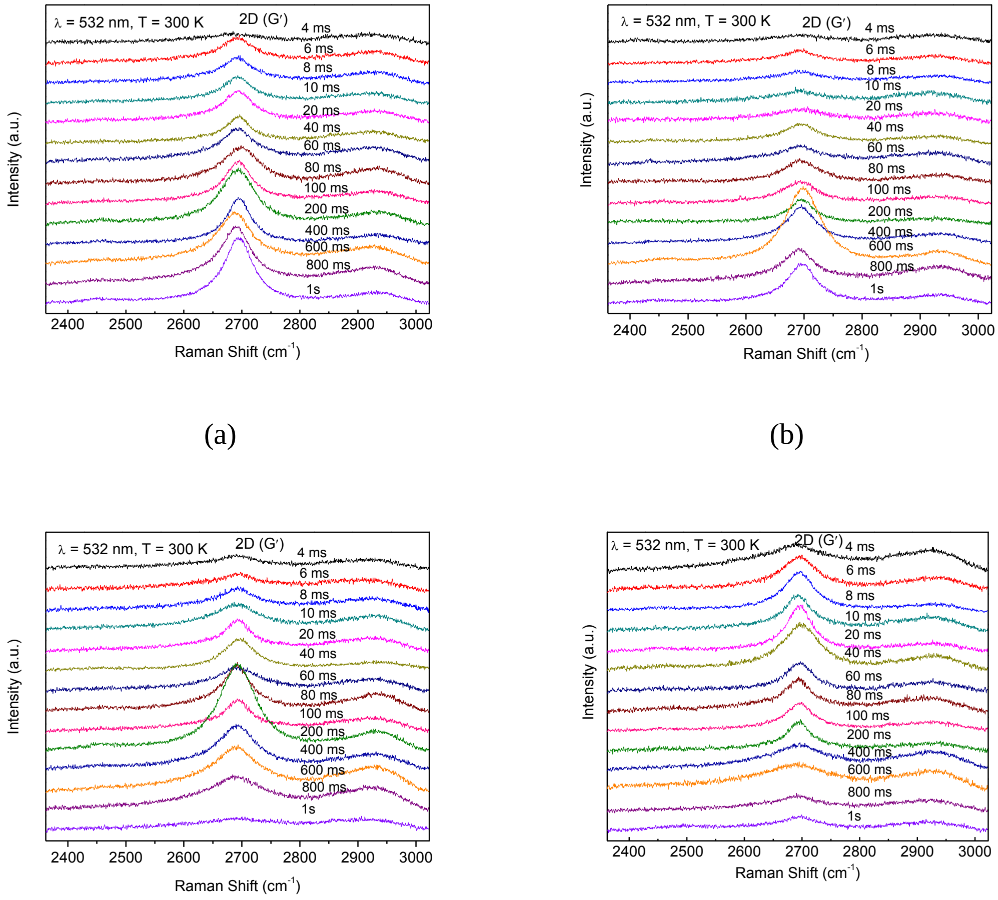

(a) (b)

(c) (d)

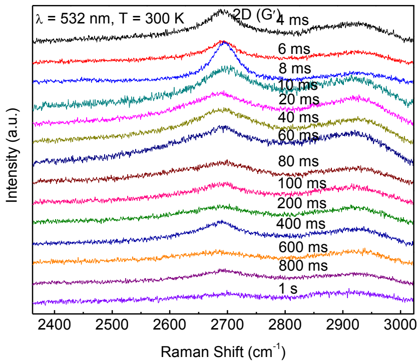

(e)

Figure 5.5: Raman spectra near 2D band of laser-induced graphene of sample B at different powers and times: (a) 17 mW, (b) 19 mW, (c) 21 mW, (d) 23 mW, and (e) 25 mW.

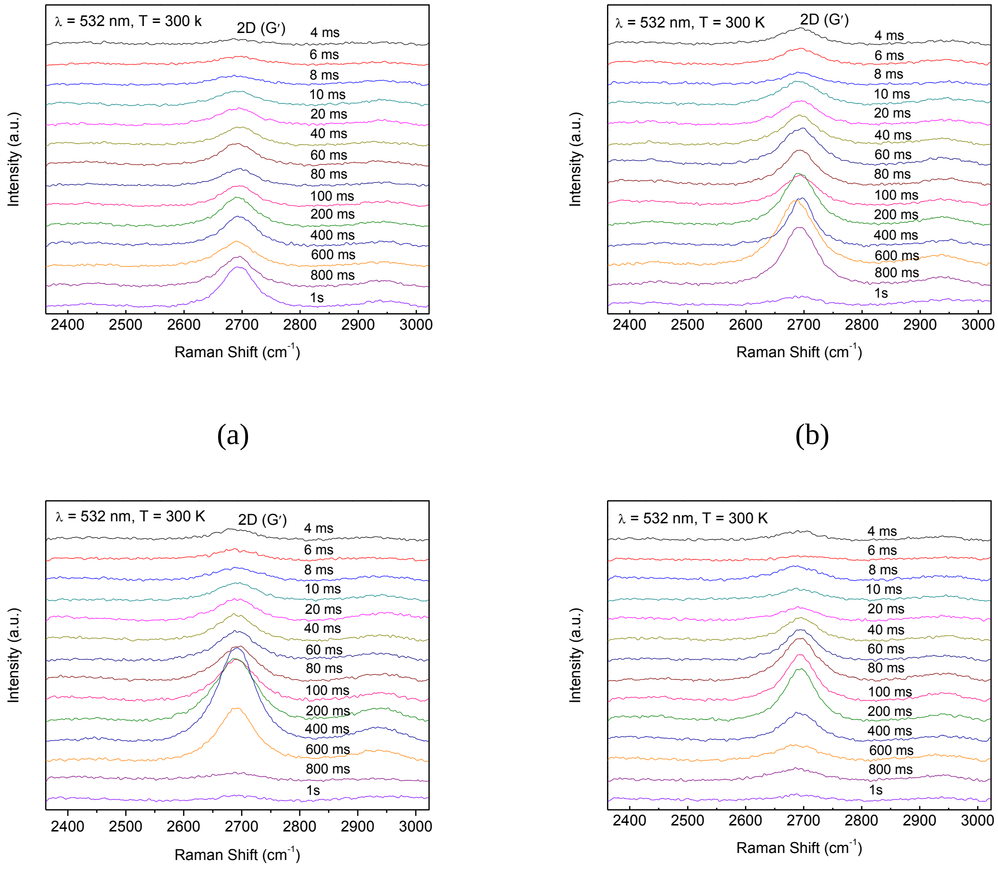

(a) (b)

(c) (d)

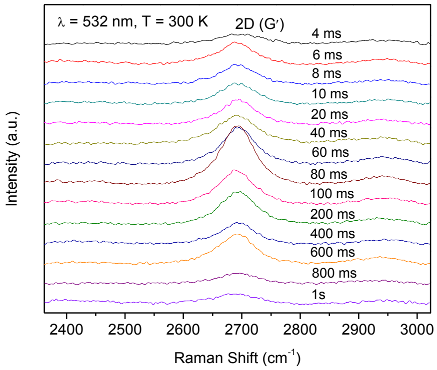

(e)

Figure 5.6: Raman spectra near 2D band of laser-induced graphene of sample C at different powers and times: (a) 22 mW, (b) 23 mW, (c) 24 mW, (d) 25 mW, and (e) 26 mW

The optimal illumination conditions, which are defined as for a given power the optimal time yielding the strongest 2D band intensity, are summarized in Figure 5.7. In general, at least for sample B and C, when the laser power increases, the illumination time decreses, but the relation is non-linear. This means that the optimal conversion does not simply depend on the dose, power, and illumination time, but has an activation process. For sample A, the variation is very small, possibly because the optimal illumination times were actually shorted than the shutter operation limit of 4 ms. In comparison with laser induced conversion of single crystalline SiC into graphene reported in the literature, the threshold power density for these polycrystalline SiC are substantially lower. For instance, the threshold power density of $4\text{x}10^7$ W/cm^2 was required for the single crystalline SiC [121]. However, the maximum power used in this study for polycrystal is 2.6 $\text{x}10^6$ W/cm^2, which is lower by more than one order of magnitude.

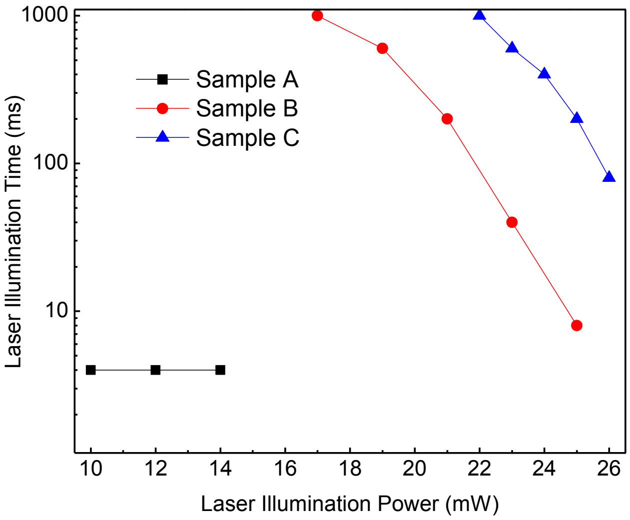

Figure 5.7: Laser illumination powers and times of three samples

5.3 Comparison of three samples

With the optimal illumination conditions identified in the above evaluation, the graphene layers were induced and measured with μ-Raman for three samples A, B and C. First, Raman spectra in a large spectral range from 400 to 3000 cm^{-1} were collected to compare overall spectra including three major peaks of graphene and characteristic LO mode of silicon substrate which can be used to calibrate the potential mechanical drift of the spectrometer. Figure 5.8 shows Raman spectra of graphene layers induced from the three samples with the respective optimal laser illumination conditions. Although all three spectra show obvious defect or disorder D modes, the D/G ratios which are used to calculate the crystallite size of graphene sheets are different [194]. The general equation for the determination of the domain size L_a of micrographite is given as [194],

$$L_a = (2.4 \times 10^{-10})\lambda_l^4 \left(\frac{I_D}{I_G}\right)^{-1} \quad (5)$$

where, L_a is the crystalline domain of graphene sheet, λ_l is the wavelength of excitation laser, and $\frac{I_D}{I_G}$ is the integral intensity ratio of D to G modes.

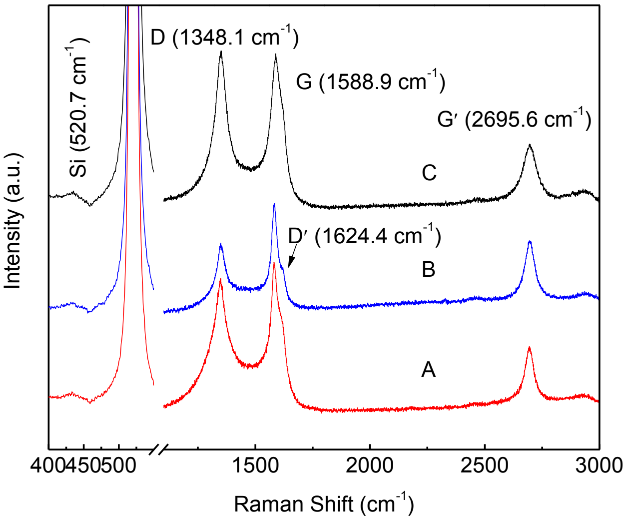

Figure 5.8: Raman spectra of laser-induced graphene layers from the three samples A, B and C with respective optimal illumination conditions.

According to the Equation 5, the domain size of graphene layers from the three samples are calculated and listed in Table 5.2.

Table 5.2: Crystallite sizes of graphene layers on samples A, B and C

Sample	**A**	**B**	**C**
I_D	4031	1323	4261
I_G	3280	1619	34198
$\left(\frac{I_D}{I_G}\right)^{-1}$	0.81	1.22	0.80
L_a ***(nm)***	16	23	15

It can be seen from Table 5.2 that graphene crystallite size L_a of sample B is somewhat larger than those of sample A and C. It is probably because that the native oxide on sample A was not removed completely, resulting in more defects in 3C-SiC and thus in graphene layers, and the higher threshold illumination power requested by sample C might introduce more disorders in graphene layers.

5.4 Summary and conclusions

The optimal laser illumination power and time for LIG on three samples A, B, and C were evulated and identified to be (10mW/4ms, 12mW/4ms, and 14mW/4ms), (17mW/1s, 19mW/600ms, 21mW/200ms, 23mW/20ms, and 25mW/8ms), and (22mW/1s, 23mW/600ms, 24mW/400ms, 25mW/200ms, and 26mW/80ms), respectively. The optimal illumination times for three samples are all sub-second. With the increase of illumination power, the optimal illumination time decreases, but the relationship is nonlinear. The threshold illumination power depends on the microstructure or morphology of polycrystal SiC films. The substrate of sample A with a few nanometers thick native SiO_2 introduces some defects into SiC film with 100 nm domain size and smallest grain size. The smaller grain size leads to more grain boundary and thus reduces thermal conductivity, increasing local temperature under laser illumination. As a consequence, sample A has the lowest threshold illumination power. Comparison between samples B and C shows that polycrystal SiC film in sample B is less uniform in grain size than than in sample C because SiC film (188 nm thick) in sample B is much thicker than that in sample C (51 nm thick) due to the shadowing effect in MBE growth (shown in Figure 8.2). The low uniformity of sample B results from the difficulty in interdiffusion between silicon and carbon through the thick SiC film (as shown in Figure 5.9). In Figure 5.9, it can be seen that at the beginning of growth, it is easy for carbon atoms to react with silicon atoms to form uniform SiC; however, when SiC becomes thicker, it is difficult for Si atoms in the underneath Si substrate to diffuse toward the surface of SiC film to react with carbon atoms, forming SiC; similarly, the thicker SiC film also prevents carbon atoms from diffusing down to react with Si in Si substrate. Therefore, the thicker SiC thin film, the less uniform SiC thin film. More defects, less uniformity, and less crystallinity contributes to the lower threshold illumination power. Another factor is the thicker SiC film in sample B compared to sample C absorbs more light and thus increases the local temperature.

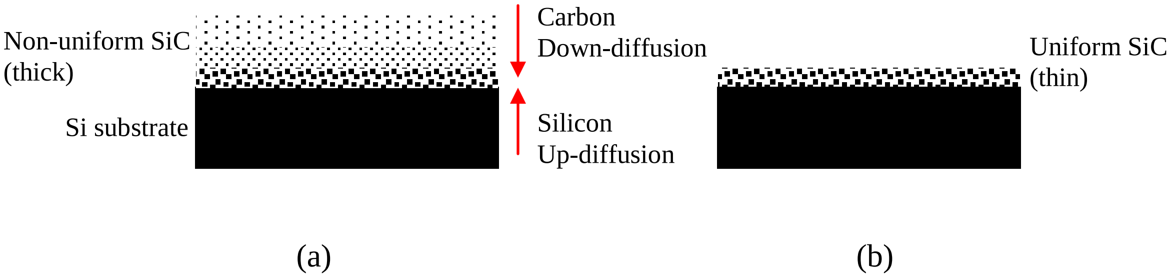

Figure 5.9: Schematic illustration of SiC film formation mechanism. (a) Thick SiC. (b) Thin SiC.

The graphene domain sizes (crystallite size) of three samples were estimated by employing an empirical formula and taking Raman spectrum. Graphene domain size of sample B is 23 nm and larger than those of samples A and C, which are 16 and 15 nm, respectively. The samller graphene domain size of sample A is due to smaller grain size of SiC, and the threshold power is lower; and the smaller graphene domain size of sample C is probably because the threshold power is relatively high with respect to samples A and B. Therefore, the threshold illumination power and graphene domain size depend on the microstructure of polycrystalline SiC film, which can be tuned with the MBE growth conditions and cleanliness of silicon substrates.

CHAPTER 6: ELECTRICAL CHARACTERIZATION OF GRAPHENE MICRO-RIBBON

6.1 Fabrication of electrodes on graphene μ-ribbon

Electrical conductivity and mobility of large area graphene have been studied and reported [7]. However, up to date, electrical characterization on laser-induced graphene has not been reported yet. Some preliminary work on conductance measurement on laser-induced graphene layers was carried out in this study. E-beam lithography and e-beam evaporation were used to make FET configuration over laser-written graphene μ-ribbon. The process flow for the fabrication of graphene-ribbon- based FET is shown in Figure 6.1. The process started with patterning alignment makers used for writing graphene μ-ribbon on 3C-SiC (111)/Si(111) using laser and for overlay of electrodes, as shown in Figure 6.2. In Figure 6.2 (c), the two arrows in the center are used as alignment markers to write a 20 μm graphene ribbon in between two arrows. The four crosshairs in the four corners are used to overlay electrodes for making the FET configuration based on laser-induced graphene μ-ribbon. The laser writing technique is the same as that described in Chapter 3. After an array of 20 μm graphene-ribbons was written on 3C-SiC(111)/Si(111). The sample was spin-coated with ZEP520A-7 at the spinning rate of 5000 rpm for 60 seconds, and then underwent pre-baking, e-beam lithography, developing, and post-baking, as described in Chapter 4. Finally, e-beam evaporation of 10 nm Ti and then 30 nm Au, and lift-off of metallization on ZEP520A-7 were carried out to pattern the electrode terminals of the graphene-based FET configuration, as shown in Figure 6.2. After the graphene μ-ribbon was written on 3C-SiC (111)/ Si(111), the metallization between source and gate as well as between drain and gate were difficult to be lift-off due to the narrow distance and roughness of laser-illuminated area. The gate electrodes in between sources and drains were removed to ease metallization lift-off processes. As a result, the electrical conductance can be measured with only two electrodes. Figures 6.2 (a) and (b) show that two electrodes were patterned on 3C-SiC (111)/Si(111) without and with laser-induced graphene underneath. However, the electrode metallization over the transition from unilluminated to illuminated area is slightly discontinuous due the larger ablation caused by larger laser power. Therefore, the conductivity is very low. Another attempt is to use sample A described in Chapter 5. The SEM images of electrode metallization over laser-induced graphene μ-ribbon, as shown in Figure 6.2 (c) and (d), show better continuity of electrode metallization of the transition area between illuminated and un-illuminated areas. Therefore, the electrical conductance measurement was focused on sample A. Keithley 4200 semiconductor characterization system was employed for this purpose. Figure 6.3 shows two probes on two electrodes overlaid over laser-induced graphene.

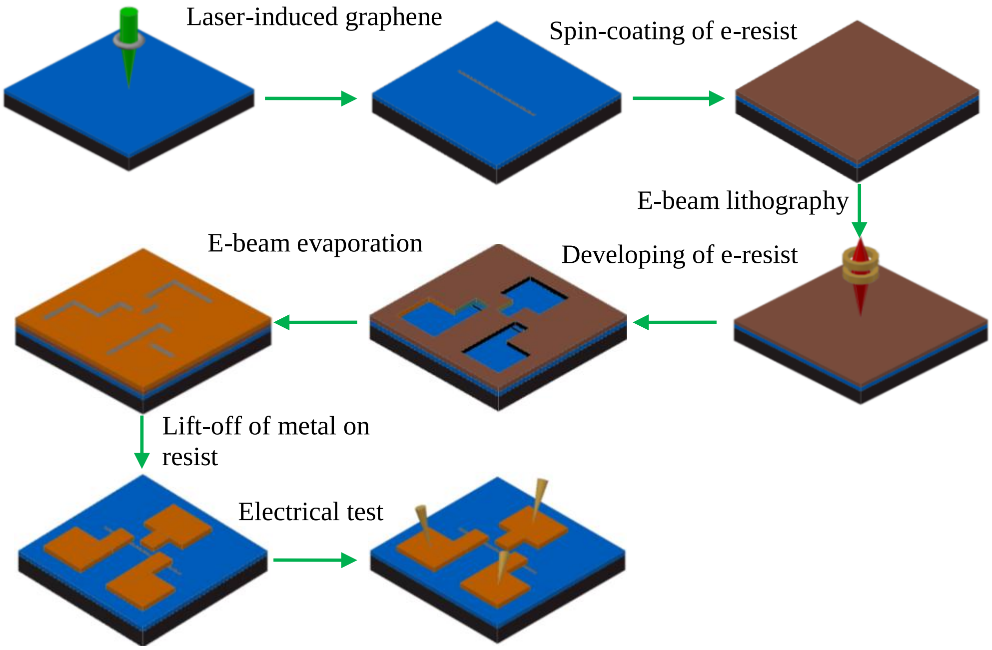

Color	⬛	🟦	🟫	🟧	🟨	▨
Materials	Si (111)	3C-SiC	ZEP520A-7	Ti/Au	W/Au	graphene

Figure 6.1: Process flow for patterning electrodes on laser-induced graphene μ-ribbon

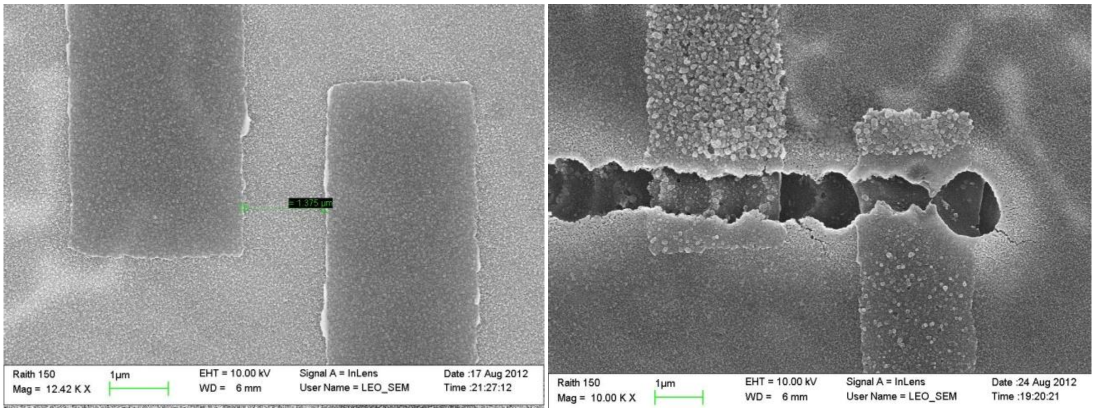

(a) (b)

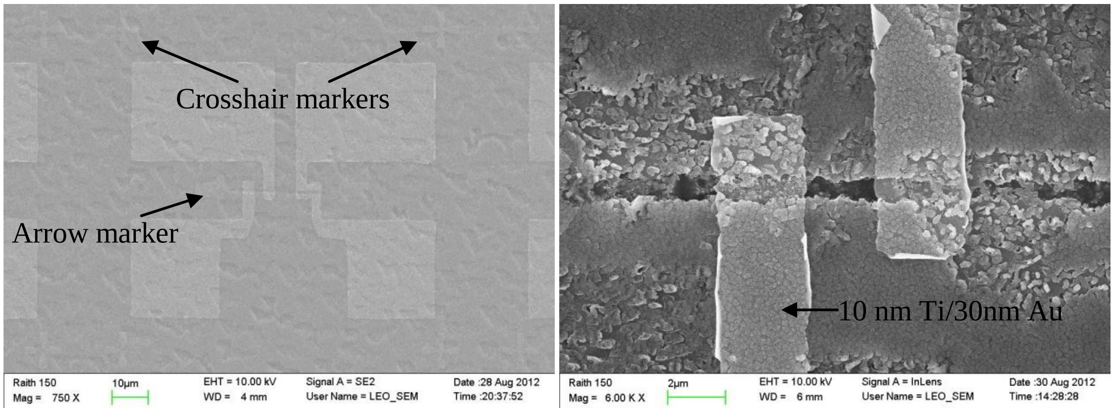

(c) (d)

Figure 6.2: SEM images of two electrode patterned on 3C-SiC (111)/Si(111).
(a) Electrodes on SiC (sample B). (b) Electrodes on LIG (sample B). (c) Electrodes on SiC (sample A). (d) Electrodes on LIG (sample A).

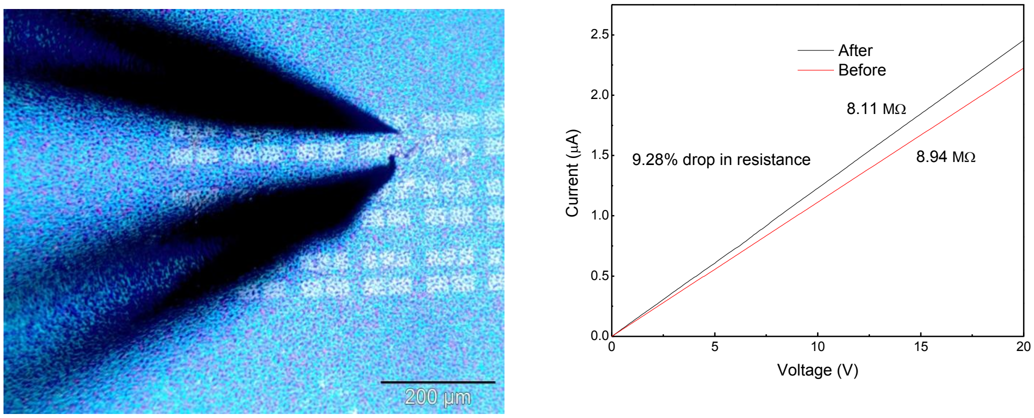

(a) (b)

Figure 6.3: Electrical characterization of LIG graphene. (a) ET setup. (b) I-V curve.

6.2 Electrical test and results

Keithley 4200 semiconductor characterization system was employed to measure electrical conductance of graphene micro-ribbon written by laser. Two micro-probes (Micromanipulator model 7A) were to contact the electrodes deposited on graphene micro-ribbon. Two-terminal resistance configuration with source measurement units SMU1 and SMU2 was used to measure resistance of graphene micro-ribbon. I-V curve are plotted and shown in Figure 6.3. The resistance of graphene micro-ribbon before and after LIG process is about 8.94 and 8.11 MΩ, repectively. There is only 9% drop in resistance after laser illumination. This means that the graphene micro-ribbon is composed of small graphene domains with low carrier transport between them, and they are either discrete or slightly in touch with each other. Therefore, the poor physical continuity of graphene micro-ribbon results in low electrical conductance.

6.3 Summary and conclusions

A graphene micro-ribbon device for electrical conductance measurement was designed, fabricated and tested. The micro-electrodes were successfully overlaid on graphene micro-ribbon using e-beam lithography and e-beam evaporation techniques. Electrical resistance measurement shows 9% drop in electrical resistance after laser illumination. The laser-induced graphene micro-ribbon is not physically continuous and thus shows low electrical conductance. Since the graphene micro-ribbon was written point by point, it is likely made up of discrete graphene domains. If graphene micro-ribbon is created by line illumination of a laser beam, the whole graphene ribbon would be formed simultaneously instead of a serial process, and the physical continuity and thus electrical conductance could be improved.

CHAPTER 7: PATTERNING OF GRAPHENE MICRO- OR NANO- STRUCTURE

7.1 Experimental setup

As described in Chapter 1, graphene layers fabricated with different synthesizing techniques have different applications. For instance, micro-scale size graphene produced by micromechanical exfoliation, though of high quality, is not scalable for wafer scale mass production; large size graphene synthesized by CVD decomposition of hydrocarbons on metals is suitable for fabricating graphene-based nano-devices in wafer scale mass production, but the transfer of graphene from a metal to an insulating substrate is required; epitaxial growth of graphene on SiC single crystal is applicable to wafer scale fabrication of graphene-based nanoelectronics, but the high cost and relatively small wafer size avaibale of SiC single crystals are the major limitation of this approach; and exfoliation and reduction of graphite oxide, though with some defects and of low electron mobility, has a good application in fabricating large area electrodes in super-capacitors. Laser annealing technique, limited by the small laser spot size, though not applicable to producing large size graphene, could be used to pattern graphene nanostructures for applications such as photonics, nano-optoelectronics, electron-photon superstructures, etc. In this chapter, we demonstrate some graphene micro- dots or discs arrays patterned with laser illumination on SiC film. Alternatively, with the pre-patterned growth of 3C-SiC dots or discs in nanosclae using the selective deposition of 3C-SiC on Si (111), graphene dots or discs in nanoscale can also be achieved. 3C-SiC is a good dielectric and substrate

Si can act as an insulating or a semiconducting material. With a three-layer structure graphene/3C-SiC/Si, electron-photon superstructure can be realized and applied as photonic crystal. Three selected samples A, B and C was illuminated with their optimal illumination conditions identified in Chapter 5, and then Raman mapping over G′ (2D) mode of graphene was carried out on three illuminated dots. The Raman images of the three dots in the spectral range of 2650-2750 cm^{-1} and their corresponding SEM images are shown in Figure 7.1. It can be seen from the SEM images in Figure 7.1 that after laser illumination, the 3C-SiC was re-crystallized near the illuminated spot and graphene layers mainly formed on the re-crystallized 3C-SiC at the illuminated site. Samples B and C show the central part of the re-crystallized 3C-SiC were ablated off. This may be due to the higher illumination laser powers than that of sample A. Figure 7.2 shows a graphene distribution in a donut shape in sample B resulting from a laser power slightly higher than the power used for the dot shown in Figure 7.1 (c). This means that the graphene shape can be changed by tuning laser irradiation conditions. Following the demonstration of patterning and Raman-mapping of single graphene dot, multi-graphene dots in an array were patterned by synchronizing an external shutter with the internal shutter in Raman system. One TTL signal controlled by Raman system software simultaneously control two shutters: one for laser source and the other for the Raman signal collection. The array of graphene dots was formed by moving stage in a preset step that determines the separation between graphene dots.

7.2 Characterization and results

In Figure 7.1, Raman mapping images which show the distribution of laser induced graphene layers with the corresponding SEM images of the laser-illuminated spots. The higher laser powers used for samples B and C result in larger ablated spots and the over-exposed central area due to the Gaussian profile of the laser power. Thereofore, larger laser power threshold value does not lead to uniform LIG graphene layers. Also, higher laser power also causes the cracking of SiC near the illuminated spot, as shown in Figures 7.1 (c) and (e). Figures 7.1 (a) and (b) show a relatively uniform graphene dot in sample A, which was created with relatively lower illumination power. For samples B and C (see below).

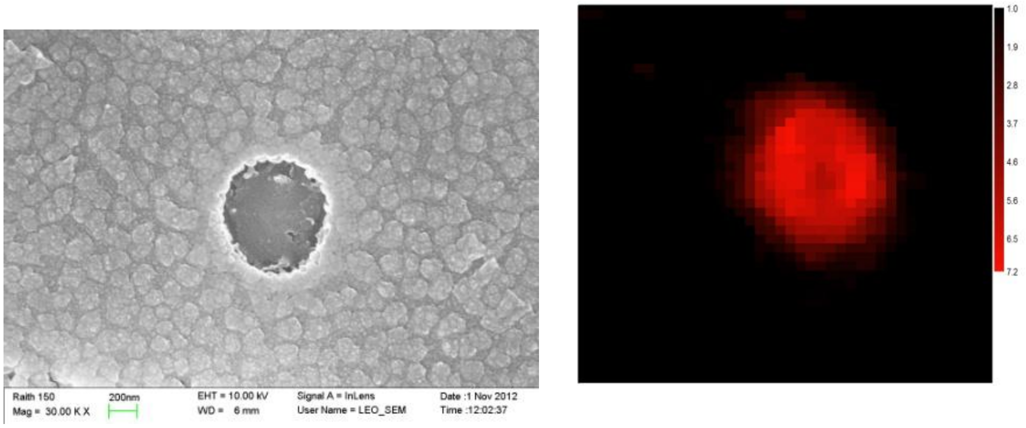

(a) (b)

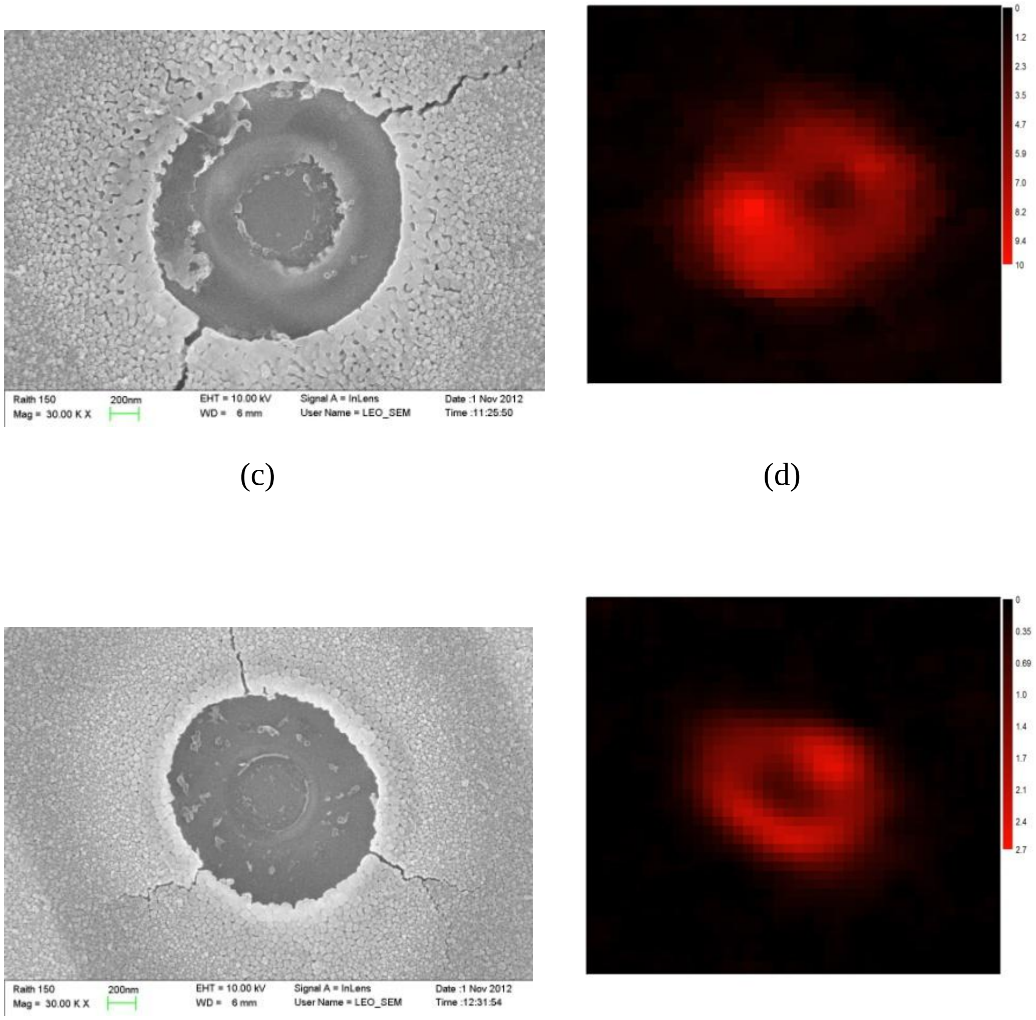

(c) (d)

(e) (f)

Figure 7.1: SEM images and corresponding Raman images (4×4 μm^2) of three dots illuminated with laser on three samples A, B, and C. (a) and (b) Sample A. (c) and (d) Sample B. (e) and (f) Sample C (Raman spectral range: 2650 ~ 2750 cm^{-1}).

Figures 7.1 (c) and (d) show a graphene dot in donut shape in sample B, which was created by a slightly higher laser power than that used in Figures 7.1 (a) and (b). The central part of dot was over exposed and then probably lost materials. Therefore, laser illumination power could be tuned to generate graphene in different shapes.

Similar to the LIG process to create single graphene dots, two, four, and nine graphene dots in arrays 1 × 2, 2 × 2, and 3 × 3 were also patterned by programmed laser illumination conditions, respectively. Following the patterning of graphene dots, Raman mapping was performed on the pattern areas, and the Raman images are shown in Figure 7.2.

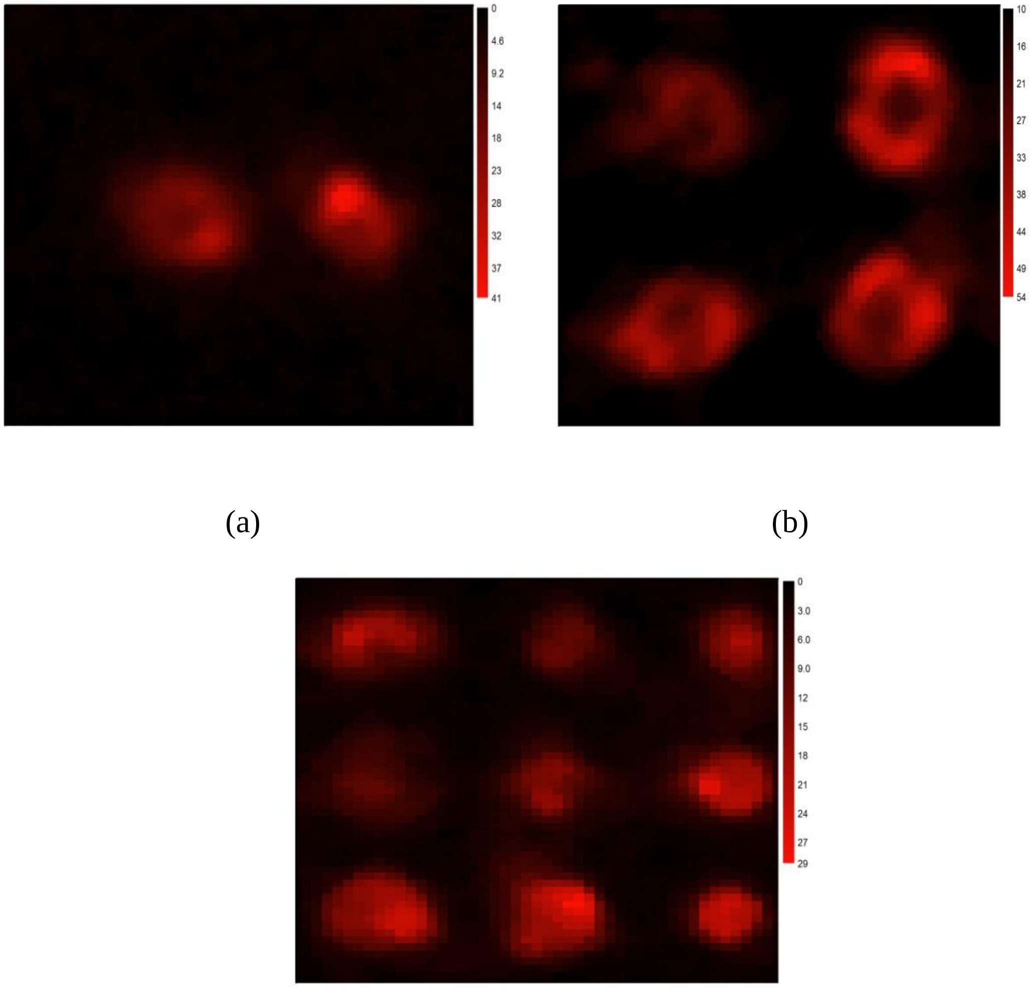

(a) (b)

(c)

Figure 7.2: Raman mapping images (2650-2750 cm^{-1}) of graphene dots in different arrays. (a) 2 dots in (1 × 2) array (image size: 6×6 μm^2). (b) 4 dots in (2 × 2) array (image size: 6×6 μm^2). (c) 9 dots in (3 × 3) array (image size: 9×9 μm^2).

In addition to the patterning of 0D graphene dot arrays, 1D graphene ribbon was also patterned. Figure 7.3 shows a Raman mapping and SEM images of a graphene μ-ribbon.

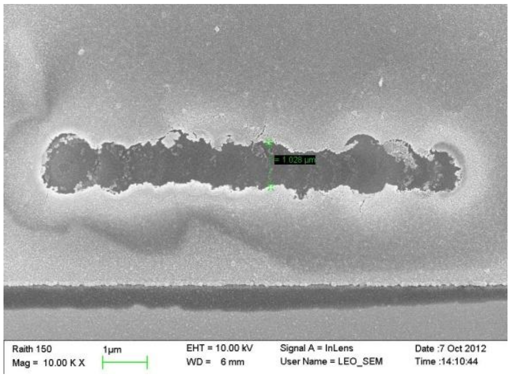

(a)

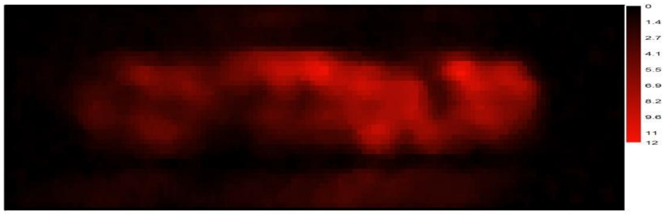

(b)

Figure 7.3: SEM and Raman mapping images of a graphene μ-ribbon. (a) SEM. (b) Raman mapping image (2650-2750 cm^{-1}) (Image size: 14×4 $\mu\mathrm{m}^2$).

In order to investigate the carbon and silicon distribution after laser illumination, EDS was performed on sample C as shown in Figure 7.4. Figure 7.4 (a) show in the central irradiated area of the laser illuminated spot, the ratio of carbon to silicon to oxygen is 52.3: 45.0: 2.7; Figure 7.4 (b) shows the ratio in the boundary area is 49.5: 46.6: 3.9; and Figure 7.4 (c) shows the ratio in the nonirridated but adjacent area is 46.4: 50.8: 2.9. Therefore, under laser illumination, silicon was sublimated from the irradiated area and transposed to the surrounding non-illuminated, leaving carbon in the central area to form graphene, and some silicon might be oxidized near the boundary and non-irradiated area because more oxygen was detected. The carbon content was found the highest in the illuminated spot, despite that because of the ablation more Si from the substrate could be probed thus potentially reducing the ratio of C. The actual C content could be even higher. Moreover, EDS shows oxygen in three areas due to the laser illumination in air. Oxygen in the irradiated area induces defects or disorders to graphene layers and thus contributes to the D peak in Raman spectrum. Oxygen in the boundary may be due to oxidation because of the high local temperature, and Oxygen in non-irradiated area may be due to oxidation of sublimated Si or the oxidation during growth.

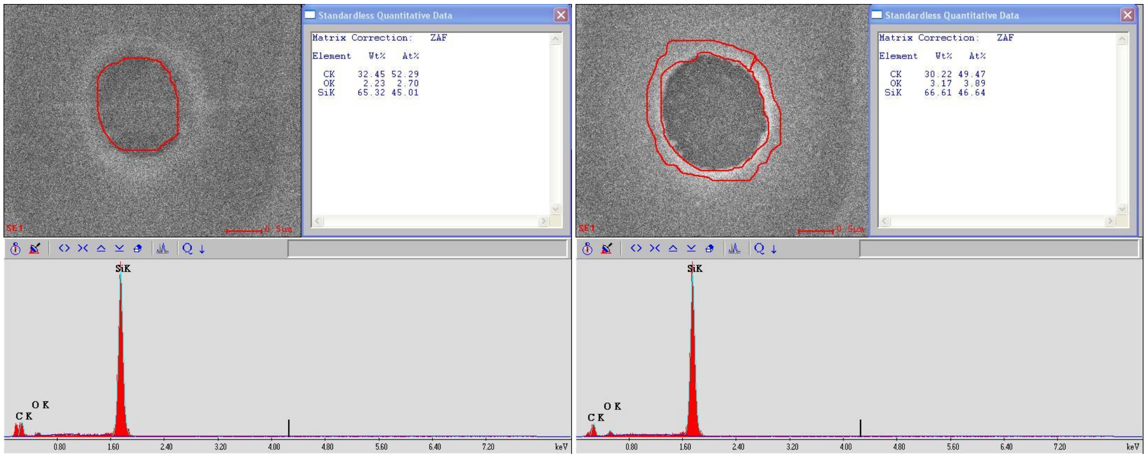

```
Matrix Correction:   ZAF

Element   Wt%   At%

  CK     32.45 52.29
  OK      2.23  2.70
 SiK     65.32 45.01
```

```
Matrix Correction:   ZAF

Element   Wt%   At%

  CK     30.22 49.47
  OK      3.17  3.89
 SiK     66.61 46.64
```

(a) (b)

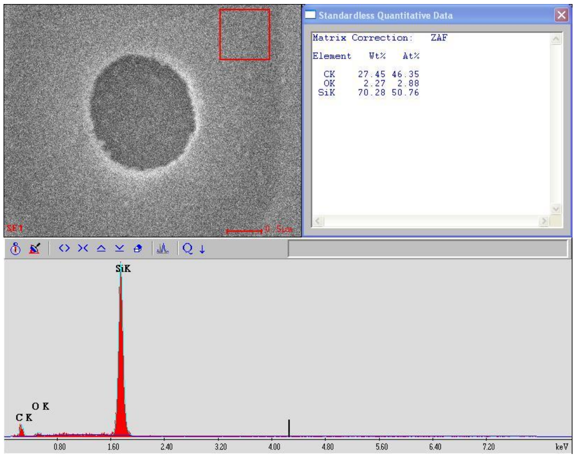

```
Matrix Correction:   ZAF

Element    Wt%   At%

  CK      27.45  46.35
  OK       2.27   2.88
 SiK      70.28  50.76
```

(c)

Figure 7.4: EDS results of laser-illuminated spot on SiC film grown on SiC (111) (sample C). (a) Irradiated area. (b) Boundary area. (c) Nonirradiated area.

7.3 Summary and conclusions

The application of the LIG technique to patterning periodic graphene microstructures was demonstrated and evaluated. The distribution of graphene in illuminated area is more uniform for sample requiring a lower threshold power. The threshold power depends on the microstructure, morphology, and thickness of SiC film. The graphene shape can be modified by tuning the illumination power. EDS elemental analyses after laser illumination indicate that silicon was sublimated and transferred to the adjacent non-irradiated area with some oxidation. More oxidation is found in the boundary due to higher local temperature. Carbon was left in the irradiated area, forming graphene layers. Oxygen was also detected in irradiated area, which introduces defects or disorders into graphene layers. UVH or low pressure Ar may be employed as illumination atmosphere to reduce the oxidation.

The periodic graphene microstructures were patterned and characterized with Raman mapping. The Raman image near 2D mode indicates the graphene layers distribute in the irradiated area, matching SEM image of the irradiated spot. A graphene ribbon of 1 μm × 10 μm was written and mapped. With the assist of selective deposition of SiC on Si substrate, periodic nanostructures of graphene could also be generated. The periodic multi-layer nanostructure, graphene (conductor)/SiC (dielectrics), could form electron-photon superstructures used in nanoelectronic and photonic applications.

CHAPTER 8: CONCLUSIONS AND PROPOSALS

8.1 MBE growth of SiC on Si substrates

The growth of SiC on the Si substrate using C60 source has been reported in the literature [195-197]. The grown SiC materials were polycrystalline in nature, thus, the materials were inferior to the single crystalline SiC in terms of material quality, such as the electronic conductivity. In this work, the primary intent is not to improve the material quality for electronic applications, but to explore the growth conditions that can yield SiC thin-films with different surface morphology and crystallinity to be converted into graphene structures using the laser illumination technique.

(A) Source and substrate temperature dependence

The MBE growth conditions for depositing SiC polycrystal thin film on Si (100) and (111) using C60 (as carbon source) and Si wafers (as both silicon source and supporting substrate) have been investigated systematically in this research work. With a constant growth time of 5 minutes, the growth temperature combinations (T_{sub}/T_{C60}) include 700/450, 700/550, 700/650, 800/450, 800/550, 900/450, 900/550, 1000/450, and 1000/550 ^{o}C. These growth conditions were evaluated and compared in terms of the uniformity, roughness, and crystallinity of SiC polycrystal thin film.

At T_{sub} = 700 ^{o}C, T_{C60} = 550 ^{o}C yields more uniform crystalline SiC on Si (100) or (111) than 450 and 650 ^{o}C do, as can be observed in Figures 2.4 and 2.7, because 450 and 650 ^{o}C generate either insufficient or excessive C60 flux, respectively. It can be obviously seen from Figures 2.4 (a), (c), and (e) that SiC film coverage on Si (100) increases from T_{C60} = 450 to 550 to 650 ^{o}C, though it is not obvious for SiC on Si (111) because of the higher atomic density of Si (111). However, the comparison between Figures 2.7 (b), (d), and (f) shows that the roughness of SiC film on Si (111) increases from T_{C60} = 450 to 550 to 650 ^{o}C. The roughest SiC grown at T_{C60} = 650 ^{o}C results from the excessive decomposed C60 on SiC film, as confirmed by the strong D and G bands in Raman spectra of SiC at T_{sub}/T_{C60} = 700/650 ^{o}C in Figure 2.18 and Figure 2.19. Similarly, Raman spectra of SiC at T_{sub}/T_{C60} = 700/550 ^{o}C also show weak D and G bands, and SiC/Si (111) has less C60 than SiC/Si (100) does because more Si atoms from the higher atomic density of Si (111) react with carbon atoms. Although SiC films on Si (100 and (111) grown at T_{sub}/T_{C60} = 700/450 ^{o}C are smoother than those at T_{sub}/T_{C60} = 700/550 ^{o}C, Raman 1st TO modes of SiC (Table 2.6) show amorphous SiC at T_{sub}/T_{C60} = 700/450 ^{o}C and crystalline 6H-SiC at T_{sub}/T_{C60} = 700/550 ^{o}C. It can also be observed from Figure 2.11 that at T_{sub}/T_{C60} = 700/550 and 700/650 ^{o}C, SiC films on Si (111) show 2θ peaks corresponding to 6H-SiC, but SiC films on Si (100) do not. Therefore, because of the higher atomic density of Si (111), it is easier to form crystalline SiC on Si (111) than on Si (100) at T_{sub}/T_{C60} = 700/550 and 700/650 ^{o}C, and the coverage of SiC on Si (111) is higher than that on Si (100). The comparisons of Figures 2.7 (a) with (c) and Figures 2.7 (d) with (b) show that the grain sizes increase with the increase of T_{C60} from 450 to 550 ^{o}C. This means the increase of source temperature T_{C60} not only increases C60 flux also increases the grain size of SiC.

At T_{sub} = 800 ^{o}C, T_{C60} = 550 ^{o}C yields rougher SiC with larger grain size on both Si (100) and (111) than T_{C60} = 450^{o}C does [Figures 2.5 (a) and (b), Figures 2.6 (a) and (b),

Figure 2.8 (a) and (b), and Figure 2.9 (a) and (b)]. This is because the higher flux and kinetic energy of C60, which result from T_{C60} = 550°C, contribute to the crystallization and thus increase the grain size of SiC. However, at T_{sub} = 900 and 1000 °C, T_{C60} = 550 °C yields smoother SiC with larger grain size on both Si (100) and (111) than T_{C60} = 450°C does (Figures 2.5, 2.6, 2.7 and 2.8). This is because the reaction rate, crystal growth, and diffusion increase with $T_{sub,}$ and higher T_{sub} require higher C60 flux to provide carbon atoms to react with silicon atoms. Therefore, insufficient C60 flux at lower T_{C60} = 450 °C leads to more non-uniform SiC, especially for higher T_{sub} = 900 and 1000 °C. At T_{C60} = 550°C, SiC on Si (111) is always smoother than that on Si (100) at T_{sub} = 800, 900, and 1000 °C because of the higher atomic density of Si (111) (Figures 2.5 and 2.6).

XRD 2θ scan spectra indicate crystalline 3C-SiC (200) was formed on Si (100) at T_{sub}/T_{C60} = 900/550 and 1000/550 °C, and crystalline 3C-SiC (111) was formed on Si (111) at T_{sub}/T_{C60} = 700/550, 700/650, 800/450, 800/550, 900/550, and 1000/550 °C, because corresponding 2θ peaks were observed in Figure 2.11. However, Lorentzian decomposition of both XRD 2θ peak and the 1st order TO modes of SiC indicates that SiC is either 6H phase or the mixture of 6H and 3C phase, depending on the growth temperatures. On Si (100), SiC grown at T_{sub}/T_{C60} = 900/550 and 1000/550 °C are mixture of 3C-SiC (200) and 6H-SiC (104), and 3C phase increases with T_{sub} from 900 to 1000 °C because d-spacing is closer to that of single crystal 3C-SiC (Table 2.4) and Raman TO mode of 3C-SiC is measurable (Table 2.8) at T_{sub} = 1000 °C. On Si (111), SiC grown at T_{sub}/T_{C60} = 700/550 °C is crystalline 6H-SiC (102), SiC grown at T_{sub}/T_{C60} = 700/650 °C is low crystalline 6H-SiC (102) (broad 2θ peak), SiC grown at T_{sub}/T_{C60} =

800/450 ^{o}C is low crystalline 6H-SiC (102) (broad 2θ peak), SiC grown at T_{sub}/T_{C60} = 800/550 ^{o}C is the mixture of crystalline 6H-SiC (102) and 3C-SiC (111), SiC grown at T_{sub}/T_{C60} = 900/550 ^{o}C is the mixture of crystalline 6H-SiC (102) and 3C-SiC (111), and SiC grown at T_{sub}/T_{C60} = 1000/550 ^{o}C is the mixture of crystalline 6H-SiC (102) and dominating 3C-SiC (111). Therefore, on Si (111), 3C phase also increases with T_{sub} from 800 to 1000 ^{o}C. It is easier to form SiC on Si (111) than Si (100) at the above-mentioned growth conditions because of the higher atomic density of Si (111). XRD omega (ω) scans shown in Figure 2.23 indicate $FWHM_{\omega}$ of SiC grown on Si (100) and (111) at T_{C60} = 550 ^{o}C decreases slightly from T_{sub} = 800 to 900 ^{o}C but significantly from T_{sub} = 900 to 1000 ^{o}C. This implies the lateral coherence of SiC crystallite increases significantly from T_{sub} = 900 to 1000 ^{o}C for SiC on both Si (100) and (111) because diffusion, nucleation rate, and crystal growth rate exponentially depend on the temperature. However, XRD omega-2theta ($\omega - 2\theta$) scans shown in Figure 2.24 indicate that $FWHM_{(\omega-2\theta)}$ of SiC on Si (100) decreases significantly from T_{sub} = 800 to 900 ^{o}C but slightly from T_{sub} = 900 to 1000 ^{o}C, and the vertical coherence of SiC crystallite increases significantly from T_{sub} = 800 to 900 ^{o}C but slightly from T_{sub} = 900 to 1000 ^{o}C because the vertical coherence depends on the out-diffusion of Si underneath SiC. On the contrary, $FWHM_{(\omega-2\theta)}$ of SiC on Si (111) decreases slightly from T_{sub} = 800 to 900 to 1000 ^{o}C, and the vertical coherence of SiC crystallite increases slightly from T_{sub} = 800 to 900 to 1000 ^{o}C because the temperature dependence of out-diffusion of Si is not so much as that on Si (100). This is because the higher atomic density of Si (111) makes it easy for Si to out-diffuse to the surface of SiC. It can also be observed from Figure 2.24 (b) that ω value of SiC/Si (111) at T_{sub} = 800 ^{o}C is smaller than those of SiC at T_{sub} = 900 and 1000^{o}C, and according to the Bragg's law, the d-spacing of SiC/Si (111) at T_{sub} = 800 ^{o}C should be larger than those of SiC at T_{sub} = 900 and 1000^{o}C. Therefore, SiC/Si (111) at T_{sub} = 800 ^{o}C might sustain a compressive strain. Figure 2.35 shows clearly that the grain size of SiC grown on Si (111) increases from T_{sub} = 700 to 800 to 900 to 1000 ^{o}C.

(B) Substrate orientation dependence

SiC thin films grown on three Si substrate orientations, Si (100), (110) and (111), at two growth conditions, T_{sub} (^{o}C) /T_{C60} (^{o}C) /time (min) = 800/550/10 and 1000/550/20, have been studied. XRD spectra shown in Figure 2.29 display 2θ peaks of 3C-SiC (200) when grown on Si (100), and 3C-SiC (111) on Si (110) and Si (111). At T_{sub} (^{o}C) /T_{C60} (^{o}C) /time (min) = 800/550/10, 3C-SiC on Si (110) is more uniform than that on Si (100) and Si (111) due to the highest area atomic density of Si (110). However, at T_{sub} (^{o}C) /T_{C60} (^{o}C) /time (min) = 1000/550/20, 3C-SiC on Si (111) is more uniform than that on Si (100) and Si (110), and excessively decomposed C60 was observed on 3C-SiC/Si (110) as white particles of about 10 nm in diameter (Figure 2.26), because the higher atomic density of 3C-SiC/Si (110) make it more difficult for silicon to out-diffuse to the surface of the denser 3C-SiC to react with decomposed C60. It is observed that at T_{sub}/T_{C60}/time = 800 ^{o}C/500^{o}C/10min, 3C-SiC (111) on Si (111) and (110) has much narrower $FWHM_{\omega}$ and thus better crystallization than 3C-SiC (200) on Si (100) (Figures 2.30 (a)). However, at T_{sub}/T_{C60}/time = 1000 ^{o}C/500^{o}C/20min, $FWHM_{\omega}$of 3C-SiC (200)/Si (100) is close to that of 3C-SiC (111)/Si (111) and /Si (110) (Figure 2.30 (b)), because the high diffusivity of Si and C at high temperature compensate the difference in area atomic density. Based on the XRD omega scans (Figure 2.30 (c)), at growth conditions of T_{sub}/T_{C60} =800/550 ^{o}C for 10 minutes and T_{sub}/T_{C60} =1000/550 ^{o}C for 20 minutes, 3C-SiC/Si (111) sustains tensile strain because the d-spacing is smaller than that of single crystal, but both 3C-SiC/Si (100) and 3C-SiC/Si (110) sustain compressive strain because the d-spacing is larger than that of single crystal. It might be due to the complicated inter-diffusion process of silicon and carbon atoms through SiC thin film. The tensile strain on 3C-SiC/Si (111) should be one of the reasons that 3C-SiC (111) /Si (111) is the easiest to be induced into graphene layers under the same laser illumination conditions (Figure 3.6). The tensile strain on SiC on Si (111) grown at T_{sub}/T_{C60} =1000/550 °C was also confirmed by the redshift of LO mode of SiC in Raman spectra (Figure 2.32). Single crystalline SiC film in 10 nm domain and polycrystalline SiC film in 30 nm domain were shown in TEM image and electron diffract pattern.

In overall consideration of the uniformity, roughness and crystallinity of SiC thin film, and available laser illumination power, growth condition of T_{sub}/T_{C60}/time=800 °C/550 °C/10min was selected to grow SiC thin film to be converted into graphene layers.

8.2 Laser induced SiC-to-graphene conversion

(A) Characterization of LIG and its comparison with other transferred graphene samples

A CW 532nm Nd-YAG laser of ~ $(2.6\sim8) \times 10^6$ W/cm^2 was used to convert SiC/Si (111) into graphene layers. SiC/Si (111) grown at T_{sub}/T_{C60}/time =800 °C/550 °C/10min was found to have the strongest graphene Raman signature (2D band) under the same laser illumination among three Si orientations (100), (110), and (111) due partially to the tensile strain in SiC/Si (111). The laser and power density used in this study were compared with those used in other LIG-related research works. For those works involved with single crystal SiC wafers, typically pulsed lasers were used with peak power densities at least one order of magnitude higher than that used in this study (Table 3.1) because the lower thermal conductivity (resulting from grain boundary) of polycrystalline SiC film contributes to the increase of local temperature, thus reducing the threshold power density. However, the power density used to illuminate sintered polycrystalline SiC bulk [119] was even lower than that used in this study by about two orders of magnitude because single crystalline Si substrate in this study dissipates more heat than polycrystalline SiC bulk does. The Raman spectra of laser induced graphene show all the graphene major phonon modes, such as G and 2D. The defect-induced D mode was also observable because 700 nm laser spot size produces graphene layers of similar size with defect concentrated on edge, resulting in that D band signal from defective and symmetry-broken edge was also collected in the Raman spectrum. Moreover, the oxygen in air may also induce defects or disorders in LIG graphene. The symmetrical 2D mode indicates the stacking order of the laser-induced graphene is turbostratic [193]. The reduction in the TO mode intensity of 3C-SiC after laser illumination also indicates the decomposition of SiC, and the remaining TO mode indicates that 3C-SiC layer was not totally decomposed, with some left and re-crystallized on Si substrate (Figure 7.1). TEM cross-section image (Figure 3.3) of graphene layers shows the inter-spacing between graphene layers is about 3.7 Å which is larger than 3.35 Å, the inter-spacing of single crystal graphite. Therefore, the stacking order is turbostratic stacking [189]. The number of graphene layers is about 8 ~ 9 layers, confirmed by AFM thickness measurement (Figure 3.4). Raman mapping of laser induced graphene dot or ribbon indicates that all graphene layers were formed within laser-illuminated area, in agreement with EDS measurement (Figure 7.4) which shows higher carbon concentration in the central illuminated area. The turbostratic stacking order of laser-induced graphene was also confirmed by the FWHM comparison of 2D modes of laser-induced graphene and SLG because the FWHM of 2D mode of LIG is ~ 72 cm^{-1}, which is double that of the 2D peak of SLG graphene (~30 cm^{-1}) and 2D mode of LIG blueshifts by over 20 cm^{-1}, in agreement with the similar turbostratic stacking reported in ref. [193]. Bule shift in both G and 2D modes indicates that either the compressive strain in LIG graphene layers or chemical doping [192] or both. However, the buleshift in 2D further proves the p-type doping in LIG graphene layers due to the electron-phonon coupling [192]. The less blue shift in G band of laser-induced graphene compared to that of monolayer graphene transferred onto the other substrates indicates that the laser induced graphene is subjected to less strain or chemical doping [193]. However, larger FWHM of G band compared with single crystal graphite and monolayers transferred on SiO_2, stainless steel, and quartz indicates that LIG is LIG is an ensemble of small graphene domains and has poorer crystalline coherence of laser induced graphene resulting from the non-equilibrium process of laser illumination. As a tradeoff between FWHM and frequency shift of G and 2D bands, SLG on quartz is subjected to the least strain and/or chemical doping. The phonon energy of D and G′ (2D) bands of LIG were found to be dependent on the laser excitation energy; the D and G′ (2D) bands are blue-shifted with the increasing laser energy at the rate of about ~ $49.1\ cm^{-1}/eV$ and $103.4\ cm^{-1}/eV$, respectively, in agreement with ref. [191], because 2D band is laser-energy-dependent double resonance phonon mode. Also, the D/G ratio of LIG was observed to decrease with the increasing laser energy (Figure 3.7), because the laser spot size decreases with the decrease in wavelength (i.e., increase in laser energy), defects or disorders concentrate on edge, and thus larger spot size collects more signal from defect-concentrated edge of the irradiated spot.

(B) Three approaches for fabricating graphene based micro- and nano-structures and selective growth of SiC on SiO2 patterned Si substrates

To apply the laser-induced graphene technique for patterning micro- or nano-graphene structures, we proposed three approaches: (1) direct writing (DW); (2) illumination mask (IM); (3) pre-patterning (PP). The first method is limited by laser spot size or diffraction limit, the second method is limited by aperture opening and diffraction limit, and the third one is limited by the minimum feature size of the selectively deposited SiC. We concentrated on the study of the third method. Selective deposition of SiC on Si substrate using MBE was demonstrated to be feasible. The preliminary study on selective deposition of SiC was carried out by using photolithography process and MBE growth. 5 μm SiC line/5 μm SiO_2 spacing was successfully patterned and converted into 5 μm graphene line/5 μm SiO_2. Raman mapping near 2D mode shows the graphene feature in 5 μm graphene line/5 μm SiO_2. Selectively deposited SiC ribbons with the minimum feature size of 89 nm wide have been achieved with e-beam lithography and MBE growth techniques, although they have not been converted into graphene. The three field effect transistor configurations, single side-gated FET, double source side-gated FET, and double side-gated FET, have been designed and fabricated. However, we encountered difficulty in converting the selectively deposited SiC ribbon of the linewidth of less than 1 μm into graphene layers using available laser power of about 30 mW, even though we have demonstrated the feasibility of laser-converting 5 μm wide selectively deposited SiC ribbon into graphene layers. There are following possible reasons: (1) SiC film is too thin, resulting from the shadowing effect in deposition caused by the small dimension (as shown in Figure 5.3); (2) SiO_2 surrounding SiC dissipates the heat absorbed in SiC. The first possibility can be overcome by increasing the growth time and thus increasing the thickness of SiC (Figure 8.1 (a)); The second one can be solved by etching away the SiO_2 using HF acid after selective deposition of SiC (Figure 8.1 (b)). Air, as a replacement of SiO_2, has a lower thermal conductivity than that of SiO_2, and thus reduces the heat dissipation. Also, these two methods reduce the diffraction limit effect in laser illumination.

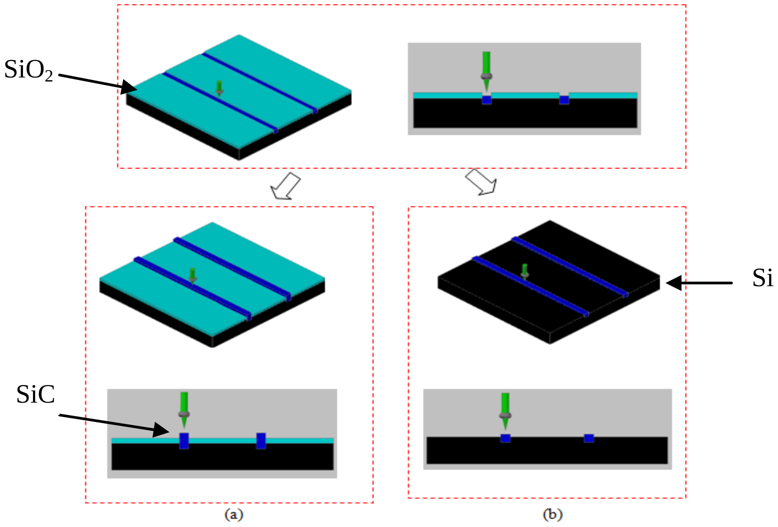

Figure 8.1: Two methods to overcome the difficulty in converting nanoscale SiC into graphene. (a) Thickness increase. (b) Removal of SiO_2 by etching with HF.

(C) Preliminary attempt on conductivity measurement

Metallization of Ti/Au (10 nm/30 nm) was evaporated with electron beam on gate, source, and drain of FET configurations with the assist of e-beam lithography. Two electrodes were deposited on laser-induced graphene μ-ribbon to measure the electrical conductance. However, the electrical resistance drops by only 9% compared with that of non-illuminated area. This is because the serial laser illumination process yields a graphene micro-ribbon made of small graphene domains overlapping one another or cross-linked by non-conductive SiC areas, resulting in low electrical conductance of graphene micro-ribbon. In order to make more continuous graphene ribbon, a larger laser spot should be used since graphene size is determined by laser spot size.

(D) Dependence of laser conversion on the crystalline structure and surface morphology

Power and time dependence of laser-induced graphene was performed on three samples grown at the same growth conditions but cleaned with three different methods. The last sample C is the selectively deposited SiC on pre-patterned $5 \times 5\ \mu m^2$ Si area. The illumination power and time were monitored with the intensity variation of Raman 2D peak. Although the threshold illumination power values are different for three different samples, the optimal illumination time shows the same trend in three samples; in other words, the optimal illumination time decreases with the increase in illumination power. The threshold power and illumination time to induce LIG are 10/4, 17/6 and 22/8 (mW/ms) for samples A, B and C, respectively, indicating the minimum laser power to induce graphene depends on the microstructure, morphology, and thickness of polycrystalline SiC film. Sample A has a few nanometers native SiO_2 on the Si substrate before growth, introducing some defects into the SiC polycrystalline (as shown 100 nm domain in Figure 5.2). Moreover, the SiC grain size in sample A is smaller than those of samples B and C, leading to more grain boundary in sample A than those in samples B and C. The more grain boundary, the lower thermal conductivity, and the higher local temperature. Therefore, sample A has the lowest threshold power. The comparison of samples B and C shows that the SiC grain size in sample C is more uniform than that in sample B and average grain size in sample B is smaller than that in sample C, contributing to the increase in local temperature in B. The uniformity of grain size is dependent on the thickness of SiC film (Figure 5.9). As shown in Figure 5.3, samples A and B have the same thickness of 188 nm , but sample C is only 51 nm, despite the same growth temperatures and time. The difference in thickness is caused by the shadowing effect in deposition, as shown in Figure 8.2. Since the Knudsen/effusive is placed at about 45^o with respect to the normal of substrate surface, the shadow effect results in less C60 deposited in the pre-patterned area (in micron or submicron scale). In order to obtain the same thickness of SiC film, the growth time for selective growth should be at least 188/51 = 3.7 times that of non-patterned growth. The selective growth in micro scale also limits the 3D diffusion of carbon and silicon atoms, making the SiC film different from that of non-patterned growth in microstructure. The relatively thinner SiC of sample C enables more uniform SiC and less light absorption than sample B, and thus increasing threshold illumination power in C.

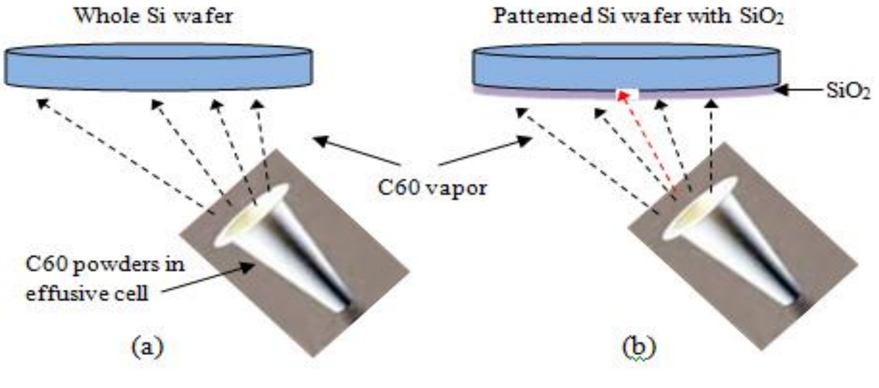

Figure 8.2: Schematic illustration of the shadow effect in selective MBE growth. (a) Entire Si wafer. (b) Pre-patterned Si wafer.

The domain size of LIG graphene also depends on the microstructure of polycrystalline SiC film. Larger SiC grain size and lower threshold illumination power contribute to the larger LIG graphene domain size. The threshold illumination power can be tuned by the microstructure and thickness of SiC film, which is controlled by MBE growth conditions and cleanliness of silicon substrate. Among the three samples A, B, and C, sample B have largest graphene size of about 23 nm because of its lower power compared with C and larger grain size compared with A. (e) Characterization of individual graphene based micro-structures

(E) Characterization of individual graphene based micro-structures

Graphene dots or discs in micro scale were patterned with laser illumination on three selected samples. Raman mappings near 2D mode show graphene dots match the SEM images of illuminated areas (Figure 7.1). The size of single laser-induced graphene dot on sample A is much smaller than those of samples B and C due to the lower threshold power of sample A. Raman mapping images of graphene dots in samples B and C show non-graphene features in the central part of graphene dots, which corresponds to central ablated areas in SEM images. However, but there is no such central ablated area in sample A, implying high power may cause the ablation of the central area, resulting in non-uniform graphene dots. We also observed a very thin SiC film remaining underneath graphene layer after laser illumination in SEM image, confirmed by Raman spectrum. Therefore, under the laser illumination, the bottom part of SiC film was recrystallized and silicon in the top part of SiC film was sublimated, with the remaining carbon atoms reconstructing into graphene layers. This was also confirmed with Raman spectra comparison before and after laser illumination (Figure 3.2). This means that the lower threshold power helps to get uniform graphene dots. The distribution of carbon atoms and thus graphene as well as whereabout of the sublimated Si were confirmed by the EDS results of sample C (shown in Figure 7.4). The ratio of carbon to silicon to oxygen (C: Si : O) in the three areas, i.e., the irradiated area, boundary area, and adjacent non-irradiation area, are 52.3: 45.0: 2.7, 49.5: 46.6: 3.9, and 46.4: 50.8: 2.9, respectively. The actual percentage of carbon in the irradiated area is expected to be higher than 52.3% because some signal from silicon substrate also contributes to the silicon percentage after the SiC film was ablated off and thin graphene layers are transparent to the electron beam and excited X-ray signal from silicon substrate. The increase in silicon percentage from the irradiated area to boundary to non-irradiated area indicates that silicon was sublimated and re-deposited on the surrounding area, with some oxidized. There is also some 2.7% oxygen in the irradiated graphene area, inducing defects or disorders in graphene layers, which is indicated by the defective D mode in Raman spectrum (Figure 3.2).The oxygen was introduced under the laser illumination in air. UVH or low pressure Ar could be employed as laser illumination atmosphere to reduce the defects or disorders in graphene caused by oxidation. In addition, more oxygen (3.9%) in the boundary is because higher local temperature causes more oxidation.

(F) Demonstration of arrays of graphene micro-structures

Periodic graphene dots in arrays of (1×2), (2×2), and (3×3) were patterned with LIG process. Although the graphene distribution is not uniform with weak graphene feature in the central area, the non-uniformity could be improved by further tuning the laser illumination power and time or performing illumination in UHV or argon atmosphere. The periodic graphene structure made of graphene/SiC/Si could be applicable to photonic microstructures, capacitor electrodes, or sensors, in which carrier mobility or electrical conductivity is not strictly required. Two micro-graphene ribbons of

1×10 μm^2 (Figure 7.3) and 2×40 μm^2 (Figure 3.5) were written with laser illumination and Raman mapping images show graphene signature within the illuminated area.

8.3 Proposals for future study

In the future study, since the laser illumination process is non-equilibrium due to rapid heating and cooling, it is critical to study the thermodynamic heating process of laser illumination, which may help to control graphene quality. Laser Illumination at different atmospheres, such as UHV or argon gas with different pressure may be compared with that in air. To improve the electrical conductivity of laser induced graphene ribbon, the parallel process (to illuminate the whole ribbon with a large laser spot size for one time) instead of serial process can be used to illuminate more continuous graphene ribbon, because point by point serial illumination yields a graphene ribbon made up of discrete small graphene domains overlapping each other or cross-linked by non-conductive areas. Interface between laser induced graphene and SiC should be investigated with TEM or LEED/LEEM. The electronic structure of laser-induced graphene should be investigated with STM/STS and angle-resolved photoelectron spectroscopy(ARPES). The investigation of the correlation between laser illumination conditions (i.e., power and time) and real temperature may be helpful for the illumination control of laser-induced graphene. The correlation between illumination conditions and real temperature can be calculated or simulated by using reported methods and/or software.

REFERENCES

1. H. W. Kroto, J. R. Heath, S. C. O'Brien, R. F. Curl, and R. E. Smalley, *Nature* **318**, 162 (1985).

2. S. Iijima and T. Ichihashi, *Nature* **363**, 603 (1993).

3. K. S. Novoselov, A. K. Geim, S. V. Morozov, D. Jiang, M. I. Katsnelson, I. V. Grigorieva, S. V. Dubonos, and A. A. Firsov, *Nature* (London) **438**, 197 (2005).

4. A. K. Geim and K. S. Novoselov, *Nature Materials* **6**, 183 (2007).

5. F. Molitor, J. Guttinger, C. Stampfer, S. Dr¨oscher, A. Jacobsen, T. Ihn, and K. Ensslin, *J. Phys.: Condens. Matter.* **23,** 243201 (2011).

6. A. H. Castro Neto, F. Guinea, N. M. R. Peres, K. S. Novoselov, and A. K. Geim, *Rev. Mod. Phys.* **81,** 109 (2009).

7. A. H. Castro Neto and K. Novoselov, *Rep. Prog. Phys.* **74,** 082501 (2011).

8. Y. B. Zhang, Y. W. Tan, H. L. Stormer, and P. Kim, *Nature* (London) **438**, 201 (2005).

9. M. I. Katsnelson, K. S. Novoselov, and A. K. Geim, *Nat. Phys.* **2**, 620 (2006).

10. C. W. J. Beenakker, *Rev. Mod. Phys.* **80**, 1337 (2008).

11. N. Stander, B. Huard, and D. Goldhaber-Gordon, *Phys. Rev. Lett.* **102**, 026807 (2009).

12. A. Rycerz, J. Tworzydlo, and C. W. J. Beenakker, *Nat. Phys.* **3**, 172 (2007).

13. A. Cresti, G. Grosso, and G. P. Parravicini, *Phys. Rev. B* **77**, 233402, (2008).

14. T. Ando, Y. S. Zheng, and H. Suzuura, *J. Phys. Soc. Jpn.* **71**, 1318 (2002).

15. K. Ziegler, *Phys. Rev. B* **75**, 233407 (2007).

16. H. Suzuura and T. Ando, *Phys. Rev. Lett.* **89**, 266603 (2002).

17. E. McCann, K. Kechedzhi, V. I. Fal’ko, H. Suzuura, T. Ando, and B. L.Altshuler, *Phys. Rev. Lett*. **97**, 146805 (2006).

18. S. V. Morozov, K. S. Novoselov, M. I. Katsnelson, F. Schedin, L. A. Ponomarenko, D. Jiang, and A. K. Geim, *Phys. Rev. Lett.* **97**, 016801 (2006)

19. F. V. Tikhonenko, D. W. Horsell, R. V. Gorbachev, and A. K. Savchenko, *Phys. Rev. Lett.* **100**, 056802 (2008).

20. X. S. Wu, X. B. Li, Z. M. Song, C. Berger, and W. A. de Heer, *Phys. Rev.Lett.* **98**, 136801 (2007).

21. K. I. Bolotin, K. J. Sikes, Z. Jiang, M. Klima, G. Fudenberg, J. Hone, P.Kim, and H. L. Stormer, *Solid State Commun.* **146**, 351 (2008).

22. M. Orlita, C. Faugeras, P. Plochocka, P. Neugebauer, G. Martinez, D. K.Maude, A. L. Barra, M. Sprinkle, C. Berger, W. A. de Heer, and M.Potemski, *Phys. Rev. Lett.* **101,** 267601 (2008).

23. X. Du, I. Skachko, A. Barker, and E. Y. Andrei, *Nat. Nanotechnol.* **3**, 491 (2008).

24. C. W. J. Beenakker, *Phys. Rev. Lett.* **97**, 067007 (2006).

25. Q. Y. Zhang, D. Y. Fu, B. G. Wang, R. Zhang, and D. Y. Xing, *Phys. Rev.Lett.* **101**, 047005 (2008).

26. J. Hass, F. Varchon, J. E. Millan-Otoya, M. Sprinkle, N. Sharma, W. A. De Heer, C. Berger, P. N. First, L. Magaud, and E. H. Conrad, *Phys. Rev. Lett.* **100**, 125504 (2008).

27. P. Sutter, M. S. Hybertsen, J. T. Sadowski, and E. Sutter, *Nano Lett.* **9**, 2654 (2009).

28. P. R. Wallace, *Phys. Rev.* **71**, 622 (1947).

29. J. C. Slonczewski and P. R. Weiss, *Phys. Rev.* **109**, 272 (1958).

30. K. Sugihara, S. Ono, H. Oshima, K. Kawamura, and T. Tsuzuku, *J. Phys. Soc. Jpn.* **51**, 1900 (1982).

31. H. Ajiki and T. Ando, *J. Phys. Soc. Jpn.* **65**, 505 (1996).

32. R. Saito, G. Dresselhaus, and M. S. Dresselhaus, *Phys. Rev. B* ***61***, 2981 (2000).

33. Y. H. Wu, T. Yu, and Z. X. Shen, *Journal of Applied Physics* **108**, 071301 (2010).

34. C. W. J. Beenakker, *Rev. Mod. Phys.* **80**, 1337 (2008).

35. T. Ando, *J. Phys. Soc. Jpn.* **74**, 777 (2005).

36. T. Ando, T. Nakanishi, and R. Saito, *J. Phys. Soc. Jpn*. **67**, 2857 (1998).

37. P. L. McEuen, M. Bockrath, D. H. Cobden, Y. G. Yoon, and S. G. Louie, *Phys. Rev. Lett.* **83**, 5098 (1999).

38. A. H. C. Neto, F. Guinea, N. M. R. Peres, K. S. Novoselov, and A. K. Geim, *Rev. Mod. Phys.* **81**, 109 (2009).

39. T. Ando, A. B. Fowler, and F. Stern, *Rev. Mod. Phys.* **54**, 437 (1982).

40. K. von Klitzing, G. Dorda, and M. Pepper, *Phys. Rev. Lett.* **45**, 494, (1980).

41. K. von Klitzing, *Rev. Mod. Phys.* **58**, 519 (1986).

42. J. W. McClure, *Phys. Rev.* **104**, 666 (1956).

43. J. W. McClure, *Phys. Rev.* **119**, 606 (1960).

44. R. S. Deacon, K. C. Chuang, R. J. Nicholas, K. S. Novoselov, and A. K. Geim, *Phys. Rev. B* **76**, 081406 (2007).

45. M. L. Sadowski, G. Martinez, M. Potemski, C. Berger, and W. A. de Heer, *Phys. Rev. Lett.* **97**, 266405 (2006).

46. G. Li and E. Y. Andrei, *Nat. Phys.* **3**, 623 (2007).

47. G. H. Li, A. Luican, and E. Y. Andrei, *Phys. Rev. Lett.* **102**, 176804 (2009).

48. D. L. Miller, K. D. Kubista, G. M. Rutter, M. Ruan, W. A. de Heer, P. N. First, and J. A. Stroscio, *Science* **324**, 924 (2009).

49. K. Nakada, M. Fujita, G. Dresselhaus, and M. S. Dresselhaus, *Phys. Rev. B* **54**, 17954 (1996).

50. M. Fujita, K. Wakabayashi, K. Nakada, and K. Kusakabe, *J. Phys. Soc. Jpn.*, **65,** 1920 (1996).

51. K. Wakabayashi, M. Fujita, H. Ajiki, and M. Sigrist, *Phys. Rev. B* **59**, 8271 (1999).

52. M. Ezawa, *Phys. Rev. B* **73**, 045432 (2006).

53. L. Brey and H. A. Fertig, *Phys. Rev. B* **73**, 235411 (2006).

54. K. I. Sasaki, S. Murakami, and R. Saito, *J. Phys. Soc. Jpn.* **75**, 074713, (2006).

55. Y. W. Son, M. L. Cohen, and S. G. Louie, *Phys. Rev. Lett.* **97**, 216803 (2006).

56. L. Yang, C. H. Park, Y. W. Son, M. L. Cohen, and S. G. Louie, *Phys. Rev. Lett.* **99,** 186801 (2007).

57. L. Brey and H. A. Fertig, *Phys. Rev. B* **73**, 235411 (2006).

58. A. F. Young and P. Kim, *Nat. Phys.* **5**, 222 (2009).

59. G. A. Steele, G. Gotz, and L. P. Kouwenhoven, *Nat. Nanotechnol.* **4**, 363 (2009).

60. D. Dragoman, *Phys. Scr.* **79**, 015003 (2009).

61. G. W. Semenoff, *Phys. Rev. Lett.* **53**, 2449 (1984).

62. A. F. Morpurgo and F. Guinea, *Phys. Rev. Lett.* **97**, 196804 (2006).

63. F. Miao, S. Wijeratne, Y. Zhang, U. C. Coskun, W. Bao, and C. N. Lau, *Science* **317**, 1530 (2007).

64. R. Danneau, F. Wu, M. F. Craciun, S. Russo, M. Y. Tomi, J. Salmilehto, A. F. Morpurgo, and P. J. Hakonen, *Phys. Rev. Lett.* **100**, 196802 (2008).

65. S. Adam, E. H. Hwang, V. M. Galitski, and S. Das Sarma, *Proc. Natl. Acad. Sci. U.S.A.* **104**, 18392 (2007).

66. E. H. Hwang, S. Adam, and S. Das Sarma, *Phys. Rev. Lett.* **98**, 186806, (2007).

67. T. Ando, *J. Phys. Soc. Jpn.* **75**, 074716 (2006).

68. K. Nomura and A. H. MacDonald, *Phys. Rev. Lett.* **98**, 076602 (2007).

69. V. V. Cheianov and V. I. Fal’ko, *Phys. Rev. Lett.* **97**, 226801 (2006).

70. V. F. Gantmakher, *Electrons and Disorder in Solids*, Clarendon/Oxford University Press, Oxford/New York, (2005).

71. Y. Imry, *Introduction to Mesoscopic Physics*, 2nd ed. Oxford University Press, New York, (2001).

72. X. Z. Yan and C. S. Ting, *Phys. Rev. Lett.* **101**, 126801 (2008).

73. F. V. Tikhonenko, D. W. Horsell, R. V. Gorbachev, and A. K. Savchenko,*Phys. Rev. Lett*. **100**, 056802 (2008).

74. R. V. Gorbachev, F. V. Tikhonenko, A. S. Mayorov, D. W. Horsell, and A. K. Savchenko, *Phys. Rev. Lett*. **98**, 176805 (2007).

75. F. V. Tikhonenko, A. A. Kozikov, A. K. Savchenko, and R. V. Gorbachev, *Phys. Rev. Lett.* **103**, 226801 (2009).

76. J. Tworzydło, B. Trauzettel, M. Titov, A. Rycerz, and C. W. J. Beenakker, *Phys. Rev. Lett.* **96**, 246802 (2006).

77. M. I. Katsnelson, *Eur. Phys. J. B* **51**, 157 (2006).

78. W. W. Ludwig, M. P. A. Fisher, R. Shankar, and G. Grinstein, *Phys. Rev. B* **50**, 7526 (1994).

79. K. Ziegler, *Phys. Rev. Lett.* **80**, 3113 (1998).

80. N. M. R. Peres, F. Guinea, and A. H. C. Neto, *Phys. Rev. B* **73**, 125411, (2006).

81. J. Cserti, *Phys. Rev. B* **75**, 033405 (2007).

82. P. M. Ostrovsky, I. V. Gornyi, and A. D. Mirlin, *Phys. Rev. B* **74**, 235443, (2006).

83. S. Ryu, C. Mudry, A. Furusaki, and A. W. W. Ludwig, *Phys. Rev. B* **75**, 205344 (2007).

84. K. Ziegler, *Phys. Rev. Lett.* **97**, 266802 (2006).

85. V. P. Gusynin and S. G. Sharapov, *Phys. Rev. Lett.* **95**, 146801 (2005).

86. J. Martin, N. Akerman, G. Ulbricht, T. Lohmann, J. H. Smet, K. Von Klitzing, and A. Yacoby, *Nat. Phys.* **4**, 144 (2008).

87. Y. B. Zhang, V. W. Brar, C. Girit, A. Zettl, and M. F. Crommie, *Nature Physics* **5**, 722 (2009).

88. J. H. Chen, C. Jang, S. Adam, M. S. Fuhrer, E. D. Williams, and M. Ishigami, *Nat. Phys.* **4**, 377 (2008).

89. Y. W. Tan, Y. Zhang, K. Bolotin, Y. Zhao, S. Adam, E. H. Hwang, S. Das Sarma, H. L. Stormer, and P. Kim, *Phys. Rev. Lett.* **99**, 246803 (2007).

90. K. I. Bolotin, K. J. Sikes, J. Hone, H. L. Stormer, and P. Kim, *Phys. Rev.Lett.* **101**, 096802 (2008).

91. T. Stauber, N. M. R. Peres, and A. H. C. Net, *Phys. Rev. B* **78**, 085418 (2008).

92. H. Ni, T. Yu, Z. Q. Luo, Y. Y. Wang, L. Liu, C. P. Wong, J. M. Miao, W. Huang, and Z. X. Shen, *ACS Nano* **3**, 569 (2009).

93. L. A. Ponomarenko, R. Yang, T. M. Mohiuddin, S. M. Morozov, A. A. Zhukov, F. Schedin, E. W. Hill, K. S. Novoselov, M. I. Katsnelson, and A. K. Geim, *Phys. Rev. Lett.* **102**, 206603(2009).

94. K. S. Viola, D. K. Campbell, and N. A. H. Castro, *Phys. Rev.* B **80** 035401 (2009).

95. C. Lee, X. Wei, J. W. Kysar, and J. Hone, *Science* **321** 38 (2008).

96. A. Alexander. A. Balandin, S. Ghosh, W. Bao, I. Calizo, D. Teweldebrhan, F. Miao, and C. N. Lau, *Nano Letters* 8, 3 (2008).

97. K. S. Kim, Y. Zhao, H. Jang, S. Y. Lee, J. M. Kim, J. H. Ahn, P. Kim, J. H. Ahn, P. Kim, J. Y. Choi, and B. H. Hong, *Nature* (London) **457**, 706 (2009).

98. Y. S. Li, W. W. Cai, J. H. An, S. Y. Kim, J. H. Nah, D. G. Yang, R. Piner, A. Velamakanni, I. H. Jung, E. Tutuc, S. K. Banerjee, L. Colombo, and R. S. Ruoff, *Science* **324**, 1312 (2009).

99. S. Bae, *Nature Nanotechnol.* **5** 574 (2010).

100. X. Wang, Y. Ouyang, X. Li, H. Wang, J. Guo, and H. Dai, *Phys. Rev. Lett* **100**, 206803 (2008).

101. J. Singh, *Smart Electronic Materials: Fundamentals and Applications*, Cambridge Unversity Press, 2005.

102. J. T. Grant and T. W. Haas. *Surf. Sci.* **21**, 76 (1970).

103. A. J. van Bommel, J. E. Crombeen, and A. van Tooren. *Surf. Sci.* **48**, 463 (1975).

104. K. Seibert, G. C. Cho, W. Kutt, and H. Kurz, *Physical Review B* 42, 5 (1990)

105. N. R. Gall, E. V. Rut’kov, and A. Y. Tontegode, *Int. J. Mod. Phys.* B **11**, 1865 (1997).

106. C. Oshima and A. Nagashima, *J. Phys.: Condens. Matter* **9**, 1 (1997).

107. J. Wintterlin and M. L. Bocquet, *Surf. Sci.* **603**, 1841 (2009).

108. Y. H. Wu, B. J. Yang, B. Y. Zong, H. Sun, Z. X. Shen, and Y. P. Feng, *J.Mater. Chem.* **14**, 469 (2004).

109. Y. H. Wu, P. W. Qiao, T. C. Chong, and Z. X. Shen, *Adv. Mater.* **14**, 64, (2002).

110. J. J. Wang, M. Y. Zhu, R. A. Outlaw, X. Zhao, D. M. Manos, B. C. Holloway, and V. P. Mammana, *Appl. Phys. Lett.* **85**, 1265 (2004).

111. M. Hiramatsu, K. Shiji, H. Amano, and M. Hori, *Appl. Phys. Lett.* **84**, 4708 (2004).

112. S. J. Park and R. S. Ruoff, *Nat. Nanotechnol.* **4**, 217(2009).

113. K. S. Subrahmanyam, L. S. Panchakarla, A. Govindaraj, and C. N. R. Rao, *J. Phys. Chem. C* 113, 11 (2009).

114. N. Li, Z. Wang, K. Zhao, Z. Shi, Z. Gu, and S. Xu, *Carbon* **48**, 255 (2010).

115. N. L. Rangel, J. C. Sotelo, and J. M. Seminario, *J. Chem. Phys.* **131**, 031105 (2009).

116. D. V. Kosynkin, A. L. Higginbotham, A. Sinitskii, J. R. Lomeda, A. Dimiev, B. K. Price, and J. M. Tour, *Nature,* **458**, 16 (2009).

117. L. Jiao, L. Zhang, X. Wang, G. Diankov, and H. Dai, *Science* **458**, 16 (2009).

118. A. L. Elı´as, A. R. Botello-Me´ndez, D. Meneses-Rodrı´guez, V. J´Gonza´lez, D. Ramı´rez-Gonza´lez, L. Ci, E. Mun oz- Sandoval, P. M. Ajayan, H. Terrones, and M. Terrones *Nano Lett.* **10**, 366 (2010).

119. Y. Ohkawara, T. Shinada, Y. Fukada, S. Ohshio, H. Saitoh, and H. Hiraga, *Journal of Materials Science* **30,** 2447 (2003).

120. D. Perrone, G. Maccioni, A. Chiolerio, C. Martinez de Marigorta, M. Naretto, P. Pandolfi, P. Martino, C. Ricciardi, A. Chiodoni, E. Celasco, L. Scaltrito, and S. Ferrero, in *Proceedings of the Fifth International WLT-Conference on Laser Manufacturing*, Munich, June 2009.

121. S. Lee, M. F. Toney, W. Ko, J. C. Randel, H. J. Jung, K.Munakata, J. Lu, T. H. Geballe, M. R. Beasley, R. Sinclair, H. C. Manoharan, and A. Salleo, *ACS Nano* **4** , 7524 (2010).

122. S. N. Yannopoulos, A. Siokou, N. K. Nasikas, V. Dracopoulos, F. Ravani, and G. N. Papatheodorou, *Adv. Funct. Mater.* **22**, 113 (2012).

123. M. G. Lemaitre, S. Tongay, Xi. Wang, D. K. Venkatachalam, J. Fridmann, B. P. Gila, A. F. Hebard, F. Ren,R. G. Elliman, and B. R. Appleton, *Applied Physics Letters* **100**, 193105 (2012).

124. D. Wei and X. Xu, *Applied Physics Letters* **100**, 023110 (2012).

125. J. B. Park, W. Xiong, Y. Gao, M. Qian, and Z. Q. Xie, *Appl. Phys. Lett.* **98**, 123109 (2011).

126. N. Yue, Y. Zhang, and R. Tsu, *Mater. Res. Soc. Symp. Proc.* Vol. 1407 (2012).

127. H. Hiura, T.W. Ebbesen, J. Fujita, K. Tanigaki, and T. Takada, *Nature* (London) **367**, 148 (1994).

128. T. W. Ebbesen and H. Hiura, H. *Adv. Mater.* **7**, 582(1995).

129. H. V. Roy, C. Kallinger, and K. Sattler, *Surface Science* **407**, 1 (1998).

130. H.V. Roy, C. Kallinger, B. Marsen, and K. Sattler, *Journal of Applied Physics* **83**, 9 (1998).

131. X. Lu, M. Yu, H. Huang, and R. Ruoff, *Nanotechnology* **10**, 269 (1999).

132. Y. B. Zhang, J. P. Small, W. V. Pontius, and P. Kim, *Appl. Phys. Lett.* **86**, 073104 (2005).

133. K. S. Novoselov, A. K. Geim, S. V. Morozov, D. Jiang, Y. Zhang, S. V. Dubonos, I. V. Grigorieva, and A. A. Firsov, *Science* **306**, 666 (2004).

134. M. Inagaki, *J. Mater. Res*. **4**, 1560 (1989).

135. L. M. Viculis, J. J. Mack, and R. B. Kaner, *Science* **299**, 28 (2003).

136. G. H. Chen, D. J. Wu, W. U. Weng, and C. L. Wu, *Carbon* **41**, 619 (2003).

137. X. H. Chen, H. S. Yang, G. T. Wu, M. Wang, F. M. Deng, X. B. Zhang,J. C. Peng, and W. Z. Li, *J. Cryst. Growth* **218**, 57 , (2000).

138. R. A. Greinke, R. A. Mercuri, and E. J. Beck, *U.S. Patent No. 4895713*, January 23, 1990.

139. G. H. Chen, W. G. Weng, D. J. Wu, C. L. Wu, J. R. Lu, P. P. Wang, and X. F. Chen, *Carbon* **42**, 753 (2004).

140. L. M. Viculis, J. J. Mack, O. M. Mayer, H. T. Hahn, and R. B. Kaner, *J. Mater. Chem.* **15**, 974 (2005).

141. X. L. Li, X. R. Wang, L. Zhang, S. W. Lee, and H. J. Dai, *Science* **319**, 9 (2009).

142. B. C. Brodie, *Philos. Trans. R. Soc. London* **149**, 249 (1859).

143. W. S. Hummers, Jr. and R. E. Offeman, *J. Am. Chem. Soc.* **80**, 1339 (1958).

144. S. Stankovich, D. A. Dikin, R. D. Piner, K. A. Kohlhaas, A. Kleinhammes, Y. Jia, Y. Wu, S. T. Nguyen, and R. S. Ruoff, *Carbon* **45**, 1558 (2007).

145. H. Kang, A. Kulkarni, S. Stankovich, R. S. Ruoff, and S. Baik, *Carbon* **47**, 1520 (2009).

146. G. K. Ramesha and S. Sampath, *J. Phys. Chem. C* **113**, 7985 (2009).

147. S. Horiuchi, T. Gotou, M. Fujiwara, T. Asaka, T. Yokosawa, and Y. Matsui, *Appl. Phys. Lett.* **84**, 2403 (2004).

148. S. Horiuchi, T. Gotou, M. Fuijwara, R. Sotoaka, M. Hirata, K. Kimoto, T. Asaka, T. Yokosawa, Y. Matsui, K. Watanabe, and M. Sekita, *Jpn. J. Appl. Phys., Part 2* **42**, L1073 (2003).

149. S. Stankovich, D. A. Dikin, R. D. Piner, K. A. Kohlhaas, A. Kleinhammes, Y. Jia, Y. Wu, S. T. Nguyen, and R. S. Ruoff, *Carbon* **45**, 1558 (2007).

150. C. Gómez-Navarro, R. T. Weitz, A. M. Bittner, M. Scolari, A. Mews, M. Burghard, and K. Kern, *Nano Lett.* **7**, 3499 (2007).

151. M. J. Allen, J. D. Fowler, V. C. Tung, Y. Yang, B. H. Weiller, and R. B. Kaner, *Appl. Phys. Lett.* **93**, 193119 (2008).

152. G. Eda, G. Fanchini, and M. Chhowalla, Nat. Nanotechnol. **3**, 270 (2008).

153. H. A. Becerril, J. Mao, Z. Liu, R. M. Stoltenberg, Z. Bao, and Y. Chen, *ACS Nano* **2**, 463 (2008).

154. G. H. Chen, W. G. Weng, D. J. Wu, and C. L. Wu, *Eur. Polym. J.* **39**, 2329 (2003).

155. S. Stankovich, D. A. Dikin, G. H. B. Dommett, K. M. Kohlhaas, E. J. Zimney, E. A. Stach, R. D. Piner, S. T. Nguyen, and R. S. Ruoff, *Nature (London)* **442**, 282 (2006).

156. D. A. Dikin, S. Stankovich, E. J. Zimney, R. D. Piner, G. H. B. Dommett,G. Evmenenko, S. T. Nguyen, and R. S. Ruoff, *Nature (London)* **448**, 457 (2007).

157. D. Li, M. B. Muller, S. Gilje, R. B. Kaner, and G. G. Wallace, *Nat. Nanotechnol.* **3**, (2008).

158. S. Park, J. H. An, R. D. Piner, I. Jung, D. X. Yang, A. Velamakanni, S. T. Nguyen, and R. S. Ruoff, *Chem. Mater.* **20**, 6592 (2008).

159. Y. Si and E. T. Samulski, *Nano Lett.* **8**, 1679 (2008).

160. Y. Hernandez, V. Nicolosi, M. Lotya, F. M. Blighe, Z. Y. Sun, S. De, I. T. McGovern, B. Holland, M. Byrne, Y. K. Gun’ko, J. J. Boland, P. Niraj, G. Duesberg, S. Krishnamurthy, R. Goodhue, J. Hutchison, V. Scardaci, A. C. Ferrari, and J. N. Coleman, *Nat. Nanotechnol.* **3**, 563 (2008).

161. J. Hamilton and J. Blakely, *Surf. Sci.* **91**, 199 (1980).

162. Y. Pan, D. X. Shi, and H. J. Gao, *Chin. Phys.* **16**, 3151 (2007).

163. P. W. Sutter, J. I. Flege, and E. A. Sutter, *Nature Mater.* **7**, 406 (2008).

164. M. C. Wu, Q. Xu, and D. W. Goodman, *J. Phys. Chem.* **98**, 5104 (1994).

165. S. Marchini, S. Gunther, and J. Wintterlin, *Phys. Rev. B* **76**, 075429, (2007).

166. J. C. Shelton, H. R. Patil, and J. M. Blakely, *Surf. Sci.* **43**, 493 (1974).

167. M. Eizenberg and J. M. Blakely, *Surf. Sci.* **82**, 228 (1979).

168. R. Rosei, M. De Crescenzi, F. Sette, C. Quaresima, A. Savoia, and P. Perfetti, *Phys. Rev. B* **28**, 1161 (1983).

169. Y. Gamo, A. Nagashima, M. Wakabayashi, M. Terai, and C. Oshima, *Surf. Sci.* **374**, 61 (1997).

170. L. C. Isett and J. M. Blakely, *Surf. Sci.* **58**, 397 (1976).

171. Z. Klusek, W. Kozlowski, Z. Waqar, S. Datta, J. S. Burnell-Gray, I.V. Makarenko, N. R. Gall, E. V. Rutkov, A. Y. Tontegode, and A. N. Titkov, *Appl. Surf. Sci.* **252**, 1221 (2005).

172. J. Coraux, A. T. N'Diaye, C. Busse, and T. Michely, *Nano Lett*. **8**, 565 (2008).

173. A. T. N'Diaye, J. Coraux, T. N. Plasa, C. Busse, and T. Michely, *New J. Phys.* **10**, 043033 (2008).

174. D. G. Castner, B. A. Sexton, and G. A. Somorjai, *Surf. Sci.* **71**, 519 (1978).

175. B. Lang, *Surf. Sci.* **53**, 317 (1975).

176. H. B. Lyon and G. A. Somorjai, *J. Chem. Phys.* **46**, 2539 (1967).

177. J. W. May, *Surf. Sci.* **17**, 267 (1969).

178. A. E. Morgan and G. A. Somorjai, *Surf. Sci.* **12**, 405 (1968).

179. S. Hagstrom, H. B. Lyon, and G. A. Somorjai, *Phys. Rev. Lett.* **15**, 491 (1965).

180. T. Aizawa, R. Souda, Y. Ishizawa, H. Hirano, T. Yamada, K. I. Tanaka, and C. Oshima, *Surf. Sci.* **237**, 194 (1990).

181. W. A. de Heer, C. Berger, X. S. Wu, P. N. First, E. H. Conrad, X. B. Li, T. B. Li, M. Sprinkle, J. Hass, M. L. Sadowski, M. Potemski, and G. Martinez, *Solid State Commun.* **143**, 92 (2007).

182. J. Hass, W. A. de Heer, and E. H. Conrad, *J. Phys.: Condens. Matter* **20**, 323202 (2008).

183. C. Berger, Z. M. Song, T. B. Li, X. B. Li, A. Y. Ogbazghi, R. Feng, Z. T. Dai, A. N. Marchenkov, E. H. Conrad, P. N. First, and W. A. de Heer, *J. Phys. Chem. B* **108**, 19912 (2004).

184. J. Hass, W. A. de Heer, and E. H. Conrad, *J. Phys.: Condens. Matter* **20**, 323202 (2008).

185. S. Iijima, *Journal of Solid State Chemistry* **42**, 101-105 (1982).

186. http://www.azom.com/article.aspx?ArticleID=6253

187. A. Brioude, P. Vincent, C. Journet, J. C. Plenet, and S. T. Purcell, *Appl.Surf. Sci.*, **221**, 4 (2004)

188. J. C. Burton, L. Sun, and F. H. Long, *Physical Review B* **59**, 3 (1999).

189. Y. Zhang and R. Tsu, *Nanoscale Research Letters* **5**, 805 (2010).

190. A. C. Ferrari, *Solid State Communication* **143** (2007) 47-57.

191. R.P. Vidano, D. B. Fishbach, L.J. Willis, and T.M. Loehr, *Solid State Comm*. **39**, 341 (1981).

192. A. Das, S. Pisana, B. Chakraborty, S. Piscanec, S. K. Saha, U.V. Waghmare, K. S. Novoselov, H. R. Krishnamurthy, A. K. Geim, A. C. Ferrari, and A. K. Sood, *Nature Nanotechnology* **3**, 210 (2008).

193. A. C. Ferrari, J. C. Meyer, V. Scardaci, C. Casiraghi, M. Lazzeri, F. Mauri, S. Piscanec, D. Jiang, K. S. Novoselov, S. Roth, and A. K. Geim, *Phys. Rev. Lett.* **97,** 187401 (2006).

194. L. G. Cancado, K. Takai, T. Enoki, M. Endo, Y. A. Kim, *Applied Physics Letter* **88**, 163106 (2006).

195. A. V. Hamaza, M. Balooch, and M. Moalem, *Surface Science* **317**, L1129 (1994).

196. C. P. Cheng, J. W. Huang, T. W. Pi, and H. H. Lee, *Journal of Applied Physics* **99**, 123708 (2006).

197. J. C. Li, P. Batoni, and R. Tsu, *Thin Solid Films* **518**,1658 (2010).